TUM

Lehrstuhl für Elektrische Energiespeichertechnik
Fakultät für Elektrotechnik und Informationstechnik
Technische Universität München

Implications of Current Density Distribution in Lithium-Ion Battery Graphite Anodes on SEI Formation

Dipl.-Ing. (Univ.) Frank M. Kindermann

Vollständiger Abdruck der von der Fakultät für Elektrotechnik und Informationstechnik der Technischen Universität München zur Erlangung des akademischen Grades eines

Doktor-Ingenieurs (Dr.-Ing.)

genehmigten Dissertation.

Vorsitzender: Prof. Dr. rer. nat. Gerhard Wachutka
Prüfer der Dissertation: 1. Prof. Dr.-Ing. Andreas Jossen
                         2. Prof. Dr. rer. nat. Jürgen Garche

Abstract

The formation of the solid-electrolyte interphase (SEI) and the associated capacity fade is an ongoing research topic for understanding the aging behavior of lithium-ion batteries. The current density distribution inside the graphitic anode mainly defines the homogeneity of the aging behavior. The presented work analyzes the influences on the formation of the SEI over cycling of lithium-ion cells. To describe the aging behavior, a physicochemical model is implemented and the inhomogeneity of SEI growth within the graphite electrode is studied. The non-uniform charge distribution can qualitatively be measured by means of electrochemical impedance spectroscopy. With the aid of a laboratory multiple working electrode cell, equilibration effects within the graphite particles and perpendicular through the electrode plane can be quantitatively measured for up to 40 h. The subsequently implemented model which accounts for the dominating equilibration processes is used to perform a design variation study to improve the current density distribution within the electrode. By including pore channels to reduce the overall tortuosity of the electrode, utilization as well as rate capability of a thick electrode can be improved and also SEI growth becomes more homogeneous.

Zusammenfassung

Die Bildung der Solid-Electrolyte Interphase (SEI) und der damit verbundene Kapazitätsverlust befinden sich im Fokus der Forschung, um das Alterungsverhalten von Lithium-Ionen-Batterien zu verstehen. Die Stromdichteverteilung in der Graphitanode bestimmt hauptsächlich die Gleichmäßigkeit des Alterungsverhaltens. Die vorliegende Arbeit analysiert die Einflüsse der SEI-Bildung auf das Zyklisierungsverhalten einer Lithium-Ionen-Zelle. Mit Hilfe eines in der Arbeit entwickelten physikalisch-chemischen Modells kann das Alterungsverhalten beschrieben und das inhomogene SEI-Wachstum in der Graphitelektrode beschrieben werden. Die ungleichmäßige Ladungsverteilung kann mittels elektrochemischer Impedanzspektroskopie qualitativ gemessen werden. Ausgleichseffekte über 40 h innerhalb der Graphitpartikel und durch die Elektrodenschicht hindurch können mit einer Laborzelle, die aus mehreren Arbeitselektroden besteht, quantitativ bestimmt werden. Ein auf den Relaxationsmessungen aufbauendes Modell wird für eine Elektrodendesignstudie genutzt, die die Gleichmäßigkeit der Stromdichteverteilung verbessern soll. Durch das Einbringen von Transportkanälen in die Elektrode kann die Tortuosität verringert werden. Dies führt zu einer gleichmäßigeren Ausnutzung der Elektrode sowie zu einem besseren Ratenverhalten und schlägt sich in einem gleichmäßigeren SEI-Wachstum nieder.

Contents

Abbreviations

Li_2CO_3 . . . . lithium carbonate

Li_2DFB . . . . . . dilithium dodecafluorododecaborate

Li_2O . . . . lithium oxide

$LiAsF_6$ . . . . . . lithium hexafluoroarsenate

$LiBF_4$ . . . . . . lithium tetrafluoroborate

$LiClO_4$ . . . . . . lithium perchlorate

LiF . . . . lithium fluoride

$LiIm$ . . . . lithium bis(trifluoromethanesulfonyl)imide

$LiPF_6$ . . . . . . lithium hexafluorophosphate

$LiTFOP$ . . . . . lithium tetrafluoro(oxalato)phosphate

$LiTf$ . . . . lithium trifluoromethanesulfonate

$ROCO_2Li$ . . . . . semicarbonates

AFM . . . . atomic force microscopy

CEI . . . . cathode electrolyte interphase

CMC . . . . carboxymethylcellulose

DEC . . . . diethyl carbonate

DMC . . . . dimethyl carbonate

EC . . . . ethylene carbonate

ECM . . . . equivalent circuit model

EDS . . . . see EDX

EDX . . . . electron dispersive X-ray spectroscopy

EEI . . . . electrode-electrolyte interphase

EELS . . . . . . electron energy loss spectroscopy

EIS . . . . electrochemical impedance spectroscopy

EMC . . . . ethylmethyl carbonate

EQCM . . . . . . electrochemical quartz crystal microbalancing

FEC . . . . fluoroethylene carbonate

FTIR . . . . Fourier transformed infrared spectroscopy

HF . . . . hydrogen fluoride

HOMO . . . . . . highest occupied molecular orbital

HOPG . . . . . . highly oriented pyrolytic graphite

IR . . . . infrared

LAM . . . . loss of active material

LFP . . . . lithium iron phosphate

LG . . . . large particle graphite

LLI . . . . loss of lithium-ion inventory

LTO . . . . lithium titanate

LUMO . . . . . . lowest unoccupied molecular orbital

MLC . . . . multi-layer cell

NCM . . . . lithium nickel cobalt manganese oxide

NMP . . . . *N*-methylpyrrolidone

NMR . . . . nuclear magnetic resonance

P2D pseudo-2D

PC . . . . propylene carbonate

PMC . . . . propylmethyl carbonate

PVdF . . . . . . poly(vinylidene fluoride)

SEI . . . . solid electrolyte interphase

SEM . . . . scanning electron microscopy

SG . . . . small particle graphite

SOC . . . . state-of-charge

SOH . . . . state-of-health

SPI . . . . solid permeable interphase

SPM . . . . scanning probe microscopy

SPM . . . . single particle model

STM . . . . scanning tunneling microscopy

TEM . . . . transmission electron microscopy

UV . . . . ultraviolet

VC . . . . vinylene carbonate

VEC . . . . vinyl ethylene carbonate

XAS . . . . X-ray absorption spectroscopy

XEDS . . . . . . see EDX

XPS . . . . X-ray photoelectron spectroscopy

Symbols

Please note that the symbols are listed as used in the main part of this thesis and may vary due to special requirements of the journals or special usage within the integrated papers. All symbols and their respective meaning are defined in each paper individually.

a_s . . . . specific surface in 1/m

α_a . . . . anodic charge-transfer coefficient

α_c . . . . cathodic charge-transfer coefficient

c_l . . . . lithium-ion concentration in the electrolyte in mol/m^3

c_s . . . . lithium-ion concentration in the active material in mol/m^3

$c_{s,\mathrm{max}}$ . . . . . maximum lithium-ion concentration in the active material in mol/m^3

D_l . . . . diffusion coefficient in the electrolyte in m^2/s

δ_{SEI} . . . . thickness of SEI layer in m

E_{Eq} . . . . thermodynamic equilibrium potential in V

$\varepsilon_{l,\mathrm{pos/neg}}$ . . . . porosity of the positive/negative electrode

$\varepsilon_{l,\mathrm{sep}}$ . . . . . . porosity of the separator

$\varepsilon_{s,\mathrm{pos/neg}}$ . . . . volume fraction of the positive/negative active material

η . . . . overpotential in V

F . . . . Faraday's constant, $96\,485\,\mathrm{C/mol}$

$f_\pm$ . . . . mean activity coefficient

i_0 . . . . exchange current density in A/m^2

$\boldsymbol{i}_l$ . . . . total current density in the electrolyte in A/m^2

i_n . . . . charge-transfer current density in A/m^2

$\boldsymbol{i}_s$ . . . . total current density in the solid phase in A/m^2

j_n . . . . pore-wall flux density in mol/m^2 s

k_a . . . . anodic reaction rate constant in m/s

k_c . . . . cathodic reaction rate constant in m/s

κ . . . . electrolyte conductivity in S/m

l_{neg} . . . . thickness of the negative electrode domain in m

l_{pos} . . . . thickness of the positive electrode domain in m

l_{sep} . . . . thickness of the separator domain in m

n . . . . number of electrons

$\boldsymbol{N}_l$ . . . . ionic flux density in the electrolyte in $\mathrm{mol/m^2\,s}$

$\boldsymbol{N}_s$ . . . . ionic flux density in the active material in $\mathrm{mol/m^2\,s}$

N_M . . . . MacMullin's number

ω . . . . angular frequency in 1/s

ϕ . . . . phase shift in degree

Φ_l . . . . electrolyte potential in V

Φ_s . . . . electrode potential in the active material in V

R . . . . unviersal gas constant, $8.314\,\mathrm{J/mol\,K}$

s_i . . . . stoichiometric coefficient of species i

σ . . . . solid phase conductivity in S/m

T . . . . absolute temperature in K

t . . . . time in s

t_+ . . . . transport number of cations

τ . . . . tortuosity

$Z(\omega)$ . . . . complex impedance in Ω

$Z'(\omega)$ . . . . real part of the complex impedance in Ω

$Z''(\omega)$ . . . . . . imaginary part of the complex impedance in Ω

1 Introduction of the Solid Electrolyte Interphase

Due to thermodynamic instabilities of the electrolyte, a passivating layer called the solid electrolyte interphase (SEI) is formed on the negative electrode in lithium-ion batteries.[1,2] The SEI was first described and named by Emanuel Peled in a paper called *The Electrochemical Behavior of Alkali and Alkaline Earth Metals in Nonaqueous Battery Systems – The Solid Electrolyte Interphase Model* in 1979. Since he presented parts of his paper already in October 1977 at the annual meeting of *The Electrochemical Society* in Atlanta, Georgia, the year 1977 is often found in literature as the year of the first mentioning of the term.[3] Although interfaces have been in focus since the beginning of battery research,[4] Peled started a quest for the Holy Grail of lithium-ion battery research.[5] The search for a perfect SEI is an ongoing research topic and to this date *Web of Science* finds more than 5,000 entries with a topic concerning the SEI.[6]

Before going into details of SEI formation and the desired properties, the typical setup of a lithium-ion cell is recalled in Figure 1.1.[7] In nowadays commercially available lithium-ion cells, the anode consists mainly of graphite and the cathode of either transition-metal oxide structures (with the transition-metals such as nickel, cobalt and manganese) or phosphates with lithium iron phosphate (LFP) being the best-known material.[8] From a chemical definition the anode is the electrode that is oxidized while the cathode is the electrode that is reduced. For batteries during discharge the negative electrode is oxidized, i.e. the anode, and the positive electrode is reduced, i.e. the cathode. As this definition
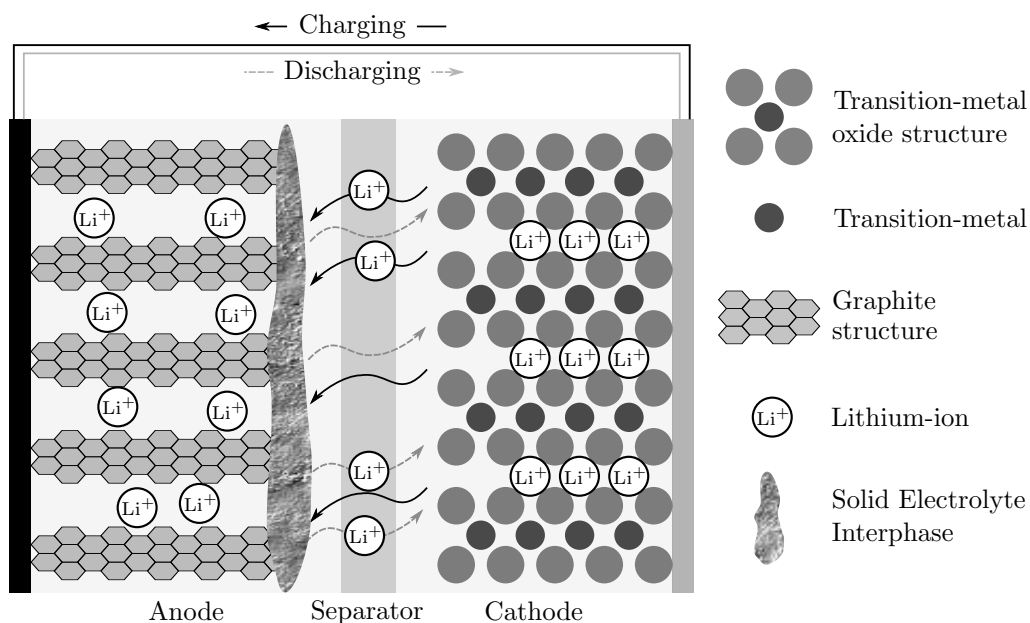

Figure 1.1: Schematic depiction of a lithium-ion cell.[7] Graphite is used as the anode material, since lithium-ions can be reversibly intercalated during the charging process. Transition-metal oxides are the most-used materials for the cathode side, as they provide lithium-ions from their structure for reversible cycling.

is reversed during charge, within the field of batteries the naming for the discharge scenario is used invariably to avoid confusion.[9]

The depicted SEI covering the anode in Figure 1.1 will be subject of the rest of this chapter. Simplistically and schematically, the SEI is located between the separator and the anodic graphite structure. In reality the SEI covers each graphite particle located between the separator and the current collector. By the definition of Peled it is obvious why the SEI is called an interphase. It is a domain inside a cell between the electrode and the electrolyte and has a certain thickness as well as its own electrochemical behavior. Still, some publications use the word *interface* instead of *interphase*. By definition, an interface is the surface boundary between two phases and in case of an SEI containing battery this would actually imply two interfaces, electrode/SEI and SEI/electrolyte. Therefore, the use of the spelling *interphase* appears to be more correct and will be used in the remainder of this document. This introduction will give an overview of Peled's first paper and the basics of SEI formation mostly based on the extensive reviews by Xu,[4,10] An et al.[11] and Collins et al.[12]

1.1 First scientific description of the SEI

In his paper Peled, introduces a 15 to 25 Å thick layer that covers all alkali and alkaline earth metals in non-aqueous batteries at first contact with the electrolyte solution and consists of metal as well as solution reaction products. Since the layer has properties of a solid electrolyte (i.e. very low electronic and high ionic conductivity) and is an interphase between electrode and electrolyte, it is called the "Solid Electrolyte Interphase". He further states that the properties of the SEI will dictate the electrochemical behavior of a cell containing an SEI covered electrode. Therefore, some basic properties have to be considered which are (i) the morphology of the interphase (porosity and crystal size of insoluble products), (ii) the layer thickness δ_{SEI}, (iii) the transference numbers of electrons as well as cationic and anionic defects and (iv) their respective mobility.[3]

In his model the SEI growth rate is determined by a mechanism of cathodic reactions (e.g. solvent reduction), when assuming a dense SEI on the anode surface. Two extreme cases are conceivable in that respect. The first is an inhomogeneous SEI by impurities in the cell building up cathodic areas that allow electron flux and reduction of the solvent. Secondly, in a pure system without inhomogeneities, the migration of electrons through the SEI is the rate determining step for new SEI formation.[13] Both mechanisms lead to a parabolic law of growth ($t^{1/2}$). In reality not all lithium electrodes display that parabolic behavior but comply with

$$\delta_{\text{SEI}} = const \cdot t^{\alpha} \tag{1.1}$$

with values of α between 1/5 and 1/2, due to dependencies of e.g. the lithium-ion diffusion coefficient or the SEI resistivity on the layer thickness. Also cracks and holes as well as other inhomogeneities in the SEI will contribute to the deviation from $\alpha = 1/2$.[3] A detailed look into SEI modeling approaches will be given in Chapter 3. The paper concludes that a proper anodic SEI is the key for all future batteries working with non-aqueous electrolytes and that controlling SEI properties will improve battery performance.[3]

After this historical introduction of the SEI's first description on metal electrodes, the following sections will reveal the progress to present day lithium-ion batteries and their respective passivation film on carbon anodes. Since most of the discussion is focused on the anodic SEI, Section 1.5 will also consider

a passivation film on the cathode.

1.2 From lithium-metal to carbon and alloy anodes

Two properties lead to lithium-metal being desired as the anode material – its electronegativity (about $-3.0\,\text{V}$ vs. Standard Hydrogen Electrode) and its weight (being the lightest metal in the periodic table with $0.534\,\text{g/cm}^3$). These properties in combination with a matching cathode lead to a high cell voltage and a high specific capacity (lithium at $3.86\,\text{Ah/g}$). However, the use of lithium-metal as an anode in a cell setup poses a great risk due to inhomogeneous lithium deposition during cycling which may result in dendrite growth. These dendrites can lead to separator punctuation and cause internal shorts with a possibly following thermal runaway.[4,12]

Since lithium-metal exhibits the mentioned safety risks, research was directed to alternative materials that still had the benefits of a high cell voltage and energy density. Similar to cathode materials, intercalation electrodes became interesting and carbonaceous lattice structures emerged as the most promising candidate which were known to store lithium since 1955.[14] In intercalation electrodes, lithium is stored in its ionic form and, hence, can not cause dendrite growth under normal usage which decreases the safety risk. Also, due to an expansion of about $10\,\%$ between intercalation and deintercalation, mechanical stress and material degradation of carbon is relatively low.[4,12,15]

Graphite is the primarily used carbon in lithium-ion batteries due to its large crystallite domains which lead to the highest intercalation capacities. In amorphous carbons, the structure is more random which decreases its capacity but in return offers a larger surface than graphitic carbon which allows for an increase in possible current rates. Additionally, the amorphous carbon surface has a higher resistivity against solvent co-intercalation compared to graphite.[12]

The theoretical maximum in storable capacity within graphite amounts to $372\,\text{mAh/g}$ when a full utilization ($x = 1$) is considered in the reversible chemical equation

$$\text{Li}_x\text{C}_6 \xrightleftharpoons[\text{charge}]{\text{discharge}} x\,\text{Li}^+ + 6\,\text{C} + x\,\text{e}^- \tag{1.2}$$

In practice, capacities of about $350\,\text{mAh/g}$ are common. They can be higher (closer to theoretical value) when very small currents are used.[16]

The conclusion by Fong et al.,[15] that reductive electrolyte decomposition products settle on the carbon surface and, hence, prevent further degradation as seen in Figure 1.2, is one of three statements that are the foundation for the success of lithium-ion batteries with carbon anodes. In their paper they extended Peled's work[3] from lithium-metal to carbon. The remaining two conclusions are that the reduction process is primarily finished after the first cycle and that the electrolyte solvent structure is mainly responsible for the formation of the passivation film. Since carbon emerged as the most widely used anode in common day lithium-ion batteries due to an optimum in costs coupled with electrical properties, carbon anodes will be the focus of the following considerations.

Newest developments for future anode materials are investigating lithium-metal alloys such as silicon (Si) or tin (Sn) due to their higher specific capacity of 3579 to $4212\,\text{mAh/g}$[8,18,19] and $993\,\text{mAh/g}$,[20] respectively. The SEI layer on metal alloy anodes is similar to the one on graphite[20] but faces greater challenges due to the volume expansion of up to $400\,\%$ between the charged and discharged state.[8,10]
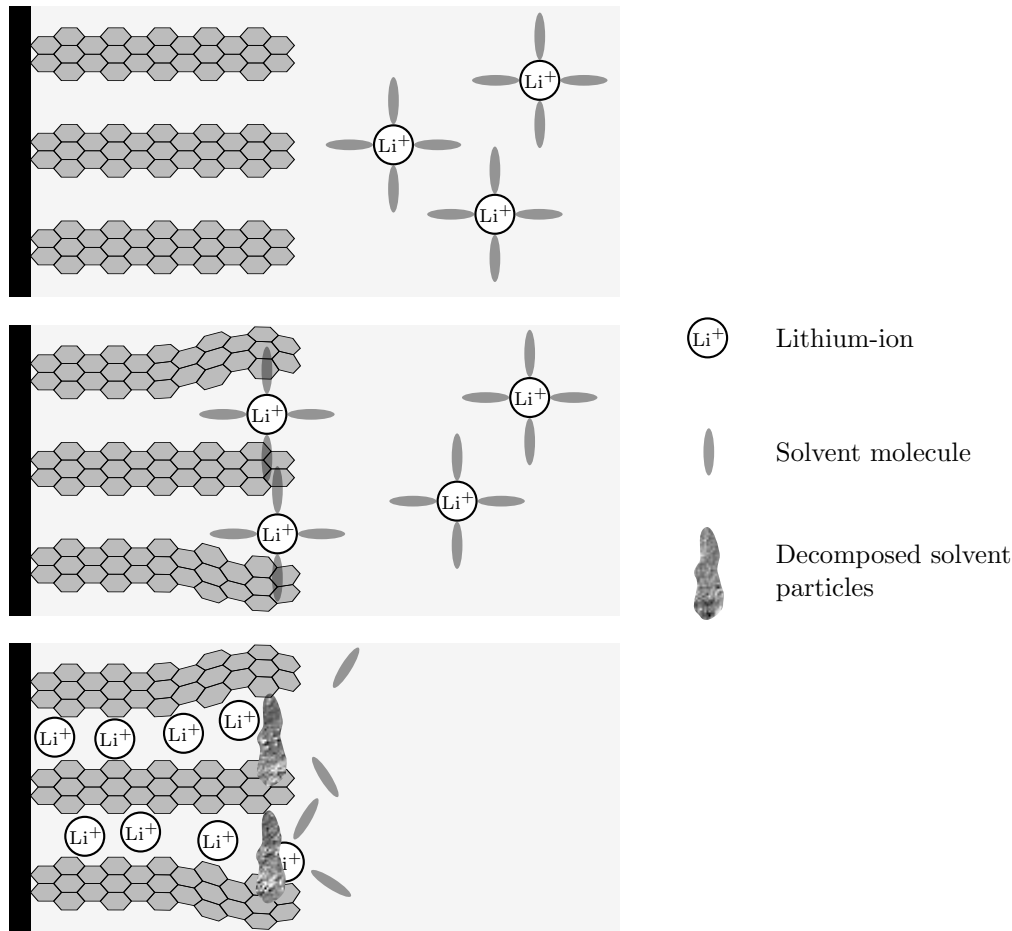
Figure 1.2: Schematic of the SEI formation process that starts with the first charge. Solvated lithium-ions intercalate into the graphite structure and decompose. The decomposed solvent particles act as a barrier to other solvent molecules and ensure that only lithium-ions intercalate in future cycles and no further co-intercalation of solvent molecules occurs.[17]

1.3 Importance of electrolyte composition

Whereas the electrode capability is measured based on its respective redox potential, electrolytes are quantified by their electrochemical stability window which is the potential range between its oxidative and reductive decomposition limits. A properly working electrolyte – consisting of a solvent and a solute – needs to have certain properties besides being in its electrochemical window given by the redox potential of the used electrodes. Those properties are (i) good ionic conductivity for lithium-ions and corresponding electronic insulation for electrons, (ii) chemical stability toward other cell components, (iii) robustness against thermal, electrical or mechanical abuse scenarios and (iv) eco-friendliness.[4]

The thermodynamically stable window of the electrolyte is given by its lowest unoccupied molecular orbital (LUMO) and highest occupied molecular orbital (HOMO). Outside this window, the anode will reduce the electrolyte and the cathode will oxidize the electrolyte. To prevent this reduction or oxidation, an SEI or cathode electrolyte interphase (CEI) needs to form on the anode or the cathode, respectively.[21,22] This can be seen in Figure 1.3.

Electrolyte solvents should fulfill four basic requirements. Those requirements are (i) a high dielectric constant for salt dissolution, (ii) a low viscosity for good ion transport, (iii) a low melting and high
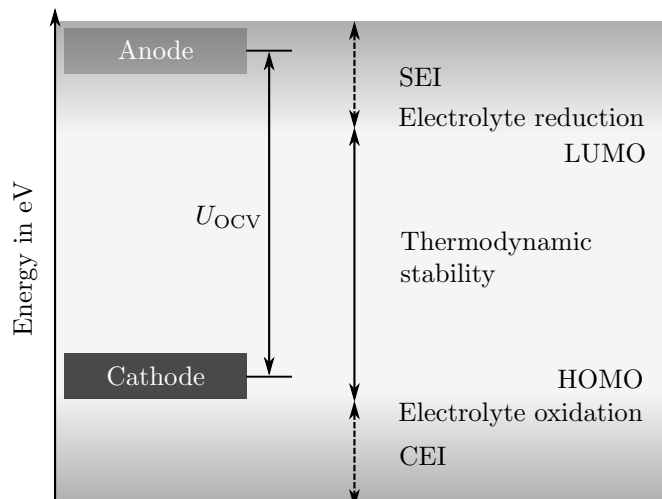
Figure 1.3: Stability window of a sample electrolyte. Since the anode is above the electrolyte reduction potential, an SEI will form there. The cathode, in contrast, has not exceeded the oxidation potential yet and is still in the stable electrochemical window.[21]

boiling point as well as (iv) safe and non-toxic properties. Two of those properties in any solvent are limiting the use of solvents in lithium-ion battery systems. First, for being able to dissociate an electrolyte salt, they have to be polar enough and additionally, they have to stay inert in the electrochemical potential window between 0.0 and 5.0 V.[4]

With the findings of Dahn and co-workers[15] that ethylene carbonate (EC) builds an effective SEI whereas propylene carbonate (PC) co-intercalates in graphite, most following research efforts were focused on EC-based electrolytes for lithium-ion batteries. The introduction of electrolyte mixtures of EC with a linear carbonate (e.g. dimethyl carbonate (DMC), diethyl carbonate (DEC), ethylmethyl carbonate (EMC) or propylmethyl carbonate (PMC)) lead to a change of anode material. Starting from 1993 basically all new lithium-ion cells were produced with graphite and EC-based electrolytes containing one or more of the mentioned linear carbonates depending on the manufacturer.[4]

After already mentioning the properties of an ideal electrolyte and the solvent, also five ideal properties of an electrolyte salt can be listed. Namely they are (i) complete dissolution in the solvent, (ii) anion stability against decomposition at the cathode and (iii) decomposition of the electrolyte solvent, (iv) inertness toward cell components of the anion and cation and, finally, (v) anion resistiveness against reactions caused by heating or trace water. Lithium hexafluorophosphate ($LiPF_6$) featured the best set of properties compared to various conducting solutes such as lithium perchlorate ($LiClO_4$), lithium hexafluoroarsenate ($LiAsF_6$), lithium tetrafluoroborate ($LiBF_4$), lithium trifluoromethanesulfonate (LiTf) or lithium bis(trifluoromethanesulfonyl)imide (LiIm).[4] Most commercially available lithium-ion batteries nowadays are using $LiPF_6$ as the electrolyte salt and will continue using $LiPF_6$ in the future. Its advantages are the well-balanced properties although each of the other salts has at least one property that is better. Due to that fact there is still room for improvements regarding thermal and chemical stability, especially against water.[10] Typically, a salt concentration of 1 mol/l (synonymous to 1 M) is used for lithium-ion batteries.

With research still going on, many alternative electrolyte salts have been tested in past years. Only two types, lithium tetrafluoro(oxalato)phosphate (LiTFOP) and dilithium dodecafluorododecaborate (Li_2DFB), emerged with overall similar or better properties than standard $LiPF_6$ in respect to thermal

and chemical stability. Considerable higher production efforts and higher costs have inhibited these electrolyte salts a market entry, yet.[10]

Another component to stabilize electrolytes and, hence, lithium-ion batteries are electrolyte additives which will be covered more extensively in Section 1.4. One of the most successful and, therefore, commercially used additives is vinylene carbonate (VC), just to mention an example at this point.[10]

The stability of the electrolyte has an essential influence on the degradation of lithium-ion batteries. One of the main degradation mechanisms is the ongoing growth of the SEI by parasitic reactions. Dahn and co-workers formulated a general mathematical description for this increase in thickness δ_{SEI} over time t

$$\frac{d\delta_{SEI}}{dt} = \sqrt{\frac{1}{2k}}\, t^{-1/2} \tag{1.3}$$

where k is a constant dependent on the specific electrode/electrolyte combination.[23] Other mechanisms include impurities from moisture causing hydrogen fluoride (HF) generation and following dissolution of transition-metals or reactions in the bulk electrolyte, dissolution of interphase components by the electrolyte and corrosion of the current collectors. Last, temperature induced degradation due to higher overpotentials at low temperatures or accelerated side reactions at higher temperatures are possible.[10]

To summarize this section, the basic formula of electrolytes for almost all commercialized cells consists of $1\,M$ $LiPF_6$, EC and linear carbonates. Although the low temperature limit can be adjusted by the mixing ration of EC and the linear carbonates, the basic formulation faces certain thermal restrictions. Typical temperature limits of a commercial electrolyte are between -20 and $50\,°C$, set by the melting point of EC (lower limit) and the reactivity and decomposition of $LiPF_6$ at higher temperatures (upper limit). Whereas an operation at temperatures below the limit compromises the utilized capacity and power capability but can be reversed, a long-lasting operation above $50\,°C$ leads to irreversible damage to the system and can be hazardous.[4]

1.4 Basics of SEI formation on anodes

Since the SEI is the foundation on which lithium-ion batteries are operating,[5] its ideal parameters can be specified as follows. (i) The electron transference number t_e should be 0 to block electron passage. (ii) Ion conductivity should be high for rapid lithium-ion migration toward or from the graphite bulk material. (iii) Adhesion to the carbonaceous surface should be good and (iv) the interphase should be flexible with a good mechanical strength to suppress cracking, e.g. during expansion and contraction of the carbon particles due to lithiation and delithiation. Also, a low SEI solubility in the used electrolytes is desirable to oppose a permanent new decomposition of electrolyte for renewing the SEI and, therefore, irreversible consumption of lithium-ions. Last, a uniform morphology and composition should be aimed at for a homogeneous current distribution.[4]

Due to – in a first approximation – similar potentials of lithiated graphite (about $0.1\,V$ vs. Li/Li^+) and lithium-metal, the SEI formation process was suggested to be similar for both materials and Peled's model for lithium-metal was adopted by Dahn's group for carbon anodes.[15] It was, though, realized that SEI formation did not start at first contact – as with lithium-metal – but only after negatively polarizing the carbon to a certain potential and that the formation process happened stepwise.[4]

SEI formation is generally believed to occur at potentials of about $1.0\,V$ vs. Li/Li^+ but also has been

shown to form salt products on the edge sites of the carbon at potentials as high as 2.0 to 1.5 V vs. Li/Li^+. Decomposition of electrolyte salts containing fluoride occur at potentials lower than 1.5 V vs. Li/Li^+ as well.[24] Coverage of the basal plane in contrast is finished at 0.8 V vs. Li/Li^+ with mainly solvent decomposition products.[25]

In 1997 Peled et al. modified the previous model for carbonaceous electrodes and called it "mosaic model", since multiple different decompositions occur at the negative electrode simultaneously that deposit different insoluble products.[26] The most accepted decomposition products include lithium fluoride (LiF), lithium oxide (Li_2O), lithium carbonate (Li_2CO_3), semincarbonates ($ROCO_2Li$ with R being a low-molecular-weight alkyl group) and polyolefins. This heterogeneous interphase consists of thermodynamically more stable salts close to the electrode/SEI interface (LiF, Li_2O and Li_2CO_3) and partially reduced, metastable, organic species such as alkyl carbonates closer to the SEI/electrolyte interface ($ROCO_2Li$ and polyolefins). These metastable products can be thermally decomposed into stable products like Li_2CO_3 prior to a thermal runaway.[27–29] The schematic of the model is depicted in Figure 1.4. It is suggested that the rate determining step for ionic transport in such an SEI is the intergrain transport of lithium-ions and the structure is more or less determined by the order of decomposition. It is generally accepted that a solvent co-intercalation into the carbon – as stated by Besenhard et al.[17] – occurs besides surface SEI formation and influences the further formation of the interphase (see also Figure 1.2).[30]
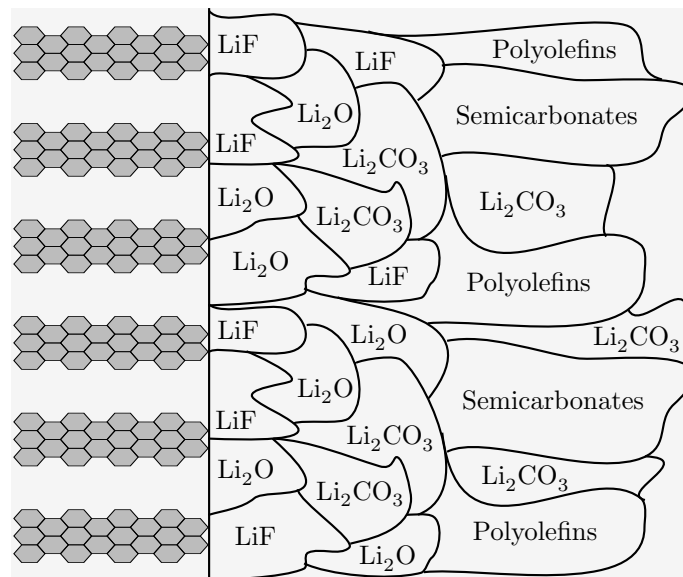

Figure 1.4: Schematic of SEI structure comprised of different degradation products as suggested by Peled in 1997. The newly emerging species include LiF, Li_2O, Li_2CO_3, semicarbonates and polyolefins.[26]

Zhang et al. propose a formation over the whole potential window of graphite where the SEI is of a simple and porous consistency at potentials above 0.25 V and becomes insulating and denser at potentials below 0.25 V.[31] El Ouatani et al. further showed that the SEI, once formed, is very stable and does not dissolve upon discharge.[32]

As mentioned before, additives are one possibility to improve lithium-ion batteries.[33] Based on their intended target, different classes of electrolyte additives can be distinguished which will be discussed in Section 2.1. Although research efforts toward SEI improving additives were extensive in the decade prior to 2004, limited literature is available on implemented additives because of commercial

interests.[4,34]

The importance of interphases are based on the fact that interfaces between electrode and electrolyte are the only site for charge transfer in an electrochemical device. Instead of being of a 2D nature, due to the adherent degradation products the charge exchange happens in a 3D electrolyte interphase zone, the SEI. In a paper by Winter it was called "the most important but least understood component" in lithium-ion batteries.[1] Despite lots of research work and insights gained in past years, a lot of unsolved problems in understanding basics of SEI constitution and the associated formation remain.

One such example for ongoing debates is the actual structure of the SEI. Whereas some groups[35,36] report a two layer structure with inorganic compounds close to the electrode and organic decomposition products reaching into the electrolyte, Nie et al. contradicts those findings and proves a single layer structure.[37–39] Even the found components are contested as can be seen in an overview by Verma et al.[2] (which was updated and complemented by An et al.[11]) in Table 1.1

Table 1.1: List of SEI components on the graphite/electrolyte interface. The reported number of literature references in which their presence or absence is experimentally verified and the role of those components (Notes) were reported by Verma et al.[2] and An et al.[11] (number in parentheses). Components not mentioned in one of the reviews are marked with [nm].

Component	Present	Absent	Notes
$(CH_2OCO_2Li)_2$	5 (4)	– (–)	As a two electron reduction product of ethylene carbonate (EC) mostly found in the SEI of the EC based electrolytes.
$ROCO_2Li$	5 (4)	– (–)	Semicarbonates are present in the outer layer of the SEI and are absent near lithium.[40] They are found in most propylene carbonate (PC) containing electrolytes, especially when the concentration of PC in the electrolyte is high.
Li_2CO_3	4 (4)	4 (4)	Not always present.[41] Normally present in the SEI formed in EC or PC based electrolytes. It may also appear as a reaction product of semicarbonates with HF or water or CO_2.
ROLi	7 (5)	– (–)	Most commonly found in an SEI formed in ether electrolytes like tetrahydrofuran (THF), but also appears as dimethyl carbonate (DMC) or ethylmethyl carbonate (EMC) reduction product.[42] Soluble and may thus undergo further reactions.[43]
LiF	3 (3)	– (–)	Mostly found as a major salt reduction product in electrolytes comprising of fluorinated salts like $LiAsF_6$, $LiPF_6$, $LiBF_4$. HF contamination also reacts with semicarbonates to give LiF as a byproduct especially during storage.[44]
Li_2O	3 (3)	3 (4)	Might be a degradation product of Li_2CO_3 during Ar^+ sputtering in the XPS experiment.
Polycarbonates	2 (2)	– (–)	Present in the outermost layer of the SEI, close to the electrolyte phase. This part imparts flexibility to the SEI.
LiOH	3 (3)	2 (2)	Mainly formed due to water contamination[45,46] as a result from reaction of Li_2O with water or with aging.[47]
$Li_2C_2O_4$	2 (2)	– (–)	Found to be present in 18650 cells assembled in Argonne National Labs containing 1.2 M $LiPF_6$ in EC:EMC (3:7) electrolyte. Lithium carboxylate and lithium methoxide were also found in their SEI.[47]
HF	[nm] (2)	[nm] (–)	Formed from decomposition of $LiPF_6$ and water in the solvents. Highly toxic and can attack components of the cell.[11]
HCOLi	1 ([nm])	– ([nm])	Present when methyl formate is used as co-solvent or additive.

In summary, an ideal SEI should have minimum electronic and maximum lithium-ion conductivity.

SEI formation kinetics should be fast, allowing it to form completely before the onset of lithium-ion intercalation. In other words, the SEI formation potential should be more positive than the lithium-ion intercalation potential. An ideal SEI should have uniform morphology and composition. It should contain stable and insoluble passivating agents like Li_2CO_3 rather than metastable and poorly passivating ones like ROLi and $ROCO_2Li$. With that, a good SEI should be a compact layer adhering well to the carbon. It should be elastic and flexible to accommodate non-uniform electrochemical behavior and active material breathing.[2] The knowledge of improving surface properties and connected SEI build-up is a main factor for future lithium-ion battery improvement.[12]

1.5 Interphase on cathodes

The formation of the cathode interphase is caused by thermodynamic instabilities and occurs mostly in three stages. First, the surface gets already covered during the manufacturing process by natural degradation, i.e. oxidation. Second, reactions of this native surface film will happen at first contact with the electrolyte and third, chemical rearrangements due to formation will exist.[10] Cathode surface films were disregarded for a long time and, therefore, no uniquely defined name was established for the cathode film. For example, Winter et al. call it a cathode electrolyte interphase (CEI)[48–50] Edström et al. a solid permeable interphase (SPI),[51,52] and more generally some groups call it an electrode-electrolyte interphase (EEI).[53–55] One of the reasons that cathode films were disregarded so long could be that during production (synthesizing) of transition-metal oxides Li_2CO_3 already develops due to reaction with the atmosphere. Li_2CO_3 later is one of the main components of the cathode surface layer.[4]

Although the exact composition of the cathode layer is still not clear, certain dependencies of the resulting thickness could be observed. The cathode layer thickness seems to be independent of the degree of lithiation but increases steadily with temperature and storage time. The cathode interphase is believed to be ionically more conductive than its anode counterpart but also to grow faster during cycling. Based on this behavior, the cathode interphase takes over as the limiting resistance parameter during aging. Due to the considered dominance of the impact of SEI growth during the first cycles, research activities rather focused on the formation of passivation films on the anode side compared to the cathode side.[4,10]

1.6 Methods for interphase characterization

Characterizing the aforementioned interphases is very challenging due to the elusive nature of the interphases in ambient atmosphere. Special in-situ or in-operando characterization techniques are required to gain knowledge about the interphases' chemical and structural composition in a cell without opening and thereby possibly altering the composition or introducing artifacts.[10,56] A recent review by Cabana gives an overview of analyzing methods used for interphase characterization. The following chapter is based on the roundups by Cabana[57] and Xu[10] and introduces each technique briefly.

Cabana differentiates between several classes of characterization techniques. Namely those are electrical techniques (i.e. electrochemical impedance spectroscopy and similar pulse techniques), vibrational spectroscopy (i.e. infrared spectroscopy and Raman spectroscopy), X-ray based techniques (i.e. X-ray photoelectron spectroscopy and X-ray absorption spectroscopy), microscopy (i.e. scanning probe

microscopy, electron microscopy and spectromicroscopy), UV-visible techniques (i.e. UV-visible spectroscopy and ellipsometry), neutron based techniques and others such as ion-exchange chromatography, electrochemical quartz crystal microbalancing and nuclear magnetic resonance.[57] The best-known and/or most-widely used techniques will be introduced in the following paragraphs.

Electrical characterization One way to characterize the SEI and its growth in-operando are electrical characterization techniques like pulse tests or electrochemical impedance spectroscopy (EIS). By exciting the system "cell" with an electrical signal (current or potential) and measuring a respective response, an impedance of the system can be obtained.[58] Although a mid- to high-frequency range can be assigned to the internal resistance where the SEI resistance poses a significant, altering part, electrical characterization techniques can never fully describe the SEI as other parts of the full cell setup contribute to the response signal as well.[59]

By reducing the components of the cell setup in laboratory cells and including reference electrodes, the growth of a passivating layer can be partially accessed by carefully analyzing measurement results. Further research might lead to a better understanding of the impedance interpretation and, therefore, qualify electrical characterization techniques as the technique of choice.

Vibrational spectroscopy Infrared (IR) spectroscopy works on the principle that IR light interacts with vibrations in atomic bonds of molecules. The measured signal is a vibrational "fingerprint" that can be associated with certain bonds known from previous experiments. The best-known technique Fourier transformed infrared spectroscopy (FTIR) is widely used in interface chemistry. FTIR is especially sensitive to organic products which covers only parts of the SEI and leads to a strong noise by the electrolyte.[2,60] Ex-situ preparation of a sample which is often chosen to avoid those interfering signals, changes the sample and, therefore, the measurable results.

Raman spectroscopy is another well-known technique based on vibrational excitation leading to inelastic scattering of photons. In contrast to IR spectroscopy, Raman spectroscopy monitors bond polarizability and not dipole interactions. The shortcomings in an experimental way are much the same as priorly discussed for IR spectroscopy.[41]

X-ray based techniques The most common X-ray based technique in lithium-ion battery research is X-ray photoelectron spectroscopy (XPS) and is based on the emission of electrons from within the material.[2] Due to the short escape length of those electrons, the analyzable depth of the SEI is only about 10 nm and experiments have to be performed in ultra-high vacuum.

Beside XPS, another X-ray based technique is X-ray absorption spectroscopy (XAS) and it detects the absorption energy of X-ray photons. In contrast to XPS measurements, a high photon flux is required for XAS measurements that only synchrotron beams can provide.[61,62] An advantage is that photo-electrons as well as fluorescent photons are emitted which enables a certain depth profiling if two detectors are available.

Microscopy Electron microscopy, e.g. scanning electron microscopy (SEM) and transmission electron microscopy (TEM), allows for direct visual measurements of passivation films.[37] Sample preparation normally requires cell opening and contamination or alteration of the sample can not be excluded in data interpretation. Also interaction of the SEI with the electron beam are commonly expected.

Microscopy techniques become especially interesting when they get coupled with spectroscopic techniques like electron dispersive X-ray spectroscopy (EDX) – also called EDS or XEDS – and electron energy loss spectroscopy (EELS) that provide further information by using the interactions of the microscopy electrons with the investigated probe.[37,62] These coupled investigation methods are often referred to as spectromicroscopy.

An alternative microscopy class is scanning probe microscopy (SPM) which is based on the effect that a physical tip is moved based in a piezoelectric mechanism.[62,63] Common representatives are scanning tunneling microscopy (STM) and atomic force microscopy (AFM). One drawback so far has been the requirement of a relatively flat surface, so investigations have been focused on metal electrodes or highly oriented pyrolytic graphite (HOPG) as a close-enough substitute for standard graphites.

Neutron based techniques Studies of the SEI using neutron based techniques are still very rare and were done on substitute materials to commonly used graphite. The potential of neutron based techniques to become the technique of choice is quite high since – in contrast to X-rays – lithium and hydrogen can be made visible and neutron based techniques are non-destructive. The limited availability to neutron sources and the strong hydrogen signal originating from commonly used electrolytes hinders widespread research efforts so far.[62,64]

Other techniques Other techniques that cannot be categorized in one of the previously introduced classes are ion-exchange chromatography, electrochemical quartz crystal microbalancing (EQCM) and nuclear magnetic resonance (NMR).

Kren showed the correlation between capacity fade and lithium-ions trapped in the SEI by harvesting cycled anodes, dissolving them in pure water and analyzing the lithium and fluoride concentration with ion-exchange chromatography.[65] While the amount of detected trapped lithium-ions and capacity fade had a good agreement, no statement on the SEI constitution could be made.

EQCM is a useful technique to detect potential thresholds at which decomposition reactions occur. As soon as several reactions happen in a similar potential window, previous knowledge is necessary for data interpretation.[57,66,67]

The advantage of NMR is the insight into ratios of different elements inside a probe. Every element has an isotope that is magnetically active and can therefore be measured after magnetic excitation.[54,68] Challenges arise when transition-metals can be found within the sample as they distort the signal. Also the presence of hydrogen stretches the signal and the most abundant isotope of carbon (^{12}C) is inactive for NMR excitation.

To summarize the above introduced techniques, every technique contributes to the understanding of the SEI growth and its composition but none of the stated techniques, by itself, is able to completely characterize the interphases on electrodes so far. A combination of several methods, however, can be able to compose a rather profound insight into interphase constitution. The desirable all-rounder for characterizing the SEI has yet to be developed.[56,57]

1.7 Scope of this work

When talking about SEI formation, two basic cases have to be considered. First, there is an initial SEI growth during cell production – called formation process – and then the growth over the lifetime of a cell due to the non-ideal properties of the initial SEI. Ideally, we would like to explore both stages individually but they cannot be separated as the formed SEI during the formation process determines the behavior during the further lifetime of the cell.

As mentioned before, there are still difficulties to measure the SEI properties and this aspect applies especially to the SEI right after the formation process. Understanding the parameters and variables that have to be considered prior and during the formation cycle is an ongoing challenge. Examining and modeling the behavior over the lifetime of a cell can be one possibility to get insights into the requirements, such as thickness or conductivity for passivating behavior, of a functioning SEI. Setting up a model to describe cell aging behavior is, therefore, one goal of this thesis.

Chapter 2 summarizes known influencing factors of the formation process. The summary reviews cell-dependent variables such as the electrolyte, the electrodes and the separator as well as process variables starting with the filling process and subsequent charging and temperature profiles. Due to the many interdependencies between the different used materials and their varying responses to the same process parameters, no universally valid set of parameters for the formation process can be derived.

Lithium-ion batteries are one of the most promising candidates for energy storage in future stationary storage systems and electric vehicles.[5,69,70] Enormous research efforts have been conducted to get a thorough understanding of the system "lithium-ion cell" and to further develop it for higher energy and power density, higher safety standards as well as longer cycle life.[71] The implementation of an aging model as introduced in Chapter 3 offers the possibility to describe the capacity and power fade of a lithium-ion cell over its lifetime. In comparison with measurement data of an lithium nickel cobalt manganese oxide (NCM)/graphite cell aging study, values for SEI growth by non-ideal insulating properties and cracking due to graphite expansion as well as conductivities for electrons and lithium-ions inside the SEI can be extracted from the model. Analyzes of the developed aging model show a non-homogeneous SEI growth through the graphite electrode. The SEI thickness close to the separator with about 600 nm is almost three times thicker than at the current collector/electrode interface with about 250 nm SEI thickness. A further goal of this thesis is to derive requirements for an electrode design that ensures a homogeneous SEI growth through the electrode over the lifetime of a cell to decrease the overall capacity fade.

The non-uniform SEI thickness is caused by an inhomogeneous current density distribution throughout the cell. The resulting inhomogeneous lithium-ion distribution leads to equilibration effects that can be recorded via EIS measurements which are introduced in Chapter 4.3. A hypothesis of three equilibration processes is derived from the long-term relaxation times and partially recreated by a model that accounts for two of the three equilibration pathways. To verify the model predictions, a laboratory cell consisting of multiple working electrode layers is used to measure intra-particle and inter-particle equilibration within a graphite electrode. The measurement setup and procedure are presented in Chapter 4.4. The implementation of the multiple working electrode design in a physicochemical model is introduced in Chapter 4.5. Besides the multiple working electrode, the model incorporates a particle size distribution in the otherwise homogenized model for the first time. With the model, an electrode design variation study is performed focusing on different combinations of porosity and tortuosity as those parameters can primarily be adjusted during electrode production. An electrode that includes

pore channels perpendicular to the electrode layer offers a distinctly more homogeneous current density distribution during cell operation.

The conclusion in Chapter 5 finally incorporates the improved electrode design into the aging model and offers a summary of proposed future research issues.

2 Factors influencing SEI Formation

As the formation process of a lithium-ion battery has a strong influence on the constitution of the SEI, this chapter will take a closer look into the formation process as one of the final production steps. In lithium-ion batteries, the SEI has two purposes which are the protection of the electrolyte from electrochemical reduction on the lithiated anode surface, and the protection of the anode material from chemically reacting with the electrolyte.

The importance of the formation step can be seen in the loss of cyclable lithium. During formation of the SEI 8 to 15 % of the cyclable lithium is consumed.[72,73] This amount is dependent on cell parameters such as e.g. active material particle size, carbon type, electrode porosity and the choice of electrolyte as well as process parameters like the charging current or temperature profile.[73] Those two paths can be seen in Figure 2.1 and will be elaborated in the following sections.
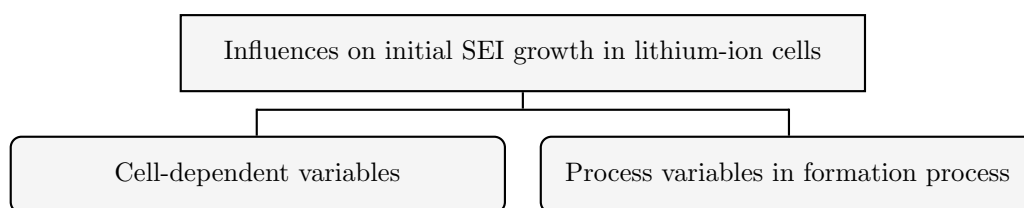
Figure 2.1: Influences on the initial SEI growth in lithium-ion cells during formation originate from cell-dependent factors as well as process variables controlling the formation regime.

2.1 Cell-dependent variables

A typical lithium-ion battery is composed of electrodes, a separator as well as an electrolyte and all those constituents influence the build-up of the passivating layers in a cell. As each of these three main components is a composite itself, a subsection is dedicated to each component.

2.1.1 Electrolyte components

An electrolyte, as mentioned in Section 1.3, consists of a conducting salt containing the intercalating species, a liquid solvent (polymers of all-solid state batteries are not considered here, although same principles apply) and possibly additives to achieve certain special properties. The composition of the electrolyte is a determining factor in the nature of the passivating film formed[72] and, therefore, the impact of all three electrolyte components on SEI formation will be described in the following paragraphs.

Conducting salt   The second indispensable component of a working electrolyte is the conducting salt that is responsible for transporting ions in the liquid phase. Used salts are, as previously mentioned,

$LiPF_6$, $LiClO_4$, $LiBF_4$ and others. Only fluoride containing salts decompose to LiF which is a thermodynamically stable salt product close to the electrode.[4,10,53] Its good passivating properties against electron flux are unfortunately coupled with a high ionic resistance.[53] The choice of the conducting salt, therefore, strongly influences the ratio between organic and inorganic components in the SEI.[41]

$LiPF_6$ is also prone to generate toxic HF with traces of water contaminating the electrolyte. By electrolyte oxidation, HF leads to transition-metal dissolution at the cathode. The transition-metal ions can then diffuse toward the anode and become reduced to form an ionically more resistive and porous SEI leading to a higher capacity fade.[74] Decomposition of electrolyte salts containing fluoride starts occuring at potentials lower than $1.5\,V$ vs. Li/Li^+.[72]

Solvent Current lithium-ion batteries incorporate mixtures of cyclic and linear carbonates as the solvents for the electrolyte. Linear carbonates such as DMC or DEC form homogenous mixtures with cyclic carbonates such as EC or PC and increase the ionic conductivity as well as the thermodynamically stable window compared to pure cyclic carbonates. While mixing the solvents was one reason for the successful implementation of lithium-ion batteries, realizing that EC does not co-intercalate into the graphitic structure but rather develops a passivating SEI was another important step.[4,10]

Research was also carried out to explore e.g. phosphorus-, silicon- or sulfur-based solvents, but until today, cyclic carbonates are the widest-used electrolyte solvent as their decomposition products – Li_2CO_3 and $ROCO_2Li$ – form a good passivating film.[4,10]

Additives The most important area for future research regarding the influence of the electrolyte on SEI formation is the area of electrolyte additives. Based on their intended target, several classes of electrolyte additives can be distinguished. Those categories namely are (i) conductivity enhancing additives for improving overall bulk electrolyte conductivity, (ii) additives to enhance safety behavior of the batteries, (iii) cathode protecting additives, (iv) SEI improving additives and (v) others for niche applications as e.g. additives for improving lithium deposition on lithium-metal electrodes.[4,75]

SEI improving electrolyte additives usually do not exceed a share of $5\,\%$ (either weight or volume) of the total electrolyte, as their intention usually is not to change the bulk properties (conductivity, viscosity, liquid temperature range) of the electrolyte but to offer a cost-effective method for improving the SEI formation of a well-established electrolyte.[34,75] There are numerous electrolyte additives improving one aspect of battery performance, unfortunately most of the time this is counterbalanced with a negative impact for another performance property.[75] In the following, the focus will be on SEI forming and cathode protecting electrolyte additives as they have the biggest impact during the formation process.

The purpose of incorporating SEI forming, reductive additives in the electrolyte is that they decompose prior to any of the solvent and salt components and build a preliminary SEI film. During formation, EC for example decomposes in two stages. Before lithium-ion intercalation, a porous, highly resistive (with respect to lithium-ion diffusion) SEI is formed. Later during lithium-ion intercalation, the SEI becomes more compact and more ionically conductive.[75] The built-up SEI in additive containing electrolytes is generally less resistive toward lithium-ion transport than an SEI formed in neat electrolyte.[76]

Besides the aforementioned additive type which reacts prior to solvent dissolution, two other types of SEI forming additives are distinguished. One is a scavenger-like additive to reduce radical anions that attack the SEI and the other intends to modify the existing SEI morphology, e.g. dissolving inorganic, low conductive species from the SEI to form more beneficial species.[75] The overall intended use of

SEI forming additives are (i) reducing gas generation, (ii) reducing irreversible capacity loss and (iii) stabilizing the SEI during cycling.

One of the most successful and known commercially used additive is VC,[10] as it has a beneficial, passivating influence on the anode side of a lithium-ion cell and is not coupled with any negative effects on the cathode side.[77] The reduction potential of VC is about the same as of EC (~0.8 V vs. Li/Li$^+$),[78] so it fits the basic, known requirements. VC is very effective for the formation of the SEI, however when too much VC is introduced into the electrolyte, it leads to low cycling efficiency and a higher self-discharge of the cell.[75]

Other researched SEI forming electrolyte additives are vinyl ethylene carbonate (VEC) and fluoroethylene carbonate (FEC)[78] but little is known about which additives are commercially incorporated.[4] VEC and FEC are reduced at higher potentials than VC between 1.4 and 0.9 V vs. Li/Li$^+$.[78] The interest in FEC is mainly based on the possibility to decompose into an HF and a VC molecule which are believed to have both positive influences on cyclability when lithium-metal electrodes are used.[75]

Electrolyte additives protecting the cathode can be categorized in additives scavenging water as well as acidic impurities and additives scavenging dissolved transition-metal ions to include them in the electrode-electrolyte interphases.[75] Especially manganese containing cathodes are prone to be attacked by HF and to release manganese-ions. Not only will this dissolution decrease the capacity of the cathode, the manganese-ions will react with the electrolyte and deposit as an ionically poor conducting salt in the anode SEI.[19,74] The benefit of scavenging additives, therefore, is quite obvious.

2.1.2 Electrode composition

Another main influence on the SEI is represented by the electrodes of the chosen cell. First, the choice of anode and cathode determines a thermodynamical window in which the electrolyte needs to be stable or otherwise the electrolyte will be reduced and/or oxidized. Also other factors like e.g. the active surface of the material and the overall thickness as design parameters influence the capacity needed to form a passivating SEI.[72] A closer look will be given in the subsequent paragraphs to the factors regarding mainly the electrodes.

Electrode chemistry Typical anode materials used nowadays are graphite and in niche applications lithium titanate (LTO). Also lithium-metal and other possibly future anode materials like silicon (Si) and tin (Sn) alloys should be considered.

As the onset potential for SEI growth is believed to be in the order of 1.0 V vs. Li/Li$^+$, it is important to look at the average potentials of the mentioned anode materials. Graphite has an average potential of 0.1 V vs. Li/Li$^+$ which makes it such an interesting candidate as an anode with a potential close to lithium-metal. Si is at about 0.2 V and Sn at 0.3 V vs. Li/Li$^+$ when considering a theoretical Li$_{4.4}$M phase (M = Si or Sn).[53] LTO in contrast has a potential of 1.55 V vs. Li/Li$^+$ and is, therefore, often considered an anode without an SEI.[79] Still, a passivating layer without a major degradation impact can be found on LTO whether it is called SEI or not.[54,80,81]

The SEI layer on Sn anodes is similar to graphite and mainly consists of Li$_2$CO$_3$, LiF and organic molecules. On Si anodes the SEI is build-up mostly by Li$_2$O and Li$_4$SiO$_4$.[20]

The problem that arises with alloy materials containing Si and Sn is the large volume change during intercalation.[53] Each expansions leads to a cracking of the SEI and, therefore, the exposure of unpassi-

vated surface that will experience passivation by new SEI build-up.[82] Due to lithium-ion consumption during new SEI formation, the lifetime of current commercial cells with Si anodes is limited to 300 – 500 cycles.[83] Graphite in contrast expands just about 10% during cycling and shows a rather stable SEI because of that.[84,85] LTO is considered a zero-strain material which means that there is no expansion and a stable passivating film can form.[8,79,81]

The influence of the cathode chemistry is more indirect than that of the anode. Transition-metal ions from every known cathode material dissolve from the cathode bulk into the electrolyte[86] by HF acid attack of trace water after manufacturing. The dissolution of transition-metal ions from the cathode and the subsequent transport to and incorporation into the anode surface film promote the growth of more SEI.[30,87] The main effect of e.g. manganese dissolution is an impedance rise on the anode as manganese-ions get incorporated in the SEI[88,89] and are blocking lithium-ions from (de-)intercalation into the graphite as well as forming cracks in a more porous SEI.[90]

Electrode morphology   The morphology and chemistry of the graphite used as the anode, influence the formation process and determine the SEI products.[75] The amount of lost lithium-ions depends on the active material particle size, carbon type and also electrode porosity as well as tortuosity.[73]

Darling et al. showed that a homogeneous particle size leads to a more homogeneous utilization of an electrode[91] and therefore, more homogeneous SEI distribution. Also particles with a radius smaller than $5.5\,\mu m$ are almost not affected by mechanical degradation (just 1.5 to 2%), whereas this influence increases with bigger particles (3.5% at $8.5\,\mu m$ radius and 10% at $12.5\,\mu m$ radius).[92] This degradation then leads to cracking and re-formation of the SEI.

Spherical particles show a more homogeneous utilization when compared to platelet-shaped and ellipsoidal-shaped particles[93] as their impact on tortuosity and consequently diffusion limitations is the lowest.[94] Also different shapes have an impact on the basal to edge plane ratio of the particles and Bar-Tow et al. previously showed that the SEI on edge planes is about 50% thicker than on the corresponding basal plane.[25] Finally, the particle size and shape in connection with the porosity of the electrode determines the overall surface area that has to be covered by an SEI.

Electrode balancing   Cells are commonly assembled in a way that the cathode is oversized capacity-wise whereas geometrically the anode exceeds the cathode. The capacity oversizing of the cathode is due to the initially predicted losses of lithium-ions within SEI formation[72] and the goal to have a balanced system after formation for a maximum energy density. The geometrical oversizing of the anode is due to high overpotential developing on the edges of graphite anodes that can enhance the probability of lithium-plating.[95,96]

Electrode balancing also determines the operating window of each electrode, as the cell during operation is controlled by a potential from outside. During charge and discharge, lithium-ions are intercalated into or deintercalated from the electrodes until the respective potential difference is reached. Depending on the local potential of the electrodes, side reactions like electrolyte decomposition for SEI and CEI growth as well as transition-metal dissolution are promoted or inhibited.[73,97]

Electrode thickness   One of the main goals in recent efforts in research and development has been to achieve an increase in energy density. Increasing the electrode thickness to relatively decrease inactive parts in the cell, is one way to achieve this goal.[98,99]

Unfortunately, increasing the electrodes' thickness leads to diffusion limitations of lithium-ions within the electrolyte volume fraction of the electrodes.[99] The diffusion limitation results in an inhomogeneous distribution of the electrolyte potential and thereby influences the overpotential for both the intercalation/deintercalation and the SEI forming side reaction. When using thick electrodes, a satisfyingly good lithium-ion transport has to be assured.[93,99]

Another challenge that can arise from thick electrodes is their manufacturability. Due to mechanical stresses during the drying of the slurry, cracks in the coating can develop[100] and thereby significantly increase the surface area which will lead to a larger area where SEI is formed. Calendering those thick electrodes ensures a better contact between the particles and, therefore, lowers the impedance of the electrode.[101]

Electrode composite The electrode composite consists of a mixture of active material, additives to enhance e.g. electronic conductivity and a binder to assure mechanical stability. Whereas the influence of the active material has been discussed before, electrode additives and the binder can also influence the composition of the SEI.[53]

The most commonly used binder is poly(vinylidene fluoride) (PVdF) as it shows a good compromise between stability against mechanical stresses during cycling, electrochemical stability and environmental friendliness.[32] As PVdF leads to additional safety problems during a thermal runaway and can only be processed with environmentally unfriendly *N*-methylpyrrolidone (NMP), research and development are exploring water soluble binders such as carboxymethylcellulose (CMC), polyacrylic latex and acrylate polyurethane.[32,100] Electrodes with water soluble binders experience higher in-plane pressure during drying and are more prone to crack propagation as well as contact loss of particles.[100] Also, due to residual water contamination in contact with the electrolyte more HF is formed[100] which leads to an SEI increase and a decrease in ionic conductivity. The drying conditions can also influence the binder distribution, as high drying rates result in a binder accumulation on the electrodes' surface which blocks the reactive surface area.[102] The influence of binders is therefore not a direct one as SEI is not formed on the binder[103] but an indirect one due to contaminants that are incorporated by binder processing.

Additives such as sodium maleate[104] and 1-pentylamine[105] can be coated on the electrode to form a pre-SEI. That pre-SEI layer can then be transformed into a normal SEI with a lower loss of cyclable lithium during formation. Also the internal resistance can be reduced by realizing a pre-SEI.[105]

2.1.3 Separator

The separator does not actively participate in the reaction and storage properties of a cell but influences the formation process due to its properties allowing for lithium-ion transportation. As will be revisited in Section 2.2, the wetting process is very important to determine which areas of the electrode will be electrolytically connected to the overall system. By improving the diffusion properties of the separator and/or adding wettability enhancers, the electrolytic connection can be affected.

Diffusion properties Separators can be classified in microporous polymer membranes, non-woven fabric mats and inorganic composite membranes ("ceramic separators").[106–108] Depending on their structure, those separator types differ in their thickness, pore size, porosity and permeability proper-

ties, all of which influence the ionic transport in the electrolyte. The ideal separator has a minimal thickness and high porosity comprising small pores to achieve a low tortuosity and, therefore, inner resistance.[106–109] Those ideal separator properties also lead to smaller gradients in the lithium-ion concentration and subsequently electrolyte potential through the cell stack which ensures a more homogeneous overpotential triggering SEI growth.[109]

Wettability enhancers Improving the wettability of the separator can be done by either electrolyte additives and/or special treatment of the separator.[106]

Wetting agents in the electrolyte are used to accelerate the wetting process of the non-polar separator when the electrolyte incorporates a significant amount of cyclic carbonates. Many overcharge-protection additives also work as wettability additives due to their non-polar nature.[75] A second way to improve the wettability of the separator – and in this case also of the electrodes – by electrolyte additives, is using additives that reduce the viscosity of the electrolyte.[75] One example for such an additive is phosphorus pentoxide (P_2O_5).[110]

Special treatment of the separator surface includes applying a hydrophilic surfactant or grafting with hydrophilic functional groups.[106,107] Prior to manufacturing, applied surfactants can be dissolved in the electrolyte and, so, only intervene during the initial wetting process.[111] The preferred method for retaining the electrolyte in the separator during cycling is, therefore, surface grafting.[106]

Overall, the purpose of adding wettability enhancers to separators is to obtain a homogeneous wetting of the separator as dry spots increase the impedance and lead to an inhomogeneous distribution in current density[106,108] and consequently SEI formation.

Summarizing all of the above mentioned and described influences of cell-dependent variables in Figure 2.2, we see that the components responsible for the operation of a lithium-ion battery also affect SEI formation.
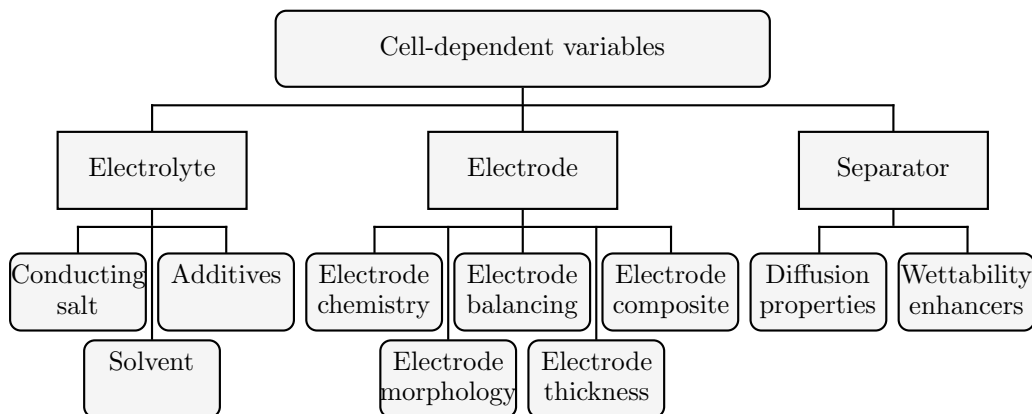
Figure 2.2: Variables influencing SEI formation that are preset during the production of a lithium-ion cell by choice of material or construction. All electrolyte components affect the growth of the SEI, as well as the composition and certain design parameters of the electrode. Even properties of the inactive separator influence the overall performance regarding SEI build-up.

By the choice of a certain material mix for the electrode, the electrolyte as well as the separator,

certain default settings for the SEI formation are already given.

2.2 Process variables in formation process

The filling of the electrolyte – which signifies the first contact between electrode and electrolyte – is the beginning of the formation process. After the filling process different temperature and cycling profiles can be applied that influence the formation of the passivating layer. For that reason a section is dedicated to each of the influencing processing steps.

2.2.1 Electrolyte filling

Filling the electrolyte into the cell housing is a crucial step in terms of product quality and cost. Therefore, the filling process as well as the time between filling and applying the first charging current to the cell is elucidated subsequently.

Filling process   The filling process itself is challenging due to the encapsulated residual surrounding air inside the cell housing and the pores of the electrodes as well as the separator.[112] For applying the liquid electrolyte to the cell, the electrolyte is trickled on the edges of an electrode stack or jelly-roll. To achieve a homogeneous wetting of all pores, usual wetting times are in the order of 12 to 24 h.[113] Depending on the type of cell housing, i.e. prismatic, cylindrical or pouch, vacuum is applied during wetting.[113–115] Calendering of electrodes with smaller particle sizes leads to the formation of very fine channels that trap residual gas.[116] As stated before for the influence of the separator, an inhomogeneous wetting leads to hot spots as well as an inhomogeneous current density distribution and, hence, to an uneven SEI.[11]

Wetting time   As mentioned above, the time for wetting is normally in the order of 12 to 24 h. One way to foster the wetting process, is to heat up the cells to decrease electrolyte viscosity and to allow for a better permeation into the pores.[11] As lithium-ion batteries are assembled in their discharged state, the cathode electrode potential is about 0.2 V more positive than that of the anode electrode during this time before a first formation current is applied.[117] This results in an oxidation of the copper current collector foil and a dissolution of copper-ions into the electrolyte.[117] Subsequent formation and cycling incorporates copper-ions into the SEI or leads to copper dendrite formation.[118] Possibilities to prevent copper dissolution by leaving the oxidative potential window are to apply a short current pulse or to use pre-lithiated graphite.[118]

2.2.2 Cycling profile

Standard formation profiles are conducted with small current rates (~C/10 and lower) in a constant-current/constant-voltage regime for about 3 cycles. During the additional cycles the current rates are often increased (~C/5).[119]

Reported influences of variations on that standard profile are presented in the following paragraphs.

Current rate   As a low charging current rate is supposed to lead to a more homogeneous and more stable passivating SEI, this is incorporated in the standard formation protocol.[119–121] Literature shows current rates of C/30,[122] C/24,[120] C/20[123,124] and C/10[125] for the first cycle. If subsequent cycles are included in the formation protocol, the charging current rate is often increased to shorten the overall formation process.[122,123]

Studies using a C/5 rate from the beginning showed promising results when several cycles were included.[122,123] Another approach to shorten formation time can be applying a time-dependent current profile. He et al. started with a C/20 current rate up to a full cell potential of 3.0 V, then stepped up the current to C/10 until a potential of 3.85 V was reached and finally applied a C/5 rate until arriving at the end-of-charge potential of 4.2 V.[124]

Also, it can be assumed that the benefit of low charging rates is based on the long duration of the formation during which an incomplete wetting can be finished. In contrast, already perfectly wetted cells where all pores are penetrated by electrolyte can be formed with a higher current rate as all active material particles are electrolytically connected.

Cut-off potential   Electrolyte (solvent) decomposition and formation of inorganic components of the SEI such as Li_2CO_3 and Li_2O starts at potentials above 0.3 V vs. Li/Li^+ while organic species are already formed at higher potentials.[53] For that reason, reducing the upper cut-off potential was investigated by several research groups.[120,122,125] They found that with a full cell potential of about 3.7 V the cell was sufficiently passivated for further cycles.[122,125]

The findings that in a potential range between 0.25 and 0.04 V vs. Li/Li^+ the re-formation into a protective SEI takes place[31] is supported by the data of Gering et al.[120] and An et al.[123] They used several cycles up to 4.2 V but did not discharge the cell afterward to shorten the overall formation duration.[123]

Cycle number   The definition of the cycle number after which formation is concluded is a major point of discussion. While the SEI is believed to be completely formed after 10 cycles,[58] only the very first charging cycle is called *the* formation cycle.[126] A general definition can be given by defining all cycles prior to the intended utilization of the formed cell as the formation cycle(s). However, it has to be noted that the main SEI formation occurs within the very first charging half-cycle.[126]

Laboratory experiments often include about three formation cycles to ensure a stable SEI for the subsequent experiment.[11,50,89,127,128] In studies investigating the formation process itself, a differentiation between full cycles[120] and partial cycles[123] is needed. Whether full or partial cycles were incorporated in the formation protocol, the findings were similar. For a stable passivating SEI that leads to a subsequent coulombic efficiency close to 100 %, 4–5 cycles proved to be beneficial.[120,123]

2.2.3 Temperature

Regarding the temperature, limited literature is available although one would expect a high influence due to the temperature dependency of all kinetic and transport phenomena. An extended study on the temperature dependency of a fixed electrode/electrolyte combination would be appreciated. The following paragraphs summarize the insights of temperature influences on the formation process gained as by-products from studies focusing on other aspects of formation factors.

There seems to be an optimum in terms of formation temperature around 45 °C, as cells formed at lower and higher temperatures show an increased inner resistance or higher capacity fade.[49,120,129,130] The optimum temperature might improve the wetting process, transport properties of the electrolyte and enhances the kinetics for a fast reaction. He et al. in contrast conclude that a lower temperature is beneficial for SEI formation. As they compare 25 and 50 °C, they might have missed the possible optimum as mentioned before.[124]

There are also reports that distinguish between the temperature influence on the different electrodes. While the formation losses of graphite electrodes increase with temperature, those of NCM were shown to decrease.[125] Another setback to consider is that at higher formation temperatures, the gas evolution is also increasing leading to higher stresses and possible particle disconnection.[126]

All previously introduced process variables are shown in Figure 2.3. Beginning with filling in the electrolyte, a process is started that can be influenced for better or worse by several settings without having an explicit set of parameters.
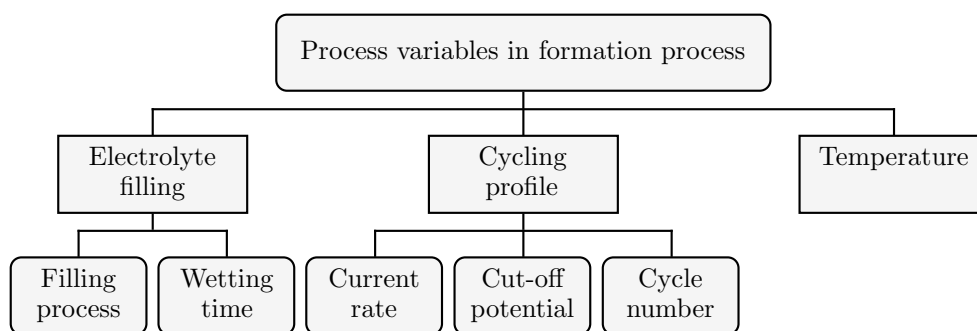
Figure 2.3: The formation process starts with the filling of the electrolyte. Afterward the cycling profile and ambient temperature are factors that determine the quality and success in the build-up of a sufficiently passivating SEI.

2.3 Summary of formation parameters

As there is still little public information available on the proprietary formation processes of lithium-ion batteries,[113] the preceding sections gave an overview on influencing parameters depending on cell properties and process variables.

The cell-dependent variables have a distinct impact on the formation of the attainable passivating layers. By choice of materials for the electrodes as well as the electrolyte and certain structural presettings, most SEI properties are already pre-determined. Additionally, due to the previously determined influence of the cell parameters, settings of the formation process show diverging and interconnected consequences.

Since no bijective correlations for formation procedure parameters can be found in literature, it becomes obvious why manufacturers keep their settings for their individual cells and processes proprietary. The interdependencies between certain material components and respective process parameters – e.g. an electrolyte additive and the formation temperature – also complicate the derivation of a universally valid formation regime from the previous sections.

Future work should address this gap by testing process variables while keeping cell-dependent variables constant and testing cell-dependent variables in a fixed process. This, of course, signifies a lot of research work associated with a high financial commitment. On the other hand, this seems to be the only sensible possibility to study and understand all the influences on the formation process.

3 Modeling of Capacity Fade Mechanisms

This chapter will give a brief, general introduction to capacity fade mechanisms in addition to SEI growth as reported in literature as well as to Newman's model as the basis for the implementation of selected degradation phenomena. With an extended Newman model, a new approach to SEI modeling is introduced and the growth of the SEI over a battery's lifetime is studied.

The aging behavior of lithium-ion batteries has been a focus issue of battery research since the introduction of lithium-ion cells by Sony in 1991.[131] Reviews by Agubra et al.,[60,132] Arora et al.,[72] Aurbach et al.,[133,134] Birkl et al.,[135] Broussely et al.,[136] Verma et al.[2] and Vetter et al.[137] are just a few examples of the extensive literature regarding aging behavior. Commonly accepted and experimentally verified aging phenomena as mentioned in the previously cited literature are electrolyte decomposition leading to SEI and CEI growth, solvent co-intercalation, gas evolution with subsequent cracking of particles, a decrease of accessible surface area and porosity due to SEI growth, contact loss of active material particles due to volume changes during cycling, binder decomposition, current collector corrosion, metallic lithium-plating and transition-metal dissolution from the cathode.
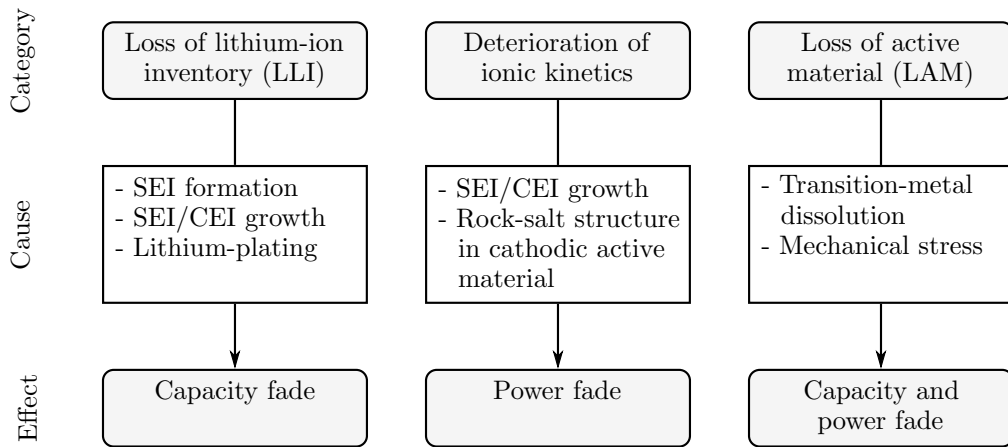
Figure 3.1: Categories of aging mechanisms associated with their respective causes and the effects they have on cell behavior.[73,136,138]

The listed aging mechanisms can be assigned to three different categories that are a loss of lithium-ion inventory (LLI), a deterioration of ionic kinetics and a loss of active material (LAM).[73,136,138–140] The LLI is synonymous to a decrease in the amount of cyclable lithium-ions as they are trapped in a passivating film on either of the electrodes or in plated metallic lithium. Due to the growth of the passivating layers and/or the formation of rock-salt in the cathode (remnant of the cathode active material after transition-metal dissolution), kinetic transport of lithium-ions through those inactive areas is limited and results in an impedance rise.[137,141] An LAM can be caused by the dissolution of transition-metal ions from the cathode bulk material, changes in the electrode composition and/or changes in the crystal structure of the active material which all decrease the host structure for lithium-ion intercalation. Also mechanical strain during de-/intercalation can contribute to LAM as particles

from both electrodes can crack and get electronically separated from the bulk material.[96,135] Figure 3.1 gives an overview of the described categories, their main causes and the effect on the cell's utilization.

The effects of capacity versus power fade on a voltage curve are shown in Figure 3.2. Whereas a capacity fade simply reduces the available amount of lithium-ions, a power fade reduces the available energy by decreasing the cell voltage while the capacity is not necessarily affected. Depending on cell utilization and surrounding conditions, lithium-ion cells will show a capacity as well as a power fade more or less pronounced.
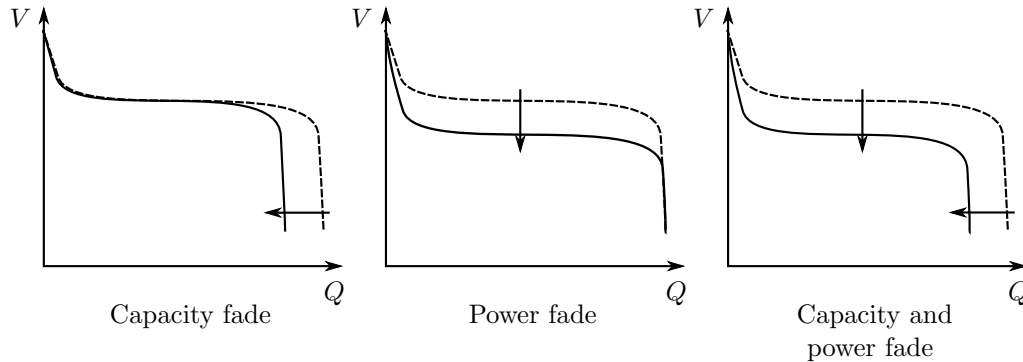
Figure 3.2: Resulting voltage curves after a capacity fade, a power fade or a combination of both (solid line) compared to a fresh cell behavior (dashed line).

After this brief overview on known aging mechanisms and their effects on cell behavior, a modeling framework for investigating cell aging behavior will be introduced as modeling represents a powerful tool for helping to understand the interactions between selected mechanisms.

3.1 Classification of modeling categories

For investigating or describing the behavior of lithium-ion cells, different model categories are implemented and those can be classified into first-principle, electrochemical engineered and empirical models.[142,143] An overview of the most prominent and applied models as well as their respective category is shown in Figure 3.3.

Atomistic models based molecular dynamics (MD)[66,144,145] and density functional theory (DFT)[146–148] try to recreate molecular behavior on an atomic scale. As they use fundamental physics-based approaches for atom-atom interactions, these models are also called first-principle models.[144] This category of models becomes of greater importance in future research efforts for better understanding interfacial chemistry as it can predict species in the interphases that might be hidden or changed due to poor empirical characterization. The drawback of first-principle models is that they cannot properly handle cycling of intercalation electrodes as the consideration of the bulk structure is necessary which cannot be represented with a traditional surface thermodynamics approach.[149,150] MD and DFT consider clean surfaces and influences of close subsurface layers, so they do not consider structural changes inside the electrodes during cycling.

A step closer to modeling complete cell behavior are electrochemical engineered models that are often also known as physicochemical models. Within this class, surface and molecule processes are modeled in a phenomenological manner but the particle and electrode domain are described mechanistically.
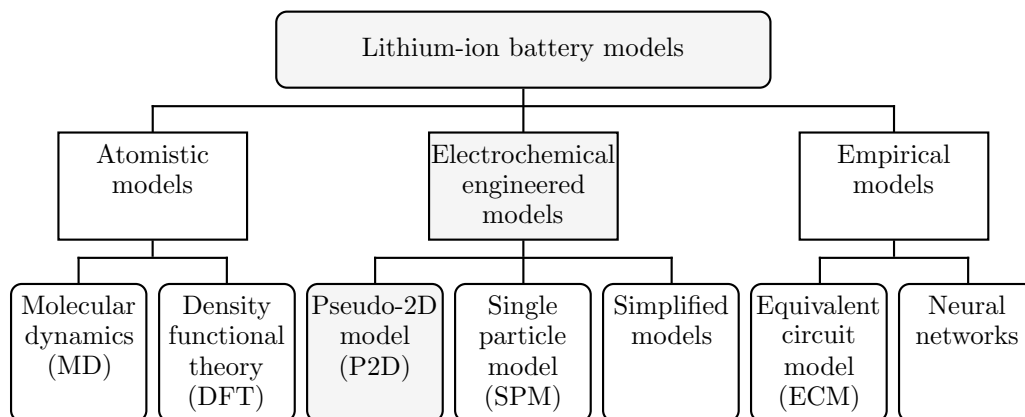
Figure 3.3: Categories of models used in lithium-ion battery simulations.[143] From left to right models are of a increasingly phenomenological manner. Uncolored models are outside the focus of this work and the P2D model is further used.

Based on electrochemical kinetics and transport equations they can simulate cell characteristics and intercalation as well as side reactions.[142,143,145]

Representatives of electrochemistry-based models are the pseudo-2D (P2D) model developed by Newman and co-workers[151–153] and the single particle model (SPM) which was first introduced for lithium-ion batteries by Zhang et al.[154] The often proved accuracy and agreement with experimental data of the P2D model originate from its basic implementation of porous electrode theory as well as concentrated solution theory.[151,155] Up to today, the P2D model represents the most precise and – though computationally costly – most popular model in lithium-ion battery research.[151] The SPM represents a simplification of the P2D model in order to decrease computational time. As the spatial representation of the liquid phase are neglected and transport phenomena are just considered in one single representative particle, the SPM lacks the accuracy of the P2D model especially in high-current scenarios but still shows good agreement with experimental data.[143,154,156]

Empirical models are based on implementing behavioral trends from past experiments and predicting future states such as state-of-charge (SOC) and state-of-health (SOH) from there. Models of that category are equivalent circuit model (ECM) and neural network models.[143,157] As they are relatively simple to implement and computationally fast, empirical models are found in literature quite often.[157–165] However, their application is limited as they can only describe a previously seen and implemented behavior, so an adaption to another cell or even chemistry needs a completely new database.[142,143]

The target in this work is to understand and describe the physical processes resulting in a certain electrode or cell behavior. Due to this intention for using the model, further remarks on atomistic modeling as well as empirical modeling are outside the focus of this manuscript. The preferred and subsequently used model for that purpose – the P2D model – is introduced in Section 3.2.

3.2 Physicochemical modeling based on P2D model

The Newman model – named after Prof. John S. Newman from University of California, Berkeley – is based on the theory of porous electrodes and the theory of concentrated solutions. By implementing a radial dimension along the 1D axis, the model is of a P2D class. As Newman's model has been

extensively introduced and discussed in literature, the following section gives a quick introduction of the main equations. For a thorough introduction the reader is referred to the book *Electrochemical systems* by John S. Newman and Karen E. Thomas-Alyea.[151]

3.2.1 Representation of the porous electrode structure

Newman's model is a 1D model extended with a second pseudo dimension in the porous electrode phase to account for ion concentration in the active material. Figure 3.4 shows a cross-section of a lithium-ion cell stack which is the basis for the consideration of a porous electrode structure in the model.
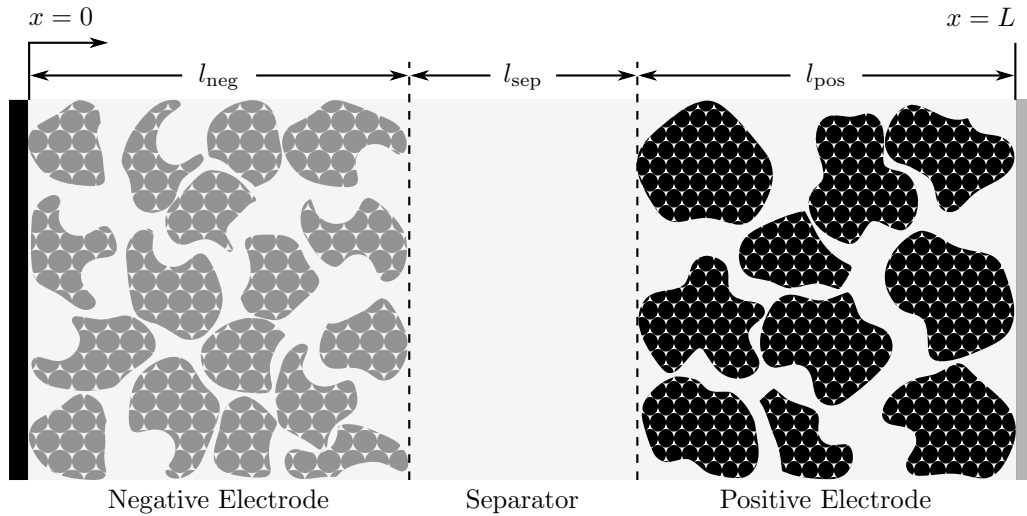
Figure 3.4: Exemplary cross-section representation of the porous electrode structure in a lithium-ion cell stack.

The reduction of a 3D lithium-ion cell to one dimension originates from the consideration of a thought perpendicular line through the electrodes and the separator along an x-axis. The origin of this line is in the current collector of the negative electrode. With this presumption, it is possible to determine the potential and the concentration of the electrolyte as well as the potential and the concentration of the active materials in every point along that line.

Therefore, the porous phase is considered a mixture of active material particles and electrolyte in every point. This assumption is based on the conception that all particles are very small, uniformly radially symmetric and surrounded by electrolyte and that the extent in y- and z-direction is infinite. With that homogenization, the approximation that a particle's surface as well as the electrolyte touches the axis in every point seems valid which leads to a superposition of both phases at every point.

In reality, electrode structures consist of particles with a diameter that is just a fraction of the electrode thickness. Graphite particles that are used for anodes often have a diameter between 2 and 40 μm.[45,166,167]

Newman's model is composed of two phases (liquid and solid) in three domains (negative electrode / separator / positive electrode). With the separator treated as liquid phase, electron transport is only possible in the solid phase of the electrode domains. As the origin of the x-axis is in the negative current collector, the length (l_{neg}, l_{sep} and l_{pos}) along the axis describes the thickness of the domains.

The porosity of the electrodes is described with $\varepsilon_{l,\mathrm{pos/neg}}$ and the volume fraction of the active material with $\varepsilon_{s,\mathrm{pos/neg}}$. Since the porous separator contains no active material, it is fully characterized by $\varepsilon_{l,\mathrm{sep}}$. Tortuosity is considered in all domains via effective parameter scaling of the transport parameters.

The description of the three domains results in four interdependent variables

$$c_l(x,t) \text{ in mol/m}^3, \quad \text{lithium-ion concentration in the electrolyte}$$
$$c_s(r,x,t) \text{ in mol/m}^3, \quad \text{lithium-ion concentration in the active material}$$
$$\Phi_l(x,t) \text{ in V}, \quad \text{electrolyte potential}$$
$$\Phi_s(x,t) \text{ in V}, \quad \text{electrode potential in the active material}$$

Solid-phase variables are obsolete in the separator domain, since neither electron flux nor intercalation in active material is possible, and are only solved in the electrode domains.

In the case of lithium-ion cell modeling, the spatial and temporal progression of the cations – the lithium-ions – is of interest. Due to the condition of electroneutrality, the local concentration of anions is implicitly given by considering just the cations when solving the system of equations.

At the end of this section, a schematic depiction of the P2D model in Figure 3.5 shows the dimensions in which lithium-ions and electrons are considered during charge and discharge. Thereby, the figure can help to comprehend the following model equations.

3.2.2 Mass balance in the liquid phase

A general representation of the mass balance in the electrolyte is given by

$$\frac{\partial c_l}{\partial t} = -\nabla \boldsymbol{N}_l + R_l \tag{3.1}$$

where the change in the lithium-ion concentration in the liquid phase c_l is depending on the divergence (with $\nabla \coloneqq \frac{\mathrm{d}}{\mathrm{d}x}$) of the ionic flux density $\boldsymbol{N}_l$ and a certain reaction term R_l that will be explained in Equation 3.17.

The ionic flux density $\boldsymbol{N}_l$ has the unit $\mathrm{mol/m}^2\,\mathrm{s}$ and is defined by a diffusion and a migration component as convection can be neglected inside a cell

$$\boldsymbol{N}_l = \boldsymbol{N}_{l,\mathrm{diff}} + \boldsymbol{N}_{l,\mathrm{mig}} \tag{3.2}$$

Diffusion is caused by a concentration gradient and follows Fick's law

$$\boldsymbol{N}_{l,\mathrm{diff}} = -D_l \nabla c_l \tag{3.3}$$

The electric field that drives migration is considered for cations by the transport number t_+ which gives the share of cations to the total current density ($\boldsymbol{i}_l$)

$$\boldsymbol{N}_{l,\mathrm{mig}} = \frac{\boldsymbol{i}_l t_+}{F} \tag{3.4}$$

with F representing Faraday's constant. Summarized, Equation 3.2 can be written as

$$\boldsymbol{N}_l = -D_l \nabla c_l + \frac{\boldsymbol{i}_l t_+}{F} \tag{3.5}$$

When using transport parameters as the diffusion coefficient D_l, the influence of the tortuosity τ has to be acknowledged for constrictions given by the blocking of the direct path in a porous electrode. The probably best-known correction for the increase of the transport path was introduced by Bruggeman, but is only valid for uniform spherical particles and a layer porosity of about $50\,\%$.[168] The Bruggeman correction scales all transport parameters with a factor of $\varepsilon_l^{1.5}$.

Another possible correction is using MacMullin's number N_M.[169] Here, all transport parameters are divided by N_M to get effective values that account for the tortuosity in the 1D modeling approach. N_M is given by the tortuosity and porosity of the porous medium, dependent on geometrical empiric constants m and n

$$N_M = \frac{\tau^n}{\varepsilon^m} \tag{3.6}$$

In porous materials of lithium-ion cells MacMullin numbers of 4 to 10 are common.[170] The big advantage of using MacMullin's number is, that it can be measured e.g. with EIS by comparing the electrical resistance of an electrolyte filled probe with the resistance of just the electrolyte.

For the example of the diffusion constant D_l the correction with N_M can be written as

$$D_{l,\text{eff}} = \frac{1}{N_M} D_l \tag{3.7}$$

In the same manner the effective electrolyte conductivity κ_{eff} is given by

$$\kappa_{\text{eff}} = \frac{1}{N_M} \kappa \tag{3.8}$$

According to the porosity of the entire domain volume, the temporal variation of the concentration from Equation 3.1 has to be scaled with ε_l. So, the mass balance in the liquid phase of the electrode domains is given by

$$\varepsilon_l \frac{\partial c_l}{\partial t} = \nabla \left(D_{l,\text{eff}} \nabla c_l - \frac{\boldsymbol{i}_l t_+}{F} \right) + R_l \qquad \text{in electrode domains} \tag{3.9}$$

Since the separator domain is solenoidal, the temporal variation of the concentration is just determined by the ionic flux density ($R_l = 0$) and is, therefore, given by

$$\varepsilon_l \frac{\partial c_l}{\partial t} = \nabla \left(D_{l,\text{eff}} \nabla c_l - \frac{\boldsymbol{i}_l t_+}{F} \right) \qquad \text{in separator domain} \tag{3.10}$$

3.2.3 Mass transport in the solid phase

Since the mass transport in the active material is considered in the pseudo dimension r, certain differences to the approach in the liquid phase appear. As mentioned before, the assumption of the Newman model is that every point along the x-axis in the electrode domains has a second dimension

r to represent diffusion in the particles which are assumed radially symmetric. Therefore, diffusion in or from a particle is described by Fick's law

$$\boldsymbol{N}_s = -D_s \nabla c_s \tag{3.11}$$

Analog to considerations in the liquid phase, a temporal alteration of the particle's concentration is due to flux changes, since no reaction takes place inside the particles

$$\frac{\partial c_s}{\partial t} = -\nabla \boldsymbol{N}_s \tag{3.12}$$

With transformation to spherical coordinates, Equations 3.11 and 3.12 give a description for the pseudo dimension at every point along the x-axis

$$\frac{\partial c_s}{\partial t} = -\nabla \boldsymbol{N}_s = D_s \left(\frac{\partial^2 c_s}{\partial r^2} + \frac{2}{r} \frac{\partial c_s}{\partial r} \right) \tag{3.13}$$

Two conditions have to be added to assume symmetrical particles

$$\left. \frac{\partial c_s}{\partial r} \right|_{r=0} = 0 \tag{3.14}$$

as well as to preserve the flux on the particles' surface $r = r_p$

$$-D_s \left. \frac{\partial c_s}{\partial r} \right|_{r=r_p} = j_n \tag{3.15}$$

The pore-wall flux density j_n in mol/m^2 s defines the amount of ions that pass through the particle surface into or out of the particle during a certain time. The subscript n represents the geometrical consideration that the flux is perpendicular to the interface between electrode and electrolyte. Since x-dimension and pseudo dimension are geometrically decoupled, the specific surface a_s (in 1/m) couples the x- and r-dimension physically. The specific surface is the ratio between the particle's surface and its volume (scaled with the volume fraction ε_s)

$$a_s = \frac{A_{\text{particle}}}{V_{\text{particle}}} = \frac{4\pi r_p^2}{\frac{4}{3}\pi \frac{r_p^3}{\varepsilon_s}} = 3\frac{\varepsilon_s}{r_p} \tag{3.16}$$

Basically, the specific surface is a conversion factor to reduce the complex three dimensional electrode structure to a one dimensional problem by providing an interface between both dimensions. The aforementioned reaction term R_l results in

$$R_l = a_s j_n \tag{3.17}$$

3.2.4 Charge balance in a cell

As most of the electrolytes in commercial lithium-ion cells are binary electrolytes (dissolve in univalent anion and cation), the current density in the liquid phase $\boldsymbol{i}_l$ dependent on its potential Φ_l and electrolyte

concentration calculates as

$$\boldsymbol{i}_l = -\kappa_{\text{eff}}\nabla\Phi_l + \frac{2\kappa_{\text{eff}}RT}{F}\left(1 + \frac{\partial \ln f_\pm}{\partial \ln c_l}\right)(1 - t_+)\nabla \ln c_l \tag{3.18}$$

with κ_{eff} being the effective value of the electrolyte conductivity and $\frac{\partial \ln f_\pm}{\partial \ln c_l}$ being a correction for the mean activity coefficient $f_\pm$ to account for interactions between anions and cations.

Whereas the liquid phase is described by a modified Ohm's law, the solid phase can be described by a classical Ohm's law in differential notation

$$\boldsymbol{i}_s = -\sigma_{\text{eff}}\nabla\Phi_s \tag{3.19}$$

with Φ_s as the solid phase potential and the solid phase conductivity σ_{eff}.

The overall current density I is defined by the current densities of the solid and the liquid phase

$$\boldsymbol{I} = \boldsymbol{i}_s + \boldsymbol{i}_l \tag{3.20}$$

Introducing Equation 3.18 into the solenoidality definition of the separator domain gives

$$\nabla\boldsymbol{i}_l = \nabla\left(-\kappa_{\text{eff}}\nabla\Phi_l + \frac{2\kappa_{\text{eff}}RT}{F}\left(1 + \frac{\partial \ln f_\pm}{\partial \ln c_l}\right)(1 - t_+)\nabla \ln c_l\right) = 0 \tag{3.21}$$

The charge balance in the electrode domains has to consider the equilibrium of incoming/outgoing charges (cations) in the electrolyte and incoming/outgoing charges (electrons) in the solid active material

$$-\nabla\boldsymbol{i}_l = \nabla\boldsymbol{i}_s \tag{3.22}$$

Both terms have to equal the concentration change of charge carriers at the interface of the solid and liquid phase due to production or consumption of charges by electrochemical reactions

$$-\frac{s_i}{nF}\nabla\boldsymbol{i}_l = a_s j_n \tag{3.23}$$

The reaction on the particles' surface resembles the following scheme

$$\text{Li}^+ + \Theta_s + e^- \rightleftharpoons \text{Li}\Theta_s \tag{3.24}$$

with the host lattice Θ_s and $\text{Li}\Theta_s$ as an intercalated lithium-ion. From Equation 3.24 the number of electrons n can be derived as 1 and the stoichiometric coefficient of lithium-ions s_{Li^+} as -1.

Therefore, the charge balance of the liquid phase – in the electrode domains in contrast to the separator domain – is not 0, but given by

$$\nabla\left(-\kappa_{\text{eff}}\nabla\Phi_l + \frac{2\kappa_{\text{eff}}RT}{F}\left(1 + \frac{\partial \ln f_\pm}{\partial \ln c_l}\right)(1 - t_+)\nabla \ln c_l\right) = -\nabla\boldsymbol{i}_s \tag{3.25}$$

3.2.5 Coupling the solid and liquid phase

Reaction 3.24 can be described mathematically by a Butler-Volmer equation. The driving force is the overpotential η defined by the difference of the electrode potential $\Phi_s - \Phi_l$ and the thermodynamic equilibrium potential E_{Eq}

$$\eta = \Phi_s - \Phi_l - E_{\mathrm{Eq}} \tag{3.26}$$

Introduced in a Butler-Volmer equation, the charge-transfer current density i_n is calculated by

$$i_n = i_0 \left(e^{\frac{\alpha_a F}{RT} \eta} - e^{-\frac{\alpha_c F}{RT} \eta} \right) \tag{3.27}$$

The subscript n again symbolizes the perpendicular consideration through the interface, so that the charge-transfer current density can neither be assigned to the solid nor the liquid phase. The corresponding exchange current density i_0 is defined by

$$i_0 = F k_c^{\alpha_a} k_a^{\alpha_c} \left(c_{s,\mathrm{max}} - c_s|_{r=r_p} \right)^{\alpha_a} \left(c_s|_{r=r_p} \right)^{\alpha_c} \left(\frac{c_l}{1\,\mathrm{mol/m^3}} \right)^{\alpha_a} \tag{3.28}$$

The maximum possible concentration of lithium-ions in the active material is given by $c_{s,\mathrm{max}}$ and c_l defines the concentration in the electrolyte. k_a and k_c describe reaction rates in m/s and α_a and α_c unit free charge-transfer coefficients. Subscripts a and c signify anodic and cathodic direction, respectively. The scaling of the last factor with $1\,\mathrm{mol/m^3}$ is for simplifying the units of k_i which get reduced to m/s in the case of $\alpha_a = \alpha_c = 0.5$. This case represents a one-electron transfer process with the same rate determining step in the anodic and cathodic direction[171].

The charge-transfer current density i_n correlates to the pore-wall flux density j_n via Faraday's law

$$j_n = \frac{i_n}{F} \tag{3.29}$$

Following the general definition, an anodic charge-transfer current density is considered positive i.e. a lithium-ion going from the solid to the liquid phase causes a positive current density i_n as well as a positive pore-wall flux density j_n.

The aforementioned reaction term R_l in $\mathrm{mol/m^3\,s}$ determines how many lithium-ions appear on the particle surface (deintercalation from host lattice) or disappear (intercalation into host lattice) in a certain volume per second. The mass balance in r-dimension and the mass as well as the charge balance in x-dimension are coupled by this term.

3.2.6 Boundary conditions

Two conditions for the model (Equations 3.14 and 3.15) have already been introduced. Further boundary conditions for being able to solve the partial differential equations numerically are introduced here.

The ionic flux $\boldsymbol{N}_l$ has to be terminated at the boundaries of the model i.e. the interface between electrode and current collector

$$\nabla c_l\big|_{x=0 \ \& \ x=L} = 0 \tag{3.30}$$

with $L = l_{\text{neg}} + l_{\text{sep}} + l_{\text{pos}}$. Since current collectors only transport electronic currents, no ionic current density ($\boldsymbol{i}_l = 0$) and reaction occurs which leads to

$$\nabla\Phi_l\big|_{x=0 \ \& \ x=L} = 0 \tag{3.31}$$

Due to $\boldsymbol{I} = \boldsymbol{i}_l + \boldsymbol{i}_s$ and $\boldsymbol{i}_l = \boldsymbol{0}$ in the current collectors, the solid phase potential is given by

$$\nabla\Phi_s\big|_{x=0 \ \& \ x=L} = -\frac{I}{\sigma_{\text{eff}}} \tag{3.32}$$

In contrast, the separator domain only supports ionic currents

$$\nabla\Phi_s\big|_{x=l_{\text{neg}} \ \& \ x=l_{\text{neg}}+l_{\text{sep}}} = 0 \tag{3.33}$$

Finished with the boundary conditions, all necessary assumptions and equations for understanding and implementing Newman's model have been introduced.
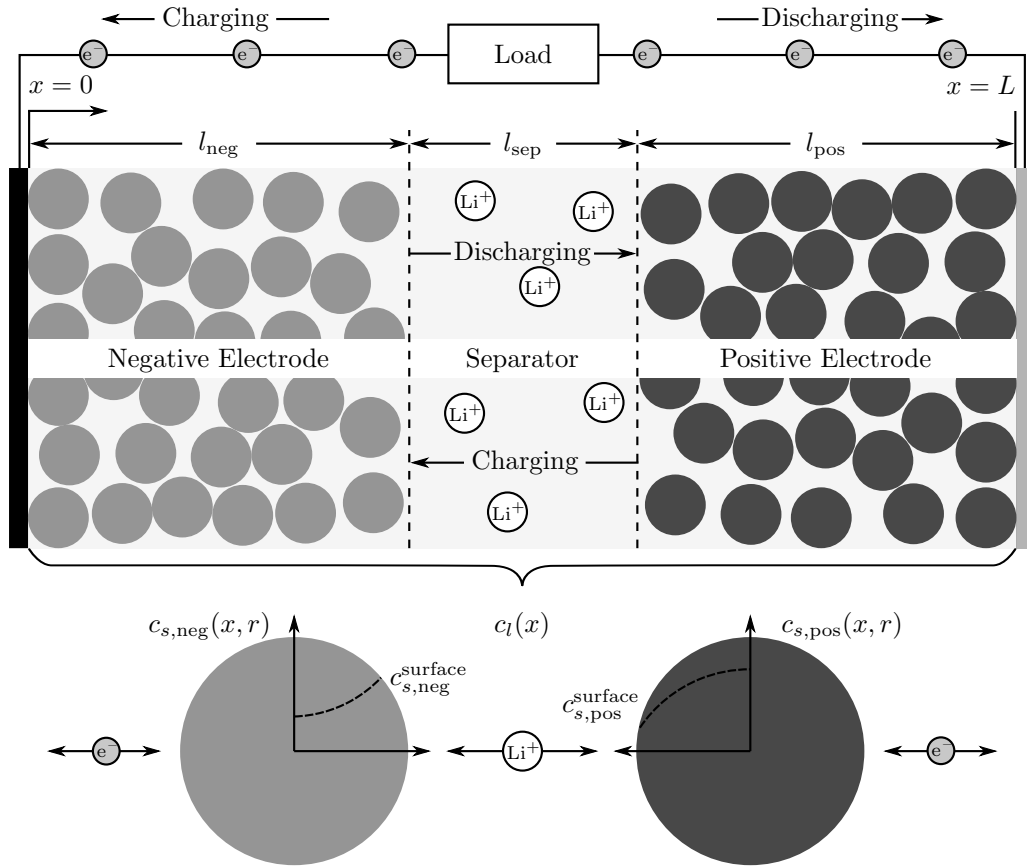
Figure 3.5: An overview of the P2D model with the respective dependent variables and where they are solved is shown above.[172] During charging and discharging lithium-ion concentration in the liquid phase is only solved in x-direction along the length of the cell whereas the solid concentration also considers a radial distribution in the particles.

3.3 A SEI Modeling Approach Distinguishing between Capacity and Power Fade

In this paper we introduced a new approach for modeling aging behavior that distinguishes between electronic (σ_{SEI}) and ionic (κ_{SEI}) conductivity of the SEI. To analyze the behavior of the most important aging mechanisms and their impact on capacity fade, we implemented a P2D physicochemical model for a common NCM/graphite cell using COMSOL® Multiphysics 5.2a.

The implementation of SEI growth in the model distinguishes between the transport of two species through the SEI – lithium-ions on the one hand and electrons on the other hand. This is in accordance with the assumption that the SEI possesses two ideal properties (as introduced in Chapter 1) – a maximum conductivity for lithium-ions and an insulating conductivity for electrons.[2,4]

We are aware that literature[167,173,174] still debates whether new SEI is formed at the SEI/electrolyte or the graphite/SEI interface. With our approach, we assume that new SEI is formed at the SEI/electrolyte interface. In the case of an SEI formation at the graphite/SEI interface solvent particles would need to be the second species migrating through the SEI besides lithium-ions. As our P2D model treats the SEI as an interface phenomenon influencing charge-transfer, both cases would lead to the same cell behavior, so we stick to electron migration through the SEI for SEI formation. This new approach results in a different ohmic drop (iR) for the driving overpotential of the main intercalation reaction at the negative electrode η_{neg} and the SEI forming side reaction η_{SEI}. By this approach we can also differentiate between capacity and power fade which is inevitably connected in a single conductivity approach.

With experimental aging data from a paper published by Ecker et al.[175] in 2014, we were able to determine an exchange current density for SEI formation depending on temperature. As the model is able to simulate calendar and cyclic aging, we not only could define the growth due to non-ideal insulation properties but additionally, an SEI re-formation after cracking due to graphite expansion during intercalation of lithium-ions.[82,176]

We assume that the known aging behavior of a lithium-ion battery cannot be represented completely by a mere implementation of SEI growth. In literature, models with SEI growth as their only capacity fade mechanism do not show the typical non-linear aging behavior – i.e. the sudden decrease – in usable capacity after several hundred cycles.[36,167,174,176,177] In these models, this non-linear aging behavior can be emulated by a high power fade, though, which shortens charging and discharging due to high overpotentials that decrease the usable capacity.[176,178] Measurements in literature ascribe this non-linear aging behavior to lithium-plating[179,180] as well as to degradation mechanisms on the cathode.[131,181,182] For the here introduced model we chose to implement a cathode dissolution reaction as the responsible mechanism for the non-linear aging behavior. As we lack any information on that topic from the chosen experimental data, including a mechanism on the positive electrode seems sensible in regard of the possible interactions between the two mechanisms (SEI growth and lithium-plating) at the negative electrode.

When modeling the thickness of the SEI throughout the electrode, we observe (refer to Figure 3.6) a non-uniform growth that is distinctly higher close to the separator (~600 nm) than near the current collector (~250 nm). This effect can be assigned to an inhomogeneous current density distribution through the electrolyte during cycling.
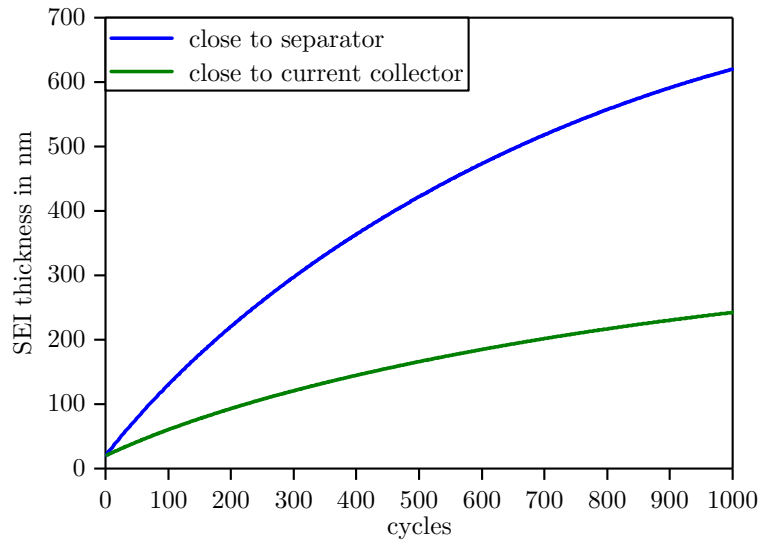
Figure 3.6: Comparison of the modeled SEI thickness close to the separator and close to the current collector over 1000 cycles.

Author contribution   The new SEI modeling approach was developed and derived from my studies and literature research of the formation process as introduced in the previous chapters. The model development was carried out in collaboration with Jonas Keil and Alexander Frank helped with processing the simulation data.

A SEI Modeling Approach Distinguishing between Capacity and Power Fade

Frank M. Kindermann, Jonas Keil, Alexander Frank, Andreas Jossen

Permanent weblink:
http://dx.doi.org/10.1149/2.0321712jes

A SEI Modeling Approach Distinguishing between Capacity and Power Fade

Frank M. Kindermann,*,z Jonas Keil,* Alexander Frank, and Andreas Jossen

Technical University of Munich (TUM), Institute for Electrical Energy Storage Technology, Munich, Germany

In this paper we introduce a pseudo two-dimensional (P2D) model for a common lithium-nickel-cobalt-manganese-oxide versus graphite (NCM/graphite) cell with solid electrolyte interphase (SEI) growth as the dominating capacity fade mechanism on the anode and active material dissolution as the main aging mechanism on the cathode. The SEI implementation considers a growth due to non-ideal insulation properties during calendar as well as cyclic aging and a re-formation after cyclic cracking of the layer during graphite expansion. Additionally, our approach distinguishes between an electronic (σ_{SEI}) and an ionic (κ_{SEI}) conductivity of the SEI. This approach introduces the possibility to adapt the model to capacity as well as power fade. Simulation data show good agreement with an experimental aging study for NCM/graphite cells at different temperatures introduced in literature.

Lithium-ion batteries are one of the most promising candidates for energy storage in future stationary storage systems and electric vehicles.[1–3] Enormous research efforts have been conducted to get a thorough understanding of the system "lithium-ion cell" and to further develop it for higher energy and power density, higher safety standards as well as longer cycle life.[4]

The aging behavior of lithium-ion batteries has been a focus issue of battery research since the introduction of lithium-ion cells by Sony in 1991.[5] Reviews by Agubra et al.,[6,7] Arora et al.,[8] Aurbach et al.,[9,10] Birkl et al.,[11] Broussely et al.,[12] Verma et al.[13] and Vetter et al.[14] are just a few examples of the extensive literature regarding aging behavior. Commonly accepted and experimentally verified aging phenomena as mentioned in the previously cited literature are electrolyte decomposition leading to solid electrolyte interphase (SEI) and cathode electrolyte interphase (CEI) growth, solvent co-intercalation, gas evolution with subsequent cracking of particles, a decrease of accessible surface area and porosity due to SEI growth, contact loss of active material particles due to volume changes during cycling, binder decomposition, current collector corrosion, metallic lithium plating and transition-metal dissolution from the cathode.

The listed aging mechanisms can be assigned to three different categories that are a loss of lithium-ions (LLI), an impedance increase and a loss of active material (LAM).[12,15–18] The LLI is synonymous to a decrease in the amount of cyclable lithium-ions as they are trapped in a passivating film on either of the electrodes or in plated metallic lithium. Due to the growth of the passivating layers and/or the formation of rock-salt in the cathode (residue of the cathode active material after transition-metal dissolution), kinetic transport of lithium-ions through those inactive areas is limited and results in an impedance rise. An LAM can be caused by the dissolution of transition-metal-ions from the cathode bulk material, changes in the electrode composition and/or changes in crystal structure of the active material which all diminish the amount of host structure for lithium-ion intercalation. Also mechanical strain during de-/intercalation can contribute to LAM as particles from both electrodes can crack and get electronically separated from the bulk material.

For investigating or describing the behavior of lithium-ion cells, different model categories can be implemented and those can be classified into first-principle, electrochemical engineered and empirical models.[19,20]

Atomistic models based molecular dynamics (MD)[21,22] and density functional theory (DFT)[23–25] try to recreate molecular behavior on an atomic scale. As they use fundamental physics-based approaches for atom-atom interactions, these models are also called first-principle models.[21] This category of models becomes of greater importance in future research efforts for better understanding interfacial chemistry as it can predict species in the interphases that might be hidden or changed due to poor empirical characterization. The drawback of first-principle models is that they cannot properly handle cycling of intercalation electrodes as the consideration of the bulk structure is necessary which cannot be represented with a traditional surface thermodynamics approach.[26,27] MD and DFT consider clean surfaces and influences of close subsurface layers, so they do not consider structural changes in the electrodes during cycling.

A step closer to modeling complete cell behavior are electrochemical engineered models that are often also known as physicochemical models. Within this class, surface and molecule processes are modeled in a phenomenological manner but the particle and electrode domain are described mechanistically. Based on electrochemical kinetics and transport equations they can simulate cell characteristics and intercalation as well as side reactions.[19,20] The best-known electrochemistry-based models are the pseudo two-dimensional (P2D) model developed by Newman and co-workers[28–30] and the single particle model (SPM) first introduced by Zhang et al.[31] The often proved accuracy and agreement with experimental data of the P2D model originate from its basic implementation of porous electrode theory as well as concentrated solution theory.[28,32] Up to today, the P2D model represents the most precise and – though computationally costly – most popular model in lithium-ion battery research.[28] The SPM represents a simplification of the P2D model in order to decrease computational time. As the spatial representation of the liquid phase are neglected and transport phenomena are just considered in one single representative particle, the SPM lacks the accuracy of the P2D model but still shows good agreement with experimental data.[20,31,33]

Empirical models are based on implementing behavioral trends from past experiments and predicting future states such as state-of-charge (SOC) and state-of-health (SOH) from there. The best known models of that category are equivalent circuit models and neural network models.[20,34] As they are relatively simple to implement and computationally fast, empirical models are frequently found in literature.[34–42] However, their application is limited as they can only describe a previously seen and implemented behavior, so an adaption to another cell or even chemistry needs a completely new database.[19,20]

Previous literature described several degradation mechanisms on anode as well as cathode in a P2D model. Ashwin et al.[43,44] investigated the porosity change in the negative electrode due to SEI growth under different cycle and temperature conditions. Fu et al.[45] ascribed capacity fade to SEI growth as well as active material degradation and found an extra deposit layer on the anode near the separator. Lawder et al.[46] studied the influence of different driving cycle profiles on the capacity fade of electric vehicle batteries and ascribed the total capacity fade to SEI growth. The effects of gas evolution due to SEI growth were modeled by Rashid et al.[47] On the cathode side, Cai et al.[48] implemented an SOC independent manganese disproportionation which

*Electrochemical Society Student Member.
zE-mail: f.kindermann@tum.de

increased the cathodic resistance and lead to a change both in porosity as well as particle radius. A combination of SEI growth and cathode dissolution in a lithium-cobalt-oxide (LCO) cell was shown by Lam et al.[49] and optimal discharge parameters were derived. Another very extensive model that included manganese dissolution from a lithium-manganese-oxide cathode and the effects of manganese-ions incorporated into the anodic SEI was presented by Lin et al.[50]

In this paper we introduce a P2D model for a common NCM/graphite cell with SEI growth as the dominating capacity fade mechanism on the graphite anode and active material dissolution as the main aging mechanism on the cathode. The SEI implementation considers a growth due to imperfections in its insulating properties as well as new SEI formation due to cracking of the layer during graphite expansion when cycling the cell. The novelty of our approach is that we include two separate conductivities within the SEI for lithium-ions (κ_{SEI}) and electrons (σ_{SEI}) leading to distinct overpotentials driving the main and side reaction. Simulation data is compared to experimental studies on NCM/graphite cells performed by Ecker et al.[51]

Model Development

To analyze the behavior of the most important aging mechanisms and their impact on capacity fade, we implemented a P2D physicochemical model for a common NCM/graphite cell using COMSOL Multiphysics 5.2a. As the basic equations of the P2D model have been extensively shown in literature,[28–30] a brief overview of the model and all used parameters (see Table AI) are given in the Appendix. The basic assumptions of the implemented aging mechanisms in the presented model are introduced and discussed subsequently.

Implementation of SEI growth.—For the implementation of SEI growth we introduce a new approach that distinguishes between the transport of two species through the SEI – lithium-ions on the one hand and electrons on the other hand (refer to Figure 1a). This is in accordance with the assumption that the SEI possesses two ideal properties – a maximum conductivity for lithium-ions and an insulating conductivity for electrons.[13,52] We are aware that literature[53–55] still debates whether new SEI is formed at the SEI/electrolyte or the graphite/SEI interface. With our approach, we assume that new SEI is formed at the SEI/electrolyte interface. In the case of an SEI formation at the graphite/SEI interface solvent particles would need to be the second species migrating through the SEI besides lithium-ions. As our P2D model treats the SEI as an interface phenomenon influencing charge-transfer, both cases would lead to the same cell behavior, so we stick to electron migration through the SEI for SEI formation.

Our new approach results in a different ohmic drop (iR) for the driving overpotential of the main intercalation reaction at the negative electrode η_{neg} and the SEI forming side reaction η_{SEI}.

$$\eta_i = \Phi_s - \Phi_l - E_{Eq,i} - i_i \cdot R_i \qquad [1]$$

Both resistances R_{neg} and R_{SEI} are dependent on the SEI's initial thickness $\delta_{0,SEI}$, the thickness increase $\Delta\delta_{SEI}$ and the respective conductivity. The initial thickness is assumed to be 20 nm which is considered a fully formed SEI[56] and the thickness increase is due to the non-ideal insulating properties as well as an SEI re-formation after cracking.

$$R_{neg} = \frac{\delta_{0,SEI} + \Delta\delta_{SEI}}{\kappa_{SEI}} \qquad [2]$$

$$R_{SEI} = \frac{\delta_{0,SEI} + \Delta\delta_{SEI}}{\sigma_{SEI}} \qquad [3]$$

As no measurements of the SEI's electronic conductivity σ_{SEI} are known,[56] we assume σ_{SEI} to be 10^{-8} S m^{-1} which is considered an insulating behavior.[57] In contrast, the ionic conductivity κ_{SEI} is presumed to be 10^{-2} S m^{-1} which is approximately the conductivity of a liquid lithium-ion battery electrolyte.[57]

With the introduced overpotentials we implemented a growth due to imperfections in the SEI's insulating properties by Butler-Volmer
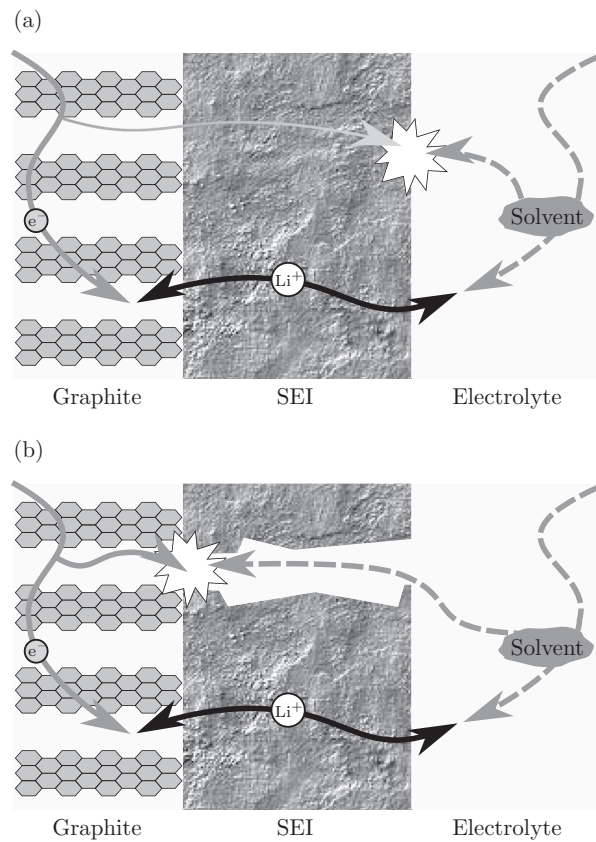

Figure 1. (a) SEI growth at SEI/electrolyte interface by electron flux through the interphase. Lithium-ion transport for (de-)intercalation reaction has a different conductivity than the electron transport. (b) SEI growth in cracks without hindrance of interphase.

kinetics with an anodic charge-transfer coefficient $\alpha_{a,SEI} = 0.05$ and a cathodic charge-transfer coefficient $\alpha_{c,SEI} = 0.95$. This implementation is close to the often used cathodic Tafel expression[8,15] but considers also dissolution reactions during cycling.[58]

$$i_{SEI,n} = i_{0,SEI} \cdot \left[\exp\left(\frac{\alpha_{a,SEI} \cdot F \cdot \eta_{SEI}}{RT} \right) - \exp\left(\frac{-\alpha_{c,SEI} \cdot F \cdot \eta_{SEI}}{RT} \right) \right] \qquad [4]$$

The index n in $i_{SEI,n}$ symbolizes LiF and Li$_2$CO$_3$ as we included the two most important SEI products in the model.[59,60] F, R and T represent Faraday's constant, the universal gas constant and the absolute temperature, respectively. Specific values for $i_{0,SEI}$ will be given in the Results and discussion section by Equation 11.

Additionally, we implemented an SEI re-formation after cracking due to graphite expansion during intercalation of lithium-ions.[61,62] As we only assume a new formation without dissolution by cracking, the anodic part in the Butler-Volmer equation is omitted and the overpotential η_{crack} considers no iR-drop.

$$\eta_{crack} = \Phi_s - \Phi_l - E_{Eq,SEI} \qquad [5]$$

The current density computation considers a cracking function dependent on intercalation degree x that is depicted in Figure 2 which is the gradient of a graphite expansion curve as previously introduced by Laresgoiti et al.[62] Furthermore, we included an empirical factor $\frac{i_{neg}}{i_{C/100}}$ to scale the cracking for utilization at different intercalation current densities.

$$i_{crack} = -i_{0,SEI} \cdot \left(\frac{i_{neg}}{i_{C/100}} \right) \cdot f_{crack}(x) \cdot \exp\left(\frac{-F \cdot \eta_{crack}}{RT} \right) \qquad [6]$$
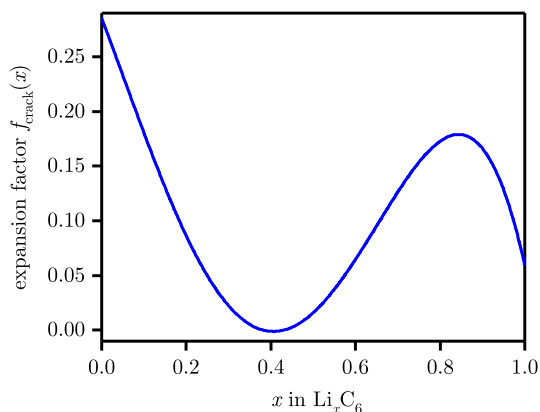
Figure 2. Function $f_{crack}(x)$ of the expansion gradient over lithiation degree x to scale the amount of SEI cracking during different stages of intercalation.

For simplicity, we assume that only Li_2CO_3 is formed in the cracks. The overall increase in SEI thickness $\Delta\delta_{SEI}$ after integrating the respective current densities is calculated with the molar masses M_i and densities ρ_i by

$$\Delta\delta_{SEI} = \frac{(Q_{crack} + Q_{Li_2CO_3}) \cdot M_{Li_2CO_3}}{\rho_{Li_2CO_3} \cdot F} + \frac{Q_{LiF} \cdot M_{LiF}}{\rho_{LiF} \cdot F} \quad [7]$$

The lithium-ions consumed in the three SEI forming charge quantities are subtracted from the total amount of cyclable lithium-ions and represent the LLI in the model.

We assume that the known aging behavior of a lithium-ion battery cannot be represented completely by a mere implementation of SEI growth. In literature, models with SEI growth as their only capacity fade mechanism do not show the typical non-linear aging behavior – i.e. the sudden decrease – in usable capacity after several hundred cycles.[53,55,59,61,63] In these models, this non-linear aging behavior can be emulated by a high power fade, though, which shortens charging and discharging due to high overpotentials that decrease the usable capacity.[43,61] Measurements in literature ascribe this non-linear aging behavior to lithium plating[64,65] as well as to degradation mechanisms on the cathode.[5,48,50] For the here introduced model we chose to implement a cathode dissolution reaction as the responsible mechanism for the non-linear aging behavior. As we lack any information on that topic from the chosen experimental data, including a mechanism on the positive electrode seems sensible in regard of the possible interactions between the two mechanisms (SEI growth and lithium plating) at the negative electrode.

We are aware that dissolved transition-metal ions from the cathode have been reported to be incorporated in the anodic SEI and have altering effects on its properties.[66-68] Including those effects will be part of future investigations, as they are not crucial for the general improvement of the introduced SEI model representation by two conductivities.

Cathode dissolution reaction.—The implemented dissolution reaction, is reducing the solid phase volume fraction $\varepsilon_{s,pos}$ depending on the cathode's intercalation degree. Hence, the reduction of $\varepsilon_{s,pos}$ corresponds to the LAM in our model. Acid attack by HF is one of the dominating causes for active material dissolution at the cathode[50,69,70] and is implemented as an irreversible kinetics expression in the positive electrode domain. As HF evolution is promoted at potentials above $4.0 V$,[69] this potential is used as the equilibrium potential $E_{Eq,diss}$.

$$i_{diss} = i_{0,diss} \cdot \exp\left(\frac{F \cdot \eta_{diss}}{RT}\right) \quad [8]$$

$$\eta_{diss} = \Phi_s - \Phi_l - E_{Eq,diss} \quad [9]$$

Table I. Parameters for the side reaction definitions. The superscript *e* indicates estimated values.

Symbol	Parameter	Value
SEI layer		
$E_{Eq,SEI}$	SEI formation equilibrium potential	$0.4 V$ [71]
κ_{SEI}	Li^+ conductivity	$1 \times 10^{-2} S m^{-1}$ [57]
σ_{SEI}	e^- conductivity	$1 \times 10^{-8} S m^{-1}$ [57]
$\delta_{0,SEI}$	Initial thickness	$20 nm$ [56]
ρ_{SEI,Li_2CO_3}	Density of Li_2CO_3	$2110 kg m^{-3}$
M_{SEI,Li_2CO_3}	Molar of mass Li_2CO_3	$73.89 g mol^{-1}$
$\rho_{SEI,LiF}$	Density of LiF	$2640 kg m^{-3}$
$M_{SEI,LiF}$	Molar mass of LiF	$25.94 g mol^{-1}$
Transition-metal dissolution		
$E_{Eq,diss}$	Dissolution equilibrium potential	$4.0 V$ [69]
$i_{0,diss}$	Dissolution exchange current density	$6.05 \times 10^{-6} A m^{-2}$ [e]

The volume fraction of the cathode active material is continuously calculated by the integrated dissolution current density Q_{diss} of HF dissolving transition-metals from the active material.

$$\varepsilon_{s,pos} = \varepsilon_{s,pos,0} - \frac{Q_{diss}}{c_{s,max,pos} \cdot l_{pos} \cdot F} \quad [10]$$

In conclusion to the introduction of the side reaction modeling approach, an overview of all parameters for the previously shown side reactions can be found in Table I.

Results and Discussion

Determination of SEI formation exchange current density.—As mentioned before, we used the experimental data for a NCM/graphite cell from Ecker et al.[51] to test our model and fit relevant parameters. By simulating our model in a calendar aging mode (i.e. no applied external current density), we are able to determine the exchange current density of SEI formation. Electrons for forming the SEI are provided by the anode in calendar as well as cyclic aging. Lithium-ions for the reaction are taken from the electrolyte but to keep the charge balance valid in calender aging, lithium-ions also have to deintercalate from the negative electrode whereas during cyclic aging those lithium-ions are deintercalated from the positive electrode. With the provided data for 35, 40 and $50°C$ at 50% SOC, we determined the SEI formation exchange current density $i_{0,SEI}$ depending on temperature T in an Arrhenius-like behavior as we expect a negligible influence of the cathodic dissolution reaction at this SOC.

$$i_{0,SEI} = 14.7 \times 10^4 A m^{-2} \exp\left(\frac{-86.2 kJ mol^{-1}}{RT}\right) \quad [11]$$

The exchange current density for SEI formation calculates to 3.6, 6.1 and 17.1×10^{-10} A m^{-2} for 35, 40 and $50°C$ respectively and is in agreement with an exchange current density smaller than 1×10^{-7} A m^{-2} as proposed by Fu et al.[45]

The agreement of experimental and simulation data can be seen in Figure 3.

Quantitatively LiF and Li_2CO_3 are formed at the same rate in the calendric regime of the introduced model. This is to be expected as the same reduction potential and an overall side reaction exchange current density $i_{0,SEI}$ is assumed. The incorporation of the two main degradation products is still advisable as it influences the thickness prediction of the SEI by the different molar volumes of LiF and Li_2CO_3 ($V_{m,LiF} = 9.8 \times 10^{-6}$ m^3 mol^{-1}; $V_{m,Li_2CO_3} = 3.5 \times 10^{-5}$ m^3 mol^{-1}).

Capacity fade based on SEI growth during cyclic and calendar aging.—When applying a cyclic aging regime with a 1C rate between 2.75 and 4.2 V (constant current (CC) discharge and constant
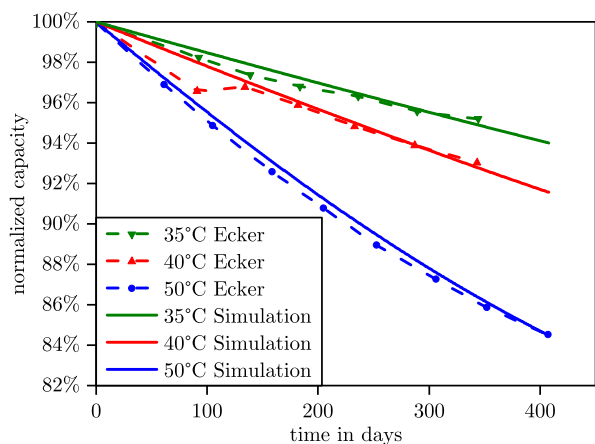
Figure 3. Comparison of experimental data taken from Ecker et al.[51] and data from the proposed model for calendar aging at 50% SOC as a result of SEI formation.
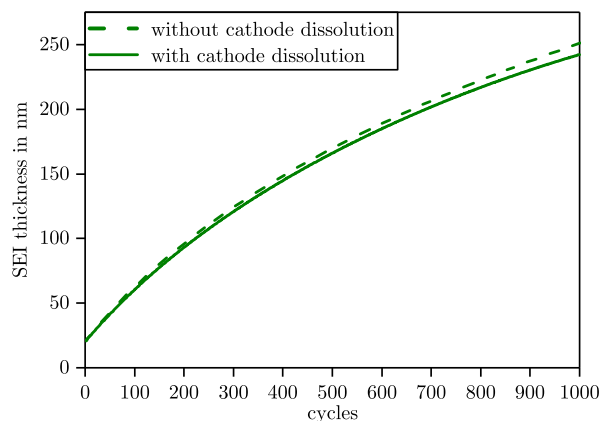

Figure 5. Comparison of the modeled SEI thickness close to the current collector over 1000 cycles with and without an implemented cathode dissolution. The cell was cycled with a 1C rate between 2.75 and 4.2 V.

current-constant voltage (CC-CV) charge), we observe a higher capacity fade due to SEI growth than during calendar aging. One might expect that this increase in capacity fade is solely due to the cracking and re-formation of the SEI which is not occurring during calendar aging. However, as also shown by Purewal et al.[72] the increase in SEI growth is mainly due to the differing overpotentials during cycling and the cracking of the SEI accounts for only a small amount of the total SEI formed.

The overall SEI growth close to the separator and close to the current collector as well as the overall capacity fade as shown in Figure 4 follows a $\sqrt{t}$-behavior. In contrast to Lin et al.,[50] this behavior is not modeled by an exponential decay pre-factor limiting the exchange current density but is based on a different utilized range in the $i_{SEI,n}$-η_{SEI}-curve determining the kinetics of SEI growth. As the kinetics dependency has an exponential shape and the overpotential changes due to the increasing R_{SEI}, the SEI formation current decreases until a state is reached where resistance increase and current density decrease keep the overpotential effectively steady. Due to that quasi-steady state, SEI formation never stops for reasons of the SEI being insulating enough but changes to a linear growth behavior.

Non-linear aging behavior due to cathode dissolution.—As the SEI is not stopping to grow due to kinetic limitations as discussed in the previous section, another effect has to serve as a limiting condition. Our simulations show that the "stabilization" of SEI growth is influenced by the degradation of the positive electrode. This fact – which seems contradictory to what one would expect – is caused by a straightforward circumstance. As cathode degradation outpaces the amount of lost cyclable lithium-ions contributing to SEI growth, less and less lithium-ions are moved from the anode to the cathode during discharge.[5,50] This effect leads to shorter charging times and, therefore, shorter times during which SEI can grow which results in a decrease of SEI growth in each cycle[75] (see Figure 5). The same would hold true with lithium plating as a source of LLI and the consequent decrease of cyclable lithium-ions.

Figure 5 compares the decrease of SEI growth over 1000 cycles close to the current collector with and without an implemented cathode dissolution reaction. The difference in SEI thickness after 1000 cycles is about 10 nm. This thickness difference seems to be very small in comparison to the difference in the corresponding overall capacity fade as depicted in Figure 6 (blue and red line). The reason for the behavior of the model with cathode dissolution is a prolonged
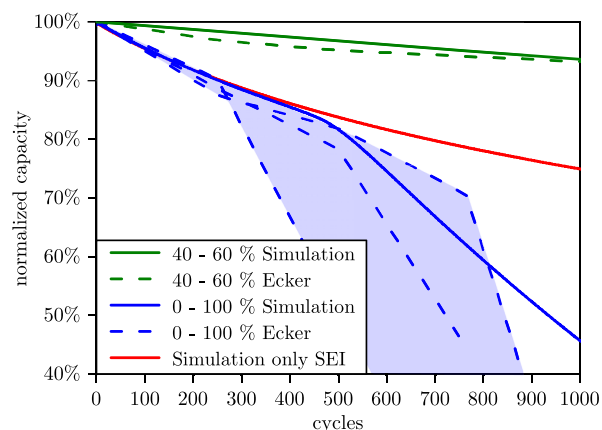

Figure 4. Comparison of the modeled SEI thickness close to the separator and close to the current collector over 1000 cycles. The cell was cycled with a 1C rate between 2.75 and 4.2 V. The difference in growth is due to inhomogeneous current density distribution through the electrodes.[73,74]

Figure 6. Comparison of experimental data taken from Ecker et al.[51] and data from the proposed model for cyclic aging as a result of SEI formation and cathode dissolution. The light blue color covers the range of the three measurements by Ecker et al.[51] Additionally, the red line shows the capacity fade behavior of the model when disabling the cathode dissolution reaction.
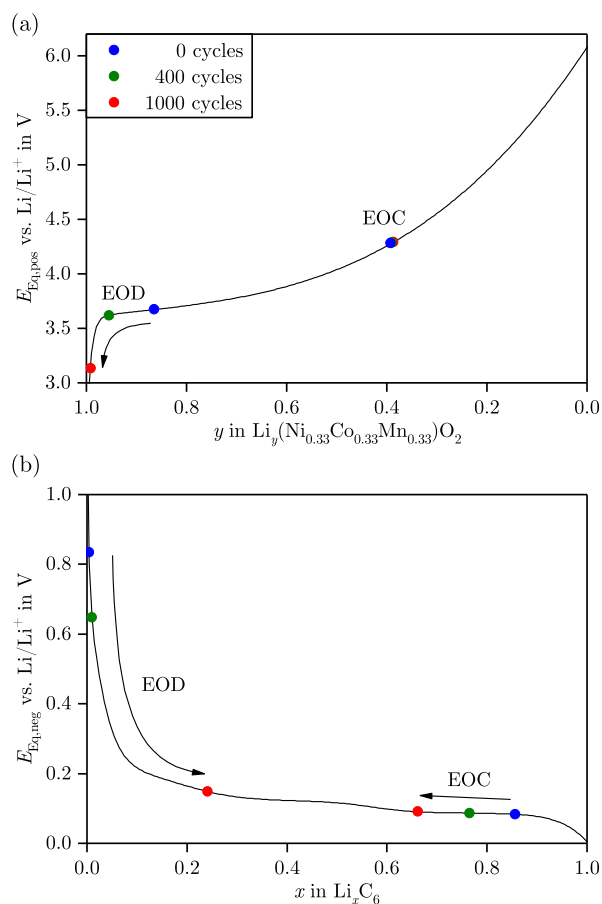
Figure 7. Cathode (a) and anode (b) stoichiometry for initial starting conditions (blue), before the transition to non-linear behavior in the capacity fade curve (green) and after 1000 cycles (red). (For interpretation of the references to color in this figure legend, the reader is referred to the web version of the article.)

Figure 8. (a) Comparison of voltage curve taken from Ecker et al.[51] for 0.25C discharge and data from the proposed model. (b) Exemplary different power fade behavior by changing κ_{SEI} to 1×10^{-7} S m^{-1}.

CV phase during charging due to the side reactions. The CV phase keeps the SEI reaction below the reduction potential and the cathode dissolution reaction above the oxidation potential, so the current does not drop below the stopping criterion of C/20 due to the side reactions. Therefore, the longer CV phase counterbalances the shorter charging time for the intercalation reaction and does not limit the SEI growth as much as expected.

Figure 6 compares the simulated non-linear behavior in usable capacity with experimental results by Ecker et al.[51] The non-linearity in usable capacity occurs as soon as the LAM in the cathode becomes larger than the LLI. Whereas the decrease in the beginning of the capacity fade and the position of the transition zone from linear to non-linear aging behavior are in good agreement, the slope after the transition zone is underestimated by the model. This could be caused by the exclusion of implementing lithium plating as a second source of LLI and will, therefore, be a task for future work.

Figure 7 depicts consequences of the capacity fade on the shift within the stoichiometry – which is the intercalation degree – at the end-of-charge (EOC) and end-of-discharge (EOD). Besides the initial conditions of a non-aged cell, the values of an aged cell before and after the transition to non-linear behavior in the capacity curve of Figure 6 are shown. As expected, the stoichiometry of the anode at the EOC decreases due to LLI (shift from blue to red in Figure 7b). In contrast, the stoichiometry of the cathode at the EOC stays (almost) the same as the anode stays in a stage-1 potential plateau and the
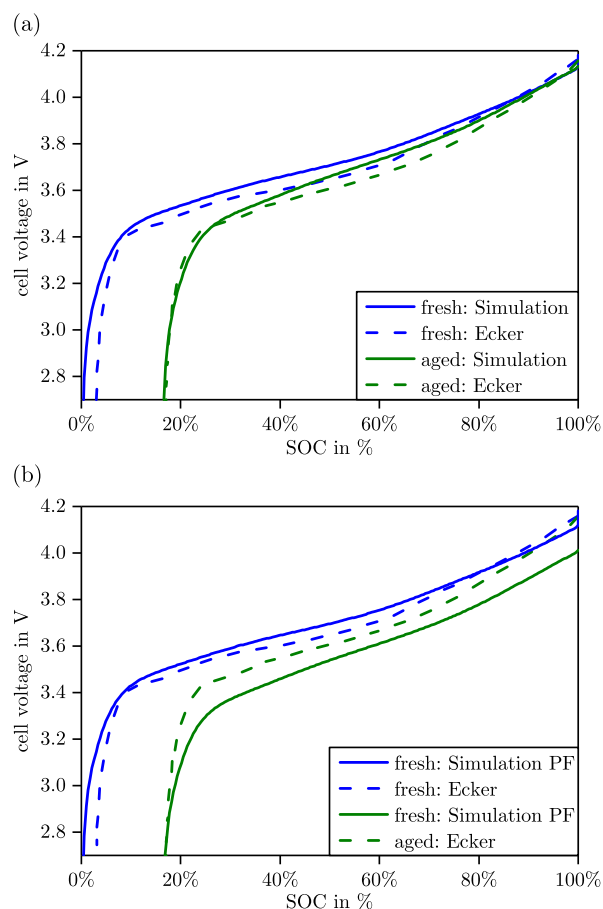
EOC is defined by the cutoff-voltage of the cell at 4.2 V which is the difference between anode and cathode potential.

At the EOD, we see that the cathode stoichiometry increases (shift from blue to red in Figure 7a) as the LAM is higher than the LLI and percentagewise more lithium-ions intercalate in a smaller cathode active material volume. When the cathode stoichiometry at EOD is reaching 1, the anode stoichiometry also increases as the discharge is terminated before all lithium-ions are deintercalated from the anode. Therefore, at this point we see a change from an anode limitation to a cathode limitation of the cell. Those shifts and the half-cell behavior are also in good agreement with measurements and conclusions reported by Kleiner et al.[76] for an NCA/graphite cell.

Capacity and power fade behavior with new model.—Depicted in Figure 8a is the voltage discharge curve of the simulated cell prior and after aging at 100 % SOC and 50 °C compared to data reported in the paper of Ecker et al.[51] As can be seen, the cell shows a capacity fade – recognizable by shorter discharge time – but no significant power fade as voltage levels are almost equal.

Figure 8b shows the exemplary behavior of a cell with a uniform conductivity κ_{SEI} of 1×10^{-7} S m^{-1} for lithium-ions and electrons within the SEI in the order of often used values in literature.[47,77] The plot shows that we get a totally different power behavior as a result and, therefore, prediction of available energy with a model that does not distinguish between the conductivity of electrons and lithium-ions in the SEI – although we calculate the same capacity fade.

With our modeling approach we are able to differentiate between capacity fade and power fade, both resulting in an energy loss during aging. We thereby get the possibility to gain new insights into SEI properties for different cell systems and material combinations in future work.

Conclusions

In this paper we introduced a new approach for modeling aging behavior that distinguishes between electronic (σ_{SEI}) and ionic (κ_{SEI}) conductivity of the SEI. By this approach we do not only represent the SEI in a way that is more accurate but we can also differentiate between capacity and power fade which is inextricably connected in a single conductivity approach.

The model shows good agreement with experimental data from Ecker et al.[51] as not only an SEI growth due to non-ideal insulation properties and re-formation after cyclic cracking but also a cathode dissolution reaction is implemented. With this cathodic aging mechanism, the transition to non-linear behavior in retrievable capacity can be explained.

Future work will add further aging mechanisms on both electrodes, like e.g. lithium plating and a cathode electrolyte interphase (CEI) formation, to the existing model to get a more thorough understanding of the interactions between the different mechanisms.

Appendix

The P2D model is based on porous electrode and concentrated solution theory and solves lithium-ion concentration c_i and potential Φ_i within the liquid electrolyte (subscript $i = l$) and the solid active material (subscript $i = s$) phase. The model geometry is defined as a one dimensional interval divided into three main domains corresponding to the graphite electrode, the separator and the NCM electrode. An additional dimension is set for the description of species intercalation within the particle domain. For a detailed model description, the reader is referred to Reference 29. The main equations are mass balance for lithium-ions in the electrolyte c_l

$$\varepsilon_l \frac{\partial c_l}{\partial t} = \nabla \left(D_{l,eff} \nabla c_l - \frac{\mathbf{i}_l t_+}{F} \right) + a_s j_n \qquad [A1]$$

and charge balance

$$\nabla \left(-\kappa_{eff} \nabla \Phi_l + \frac{2\kappa_{eff} RT}{F} \left(1 + \frac{\partial \ln f_\pm}{\partial \ln c_l} \right) (1 - t_+) \nabla \ln c_l \right) = F a_s j_n \qquad [A2]$$

throughout the electrode domain. The current within the liquid phase is described by the current density $\mathbf{i}_l$ and potential Φ_l, while the pore wall flux at the electrode-electrolyte interface is named j_n. R describes the universal gas constant, F the Faraday's constant and T the local absolute temperature. Within the separator domain the equations simplify to

$$\varepsilon_l \frac{\partial c_l}{\partial t} = \nabla \left(D_{l,eff} \nabla c_l - \frac{\mathbf{i}_l t_+}{F} \right) \qquad [A3]$$

and

$$\nabla \left(-\kappa_{eff} \nabla \Phi_l + \frac{2\kappa_{eff} RT}{F} \left(1 + \frac{\partial \ln f_\pm}{\partial \ln c_l} \right) (1 - t_+) \nabla \ln c_l \right) = 0 \qquad [A4]$$

To couple solid and liquid phase, Butler-Volmer kinetics are assumed for the pore wall flux

$$j_n = k_c^{\alpha_a} k_a^{\alpha_c} \left(c_{s,max} - c_s|_{r=r_p} \right)^{\alpha_a} \left(c_s|_{r=r_p} \right)^{\alpha_c} \left(\frac{c_l}{1\,\text{mol m}^{-3}} \right)^{\alpha_a} \left(e^{\frac{\alpha_a F}{RT}\eta} - e^{-\frac{\alpha_c F}{RT}\eta} \right) \qquad [A5]$$

including the lithium-ion concentration at the particle's surface c_s and the overpotential

$$\eta = \Phi_s - \Phi_l - E_{Eq} \qquad [A6]$$

where Φ_s corresponds to the solid phase potential.

Effective transport parameters are used to account for tortuosity in the homogenized P2D model by scaling material parameters with MacMullin's number – a function of

---

Table AI. Physicochemical model parameters measured and estimated from a Samsung ICR-22F 18650-cell. Superscript *m* indicates measured values and *e* estimated values.

Parameter	Anode	Separator	Cathode
Geometry			
Thickness l	$77\,\mu\text{m}^{\,m}$	$18\,\mu\text{m}^{\,m}$	$79\,\mu\text{m}^{\,m}$
Particle radius r_p	$10\,\mu\text{m}^{\,m}$		$4\,\mu\text{m}^{\,m}$
Solid phase fraction ε_s	$0.56^{\,m}$		$0.59^{\,m}$
Liquid phase fraction ε_l	$0.33^{\,m}$	$0.4^{\,m}$	$0.33^{\,m}$
Thermodynamics			
Equilibrium voltage E_{Eq}	see Equation A8 [81]		see Equation A9 [80]
Maximum Li$^+$ concentration $c_{s,max}$	$31363\,\text{mol m}^{-3}$		$51385\,\text{mol m}^{-3}$
Initial state of charge $\frac{c_{s,0}}{c_{s,max}}$	$0.85^{\,e}$		$0.395^{\,e}$
Kinetics			
Reaction rate constant k_{ref}	$1 \times 10^{-11}\,\text{m s}^{-1\,e}$		$1 \times 10^{-11}\,\text{m s}^{-1\,e}$
Anodic charge-transfer coefficient α_a	$0.5^{\,e}$		$0.5^{\,e}$
Cathodic charge-transfer coefficient α_c	$0.5^{\,e}$		$0.5^{\,e}$
Transport			
Solid diffusivity D_s	$3.9 \times 10^{-14}\,\text{m}^2\,\text{s}^{-1\,e}$		$8 \times 10^{-14}\,\text{m}^2\,\text{s}^{-1\,e}$
Solid conductivity σ	$100\,\text{S m}^{-1\,e}$		$2\,\text{S m}^{-1\,e}$
MacMullin number N_M	12 [82]	10 [82]	10 [82]

Parameter	Electrolyte
Electrolyte concentration c_l	$1000\,\text{mol m}^{-3\,e}$
Electrolyte diffusivity D_l	see Equation A10 [79]
Electrolyte conductivity κ	see Equation A11 [79]
Activity dependency $\frac{\partial \ln f_\pm}{\partial \ln c_l}$	see Equation A12 [79]
Transport number t_+	0.38 [79]

porosity ε_l and tortuosity τ[78]

$$\Psi_{l,eff} = \frac{\varepsilon_l}{\tau} \Psi_l = \frac{1}{N_M} \Psi_l \qquad [A7]$$

To describe the electrolyte's characteristics properly, a concentration dependence is implemented for conductivity, diffusivity and mean molar activity coefficient of the electrolyte. These are taken from fittings to measurements[79] while presuming a constant transport number. The applied diffusion coefficients are estimated from various literature sources.[29,30,80,81] The equilibrium potential is taken from literature[81] as well as the maximum concentration of lithium within active material particles.[71,81] Additional parameters such as reaction rate constants[80,81] are assumed based on references from literature.

The chosen parameters for the above introduced model – measured or taken from literature – are summarized in Table AI.

Equilibrium voltage curves dependent on the degree of lithiation x or y for the negative electrode $E_{Eq,neg}$ by Safari et al.[81] and the positive electrode $E_{Eq,pos}$ by Stewart et al.[80]

$$E_{Eq,neg} = 0.6379 + (0.5416 \cdot \exp(-305.5309 \cdot x)) + 0.044 \cdot \tanh\left(\frac{-x + 0.1958}{0.1088}\right)$$

$$- 0.1978 \cdot \tanh\left(\frac{x - 1.0571}{0.0854}\right) - 0.6875 \cdot \tanh\left(\frac{x + 0.0117}{0.0529}\right)$$

$$- 0.0175 \cdot \tanh\left(\frac{x - 0.5692}{0.0875}\right) \qquad [A8]$$

$$E_{Eq,pos} = 6.0826 - 6.9922 \cdot y + 7.1062 \cdot y^2 - 0.54549 \cdot 10^{-4} \cdot \exp(124.23 \cdot y - 114.2593)$$

$$- 2.5947 \cdot y^3 \qquad [A9]$$

Analytical dependencies for electrolyte diffusivity D_l, conductivity κ and activity $\frac{\partial \ln f_\pm}{\partial \ln c_l}$ as functions of temperature T, lithium-ion concentration in the liquid phase c_l and transport number t_+ as measured by Valøen et al.[79]

$$D_l = 10^{-4.43 - \frac{54}{T - (229 + 5 \cdot c_l)} - 0.22 \cdot c_l} \cdot 10^{-4} \qquad [A10]$$

$$\kappa = 0.1 \cdot c_l \cdot (-10.5 + 0.074 \cdot T - 6.96 \cdot 10^{-5} \cdot T^2 + 0.668 \cdot c_l - 0.0178 \cdot c_l \cdot T$$

$$+ 2.8 \cdot 10^{-5} \cdot c_l \cdot T^2 + 0.494 \cdot c_l^2 - 8.86 \cdot 10^{-4} \cdot c_l^2 \cdot T)^2 \qquad [A11]$$

$$\frac{\partial \ln f_\pm}{\partial \ln c_l} = \frac{0.601 - 0.24 \cdot c_l^{0.5} + 0.982 \cdot c_l^{1.5} \cdot (1 - 0.0052 \cdot (T - 294))}{1 - t_+} - 1 \qquad [A12]$$

References

1. M. Armand and J.-M. Tarascon, *Nature*, **451**, 652 (2008).
2. J.-M. Tarascon, *Electrochemical Society Interface*, **25**, 79 (2016).
3. B. Scrosati and J. Garche, *Journal of Power Sources*, **195**, 2419 (2010).
4. S. Passerini and B. Scrosati, *Electrochemical Society Interface*, **25**, 85 (2016).
5. R. M. Spotnitz, *Journal of Power Sources*, **113**, 72 (2003).
6. V. A. Agubra and J. W. Fergus, *Materials*, **6**, 1310 (2013).
7. V. A. Agubra and J. W. Fergus, *Journal of Power Sources*, **268**, 153 (2014).
8. P. Arora, R. E. White, and C. M. Doyle, *Journal of The Electrochemical Society*, **145**, 3647 (1998).
9. D. Aurbach, *Journal of Power Sources*, **89**, 206 (2000).
10. D. Aurbach, B. Markovsky, G. Salitra, E. Markevich, Y. Talyossef, M. Koltypin, L. F. Nazar, B. Ellis, and D. Kovacheva, *Journal of Power Sources*, **165**, 491 (2007).
11. C. R. Birkl, M. R. Roberts, E. McTurk, P. G. Bruce, and D. A. Howey, *Journal of Power Sources*, **341**, 373 (2017).
12. M. Broussely, P. Biensan, F. Bonhomme, P. Blanchard, S. Herreyre, K. Nechev, and R. J. Staniewicz, *Journal of Power Sources*, **146**, 90 (2005).
13. P. Verma, P. Maire, and P. Novák, *Electrochimica Acta*, **55**, 6332 (2010).
14. J. Vetter, P. Novák, M. R. Wagner, C. Veit, K.-C. Möller, J. O. Besenhard, M. Winter, M. Wohlfahrt-Mehrens, C. Vogler, and A. Hammouche, *Journal of Power Sources*, **147**, 269 (2005).
15. J. Christensen and J. S. Newman, *Journal of The Electrochemical Society*, **152**, A818 (2005).
16. Q. Zhang and R. E. White, *Journal of Power Sources*, **179**, 793 (2008).
17. X. Han, M. Ouyang, L. Lu, J. Li, Y. Zheng, and Z. Li, *Journal of Power Sources*, **251**, 38 (2014).
18. M. Dubarry, C. Truchot, and B. Y. Liaw, *Journal of Power Sources*, **219**, 204 (2012).
19. V. Ramadesigan, Paul W. C. Northrop, S. De, S. Santhanagopalan, R. D. Braatz, and V. R. Subramanian, *Journal of The Electrochemical Society*, **159**, R31 (2012).
20. A. Jokar, B. Rajabloo, M. Désilets, and M. Lacroix, *Journal of Power Sources*, **327**, 44 (2016).
21. P. Ganesh, P. R. C. Kent, and D.-e. Jiang, *The Journal of Physical Chemistry C*, **116**, 24476 (2012).
22. D. Marrocchelli, C. Merlet, and M. Salanne In *Physical Multiscale Modeling and Numerical Simulation of Electrochemical Devices for Energy Conversion and Storage*; A. A. Franco, M. L. Doublet, and W. G. Bessler, Eds.; Green Energy and Technology; Springer: London, 2016; pp 61–89.
23. S. Ogata, N. Ohba, and T. Kouno, *The Journal of Physical Chemistry C*, **117**, 17960 (2013).
24. E. Zvereva, D. Caliste, and P. Pochet, *Carbon*, **111**, 789 (2017).
25. M. Saubanère, J.-S. Filhol, and M. L. Doublet In *Physical Multiscale Modeling and Numerical Simulation of Electrochemical Devices for Energy Conversion and Storage*; A. A. Franco, M. L. Doublet, and W. G. Bessler, Eds.; Green Energy and Technology; Springer: London, 2016; pp 1–36.
26. N. G. Hörmann, M. Jäckle, F. Gossenberger, T. Roman, K. Forster-Tonigold, M. Naderian, S. Sakong, and A. Groß, *Journal of Power Sources*, **275**, 531 (2015).
27. K. Ushirogata, K. Sodeyama, Z. Futera, Y. Tateyama, and Y. Okuno, *Journal of The Electrochemical Society*, **162**, A2670 (2015).
28. J. S. Newman and K. E. Thomas-Alyea *Electrochemical systems*, 3rd ed.; Wiley-Interscience: Hoboken, NJ, 2004.
29. T. F. Fuller, C. M. Doyle, and J. S. Newman, *Journal of The Electrochemical Society*, **141**, 982 (1994).
30. C. M. Doyle, T. F. Fuller, and J. S. Newman, *Journal of The Electrochemical Society*, **140**, 1526 (1993).
31. D. Zhang, B. N. Popov, and R. E. White, *Journal of The Electrochemical Society*, **147**, 831 (2000).
32. J. S. Newman and C. W. Tobias, *Journal of The Electrochemical Society*, **109**, 1183 (1962).
33. S. Santhanagopalan, Q. Guo, P. Ramadass, and R. E. White, *Journal of Power Sources*, **156**, 620 (2006).
34. L. Kang, X. Zhao, and J. Ma, *Applied Energy*, **121**, 20 (2014).
35. W. Waag, S. Käbitz, and D. U. Sauer, *Applied Energy*, **102**, 885 (2013).
36. U. Tröltzsch, O. Kanoun, and H.-R. Tränkler, *Electrochimica Acta*, **51**, 1664 (2006).
37. H. Schranzhofer, J. Bugajski, H. J. Santner, C. Korepp, K.-C. Möller, J. O. Besenhard, M. Winter, and W. Sitte, *Journal of Power Sources*, **153**, 391 (2006).
38. D. Andre, M. Meiler, K. Steiner, H. Walz, T. Soczka-Guth, and D. U. Sauer, *Journal of Power Sources*, **196**, 5349 (2011).
39. D. Andre, M. Meiler, K. Steiner, C. Wimmer, T. Soczka-Guth, and D. U. Sauer, *Journal of Power Sources*, **196**, 5334 (2011).
40. J. C. Burns, R. Petibon, K. J. Nelson, N. N. Sinha, A. Kassam, B. M. Way, and J R Dahn. *Journal of The Electrochemical Society*, **160**, A1668 (2013).
41. H. Dai, T. Xu, L. Zhu, X. Wei, and Z. Sun, *Applied Energy*, **184**, 119 (2016).
42. K. Fang, D. Mu, S. Chen, B. Wu, and F. Wu, *Journal of Power Sources*, **208**, 378 (2012).
43. T. R. Ashwin, Y. M. Chung, and J. Wang, *Journal of Power Sources*, **328**, 586 (2016).
44. T. R. Ashwin, A. McGordon, and P. A. Jennings, *Electrochimica Acta*, **232**, 203 (2017).
45. R. Fu, S.-Y. Choe, V. A. Agubra, and J. W. Fergus, *Journal of Power Sources*, **278**, 506 (2015).
46. M. T. Lawder, Paul W. C. Northrop, and V. R. Subramanian, *Journal of The Electrochemical Society*, **161**, A2099 (2014).
47. M. Rashid and A. Gupta, *ECS Electrochemistry Letters*, **3**, A95 (2014).
48. L. Cai, Y. Dai, M. Nicholson, R. E. White, K. Jagannathan, and G. Bhatia, *Journal of Power Sources*, **221**, 191 (2013).
49. L. L. Lam and R. B. Darling, *Journal of Power Sources*, **276**, 195 (2015).
50. X. Lin, J. Park, L. Liu, Y. K. Lee, A. M. Sastry, and W. Lu, *Journal of The Electrochemical Society*, **160**, A1701 (2013).
51. M. Ecker, N. Nieto, S. Käbitz, J. Schmalstieg, H. Blanke, A. Warnecke, and D. U. Sauer, *Journal of Power Sources*, **248**, 839 (2014).
52. K. Xu, *Chemical Reviews*, **104**, 4303 (2004).
53. D. Li, D. Danilov, Z. Zhang, H. Chen, Y. Yang, and P. H. L. Notten, *Journal of The Electrochemical Society*, **162**, A858 (2015).
54. J. Yan, B.-J. Xia, Y.-C. Su, X.-Z. Zhou, J. Zhang, and X.-G. Zhang, *Electrochimica Acta*, **53**, 7069 (2008).
55. M. B. Pinson and M. Z. Bazant, *Journal of The Electrochemical Society*, **160**, A243 (2013).
56. S. J. Harris and P. Lu, *The Journal of Physical Chemistry C*, **117**, 6481 (2013).
57. J. B. Goodenough and Y. Kim, *Chemistry of Materials*, **22**, 587 (2010).
58. S. Ramesh and B. Krishnamurthy, *Journal of The Electrochemical Society*, **162**, A545 (2015).
59. L. Liu, J. Park, X. Lin, A. M. Sastry, and W. Lu, *Journal of Power Sources*, **268**, 482 (2014).
60. M. Gauthier, T. J. Carney, A. Grimaud, L. Giordano, N. Pour, H.-H. Chang, D. P. Fenning, S. F. Lux, O. Paschos, C. Bauer, F. Maglia, S. Lupart, P. Lamp, and Y. Shao-Horn, *The Journal of Physical Chemistry Letters*, **6**, 4653 (2015).
61. H. Ekström and G. Lindbergh, *Journal of The Electrochemical Society*, **162**, A1003 (2015).
62. I. Laresgoiti, S. Käbitz, M. Ecker, and D. U. Sauer, *Journal of Power Sources*, **300**, 112 (2015).
63. H. J. Ploehn, P. Ramadass, and R. E. White, *Journal of The Electrochemical Society*, **151**, A456 (2004).
64. S. F. Schuster, T. C. Bach, E. Fleder, J. Müller, M. J. Brand, G. Sextl, and A. Jossen, *Journal of Energy Storage*, **1**, 44 (2015).
65. T. C. Bach, S. F. Schuster, E. Fleder, J. Müller, M. J. Brand, H. Lorrmann, A. Jossen, and G. Sextl, *Journal of Energy Storage*, **5**, 212 (2016).
66. Y. Domi, T. Doi, M. Ochida, T. Yamanaka, T. Abe, and Z. Ogumi, *Journal of The Electrochemical Society*, **163**, A2849 (2016).

67. I. Buchberger, S. Seidlmayer, A. Pokharel, M. Piana, J. Hattendorff, P. Kudejova, R. Gilles, and H. A. Gasteiger, *Journal of The Electrochemical Society*, **162**, A2737 (2015).
68. B. Vortmann-Westhoven, M. Winter, and S. Nowak, *Journal of Power Sources*, **346**, 63 (2017).
69. A. Bhandari and J. Bhattacharya, *Journal of The Electrochemical Society*, **164**, A106 (2017).
70. A. Banerjee, Y. Shilina, B. Ziv, J. M. Ziegelbauer, S. Luski, D. Aurbach, and I. C. Halalay, *Journal of The Electrochemical Society*, **164**, A6315 (2017).
71. P. Ramadass, B. S. Haran, P. M. Gomadam, R. E. White, and B. N. Popov, *Journal of The Electrochemical Society*, **151**, A196 (2004).
72. J. Purewal, J. S. Wang, J. Graetz, S. Soukiazian, H. Tataria, and M. W. Verbrugge, *Journal of Power Sources*, **272**, 1154 (2014).
73. F. M. Kindermann, P. J. Osswald, S. Klink, G. Ehlert, J. Schuster, A. Noel, S. V. Erhard, W. Schuhmann, and A. Jossen, *Journal of Power Sources*, **342**, 638 (2017).
74. F. M. Kindermann, P. J. Osswald, G. Ehlert, J. Schuster, A. Rheinfeld, and A. Jossen, *Journal of The Electrochemical Society*, **164**, E3105 (2017).
75. A. M. Colclasure, K. A. Smith, and R. J. Kee, *Electrochimica Acta*, **58**, 33 (2011).
76. K. Kleiner, P. Jakes, S. Scharner, V. Liebau, and H. Ehrenberg, *Journal of Power Sources*, **317**, 25 (2016).
77. G. Ning, R. E. White, and B. N. Popov, *Electrochimica Acta*, **51**, 2012 (2006).
78. M. J. Martínez-Rodríguez, S. Shimpalee, and J. W. van Zee, *Journal of The Electrochemical Society*, **156**, B80 (2009).
79. L. O. Valøen and J. N. Reimers, *Journal of The Electrochemical Society*, **152**, A882 (2005).
80. S. G. Stewart, V. Srinivasan, and J. S. Newman, *Journal of The Electrochemical Society*, **155**, A664 (2008).
81. M. Safari and C. Delacourt, *Journal of The Electrochemical Society*, **158**, A562 (2011).
82. J. Landesfeind, A. Ehrl, M. Graf, W. A. Wall, and H. A. Gasteiger, *Journal of The Electrochemical Society*, **163**, A1254 (2016).

4 Charge Distribution in Graphite Electrodes

Resulting from advancements in the quality of manufacturing processes, the ratio between active and inactive components can be improved by realizing thicker electrode coatings and thinner current collector foils.[70] However, this increase in energy density of the cells comes with longer charging times due to a reduced rate capability. While concepts such as intelligent charging strategies require a comprehensive framework to be implemented,[183] the most obvious approach is to increase charging power.

Various publications address the variations in current density distribution and the resulting inhomogeneities as an effect of high charging currents. The impact of the cell design and the resulting equilibration processes along the electrodes are presented using experimental cells[184–191] or by a modeling approach.[192,193] The resulting inhomogeneous utilization of the active material leads to undesired side reactions and accelerated degradation, especially lithium-plating[194,195] and an uneven mechanical expansion of the anode.[196] This is further provoked by the increasing thickness of the cell's electrodes. In contrast to the equilibrating process along the electrode, only limited knowledge regarding the process throughout the electrode thickness is available. Consequently, a fundamental understanding of the lithium-ion transport mechanisms is a crucial requirement to enable intelligent fast charging strategies and homogeneous aging behavior.

In this chapter EIS measurements are introduced as a promising candidate to determine the quality of the formation in an end-of-line testing scenario as EIS is a commonly used method for state estimation. As equilibration processes affect impedance measurements, a hypothesis is presented, discussing possible lithium-ion relaxation pathways inside a lithium-ion cell. The first effect being an equilibration inside the particles, where the concentration gradient between the bulk and the surface of graphite particles leads to an intra-particle equilibration process. The second effect addresses the equilibration between different particles (inter-particle), where the equilibration of the lithium-ion concentration gradient occurs through the electrolyte. This equilibration is observed using an experimental test cell, where the anode consists of three separated graphite layers[197] based on the works of La Mantia et al.,[198] Ng et al.[199] and Klink et al.[200,201] The results from the laboratory cell were incorporated in a new P2D model with three distinctive particle radii to account for the equilibration processes. An electrode design study was carried out using the model that resulted in an electrode design that showed an improved performance in a rate capability test.

4.1 Impedance spectroscopy as a qualitative method to measure equilibration processes

EIS is a measurement technique to determine the alternating current (AC) resistance of a device under test. In this case, that means applying an AC current signal over a defined frequency range to a lithium-ion battery and measuring the potential response. This method is called a galvanostatic EIS

whereas in a potentiostatic EIS an applied potential signal would induce a current response.[202,203]

The applied sinusoidal current signal in the time domain is described by

$$i(t) = \widehat{i} \cdot \sin(\omega t) = \widehat{i} \cdot e^{j(\omega t)} \tag{4.1}$$

with the current amplitude $\widehat{i}$ and angular frequency $\omega = 2\pi f$. As an impedance measurement requires a linear time-invariant system, the measured potential response includes an offset of the phase shift ϕ

$$E(t) = \widehat{E} \cdot \sin(\omega t + \phi) = \widehat{E} \cdot e^{j(\omega t + \phi)} \tag{4.2}$$

After transformation to the frequency domain, the complex impedance $Z(\omega)$ is calculated by Ohm's law and given in polar coordinates or separated as a real ($Z'(\omega)$) and an imaginary ($Z''(\omega)$) part[202]

$$Z(\omega) = \frac{E(\omega)}{i(\omega)} = |Z(\omega)| \cdot e^{-j\phi} = |Z(\omega)| \cdot (\cos\phi - j \cdot \sin\phi) = Z'(\omega) - j \cdot Z''(\omega) \tag{4.3}$$

This second representation of the real as well as imaginary part of the impedance gives to coordinates for every frequency that can be depicted in a so-called Nyquist diagram. A typical Nyquist plot for a lithium-ion cell is given in Figure 4.1. As solid state objects such as the electrodes in a lithium-ion cell exhibit mostly resistive and capacitive behavior which are represented in the negative imaginary half plane, a common depiction shows the negative imaginary half plane in the upper half.[202]
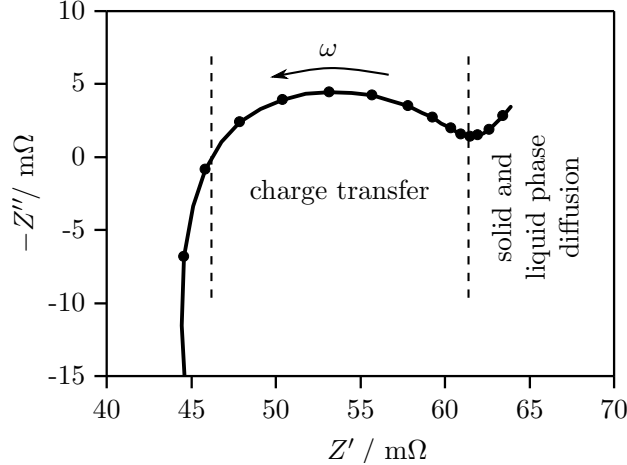
Figure 4.1: Exemplary Nyquist representation of a *Samsung* NCM/graphite cell as used in Section 4.3 measured at 25 °C and 50 % SOC with typical frequency regions assigned to certain electrochemical phenomena.[202,203] Tested frequencies were 10 kHz to 70 mHz with a 50 mA current amplitude.

As the Nyquist depiction disregards the frequency dependency of the measurements, another common representation is the so-called Bode plot. In a Bode plot, as shown in Figure 4.2, $Z(\omega)$ is represented as absolute value $|Z(\omega)|$ and phase shift ϕ over frequency.[204]

EIS was established as a qualitative method to measure equilibration processes after an inhomogeneous current density distribution. Therefore, the used measurement equipment and protocol for Section 4.3 are introduced in the following paragraphs.
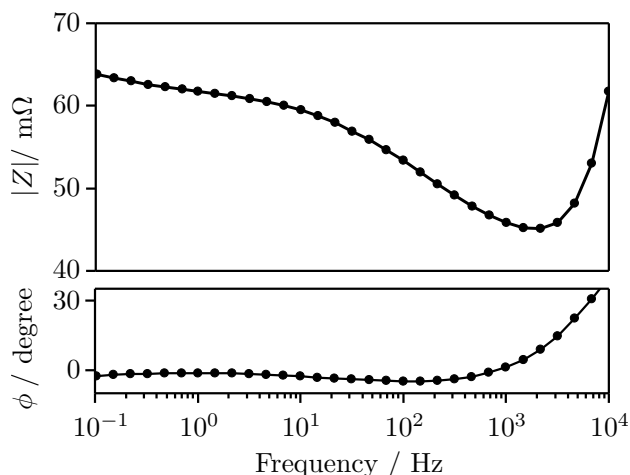
Figure 4.2: Bode plot of the same cell and measurement as shown in Figure 4.1.

Three cells from five different manufactures were tested in the experimental setup. The presented cycling and impedance measurements were carried out with a VMP3 potentiostat/galvanostat from *Bio-Logic SAS* in a temperature chamber. The temperature was set prior to all charging actions for at least 1 h to give the cells enough time to adapt to a temperature change. Previous to all EIS measurements all cells were charged with a 1C rate to the maximum potential given by the manufacturer in a constant-current/constant-voltage (CCCV) charging mode (CV terminated after 1 h). After a pause of 15 min the cells were discharged with 1C to their respective minimum potential which was also kept for an hour or terminated when the remaining current dropped beneath C/100 (i.e. CCCV mode). Before charging again with the same parameters as before, another pause of 15 min was kept. This charging step was followed by a 1 h pause and at last, the cells were discharged with 1C to their intended SOC by ampere-hour counting.

Following the SOC setting of the cell, impedances were measured over a time of 48 h, starting with every 10 min for the first hour, then every 30 min for the next two hours and finally every hour for the remaining time. Since no change in cell potential was observed after 4 to 5 h, self-discharge or side reactions are not considered to be of significant influence. Each EIS measurement was succeeded by an open-circuit potential phase. The tested frequencies were 10 kHz to 70 mHz with 6 points per decade and 3 sine waves per frequency (only 2 for frequencies lower than 700 mHz). Measurements were carried out in galvanic mode (current excitation and potential response) with a 50 mA amplitude, which was small compared to the capacities of the tested cells, and no DC offset. The resulting measurement time of about 120 s was short compared to the overall relaxation time. With the small excitation amplitude and the short perturbation time, the requirement of stationary conditions was fulfilled.[205]

4.2 Multi-layer cell setup to quantify exchanged amount of charge during equilibration

For the experiments in Sections 4.4 and 4.5 to measure relaxation effects inside an electrode layer, a laboratory cell introduced by Klink[200] was used. The setup of the cell with its several individual working electrode layers – therefore called multi-layer cell (MLC) – can be seen in the provided scheme

in Figure 4.3. In this work, a setup with three graphite electrodes was chosen for a proof-of-principle. Details on the used cell and measurement setup will be given in the following subsections.
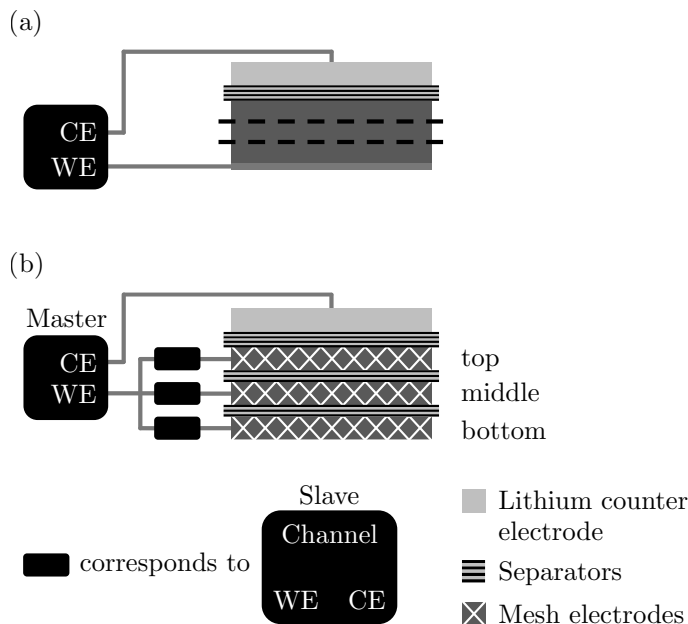

Figure 4.3: Scheme of MLC with (a) showing the cross section of a typical half-cell measurement versus a lithium-metal counter electrode (CE) (dashed lines represent the exemplary sectioning of this electrode) and (b) depicting the MLC setup with each layer being connected to a single potentiostat – called slave channel. A separate master channel is used for applying the current between the lithium counter electrode and the three working electrodes (WE).

4.2.1 Cell preparation and initial operation

Two graphites from *SGL Carbon GmbH* were experimentally tested. The first graphite was specified with a D50 value of 19 µm (subsequently referred to as large particle graphite – LG) and the second graphite had a D50 value of 2.3 µm (small particle graphite – SG) according to the manufacturer. The preparation of the corresponding electrodes and the assembly of the MLC setup are included in the following paragraphs.

Electrode preparation and characterization Both graphites were processed in a similar fashion. The graphite containing slurry and PVdF binder (*Sigma-Aldrich*) were mixed in a 95:5 weight ratio in NMP (*Sigma-Aldrich*) solvent. The slurry was coated by an automatic coater (*RK Print*) on a Microgrid Cu25 copper mesh (provided by *Dexmet Corporation*) in the case of LG and on a MC33 copper mesh (*Precision Eforming Ltd.*) in the case of SG. The meshes were chosen for their thickness of only 24 µm (Microgrid Cu25) and 9 µm (MC33) as well as a porosity of about 60 %. The coating speed for both coatings was 1.5 m/min.

Pressing the coated LG electrodes with a hydraulic stamping press for 2 min with 2.5 t, resulted in an electrode porosity of 32 % and a thickness of 44 µm which corresponds to a loading of 4.13 mg/cm². SG electrodes were not treated due to mechanical instabilities arising during the pressing process, resulting

in a porosity of 79 %, a thickness of 42.5 µm and a loading of 1.82 mg/cm². Respective tortuosities for both kinds of electrodes were measured and calculated as suggested by Landesfeind et al.[170]

For measuring the tortuosity of the used mesh electrodes, symmetrical cells were assembled with facing coating sides ("top graphite") as well as with facing mesh sides ("top mesh") to see the influence of the mesh structure. The obtained EIS spectra for the electrodes are shown in Nyquist depiction in Figure 4.4.
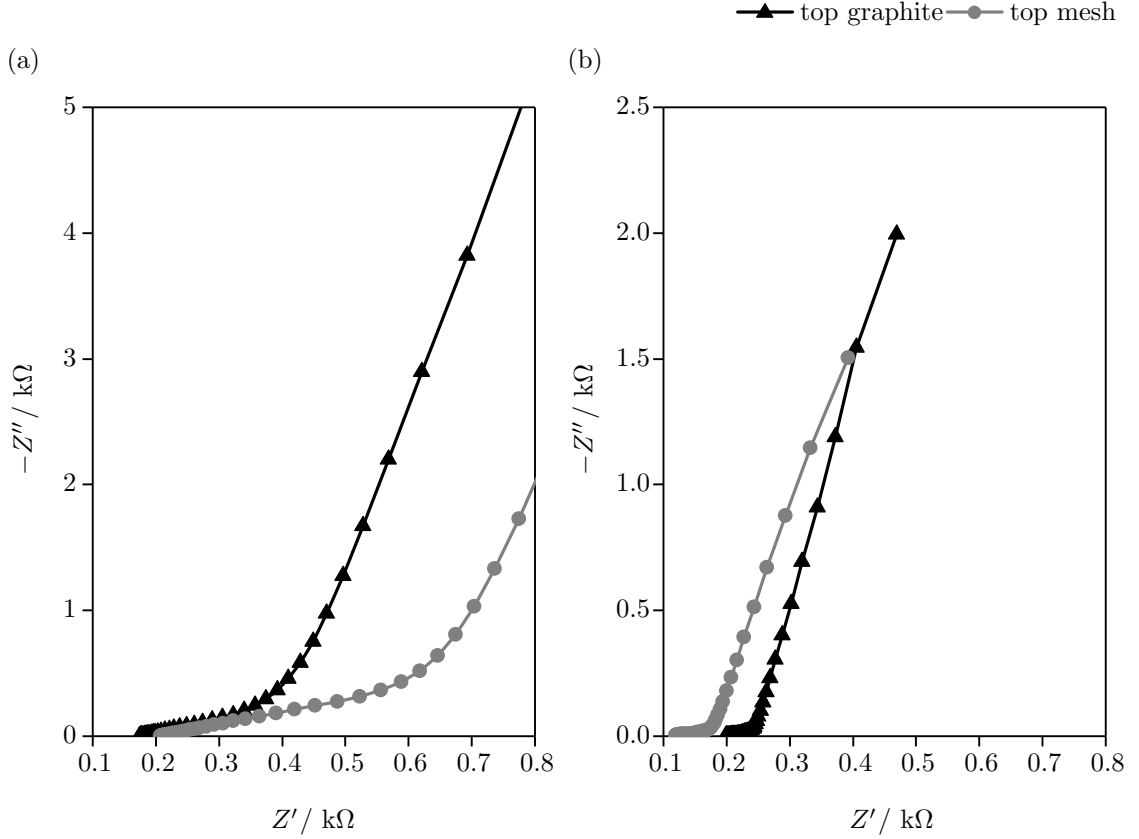
Figure 4.4: Obtained impedance spectra in Nyquist depiction for (a) LG electrodes and (b) SG electrodes both in "top graphite" as well as "top mesh" configuration.

According to Landesfeind et al.,[170] the ionic resistance R_{ion} inside the electrolyte phase determines the charge transport in porous particle networks or structures. Such porous structures are e.g. electrodes and separators in commercially used lithium-ion batteries. With the ionic resistance, MacMullin's number can be calculated via Ohm's law when the conductivity of the non-intercalating electrolyte κ as well as the cross-sectional area A of the tested material with its respective thickness d is known. By also knowing the porosity of the material, a tortuosity value can be given.

$$N_M = \frac{\tau}{\varepsilon} = \frac{R_{ion} \cdot A \cdot \kappa}{d} \tag{4.4}$$

To obtain the ionic resistance experimentally, an EIS has to be carried out on symmetrical cells. The measured data can either be fitted to

$$Z_{LFR} = \sqrt{\frac{R_{ion}}{Q_S(i\omega)^\gamma}} \coth\left(\sqrt{Q_S(i\omega)^\gamma R_{ion}}\right) \tag{4.5}$$

where Z_{LFR} refers to the linear extrapolation of the low frequency resistance branch to the real part axis Z', Q_{S} sums up all capacitive contributions in a constant-phase element and γ corresponds to the constant-phase exponent (if $\gamma = 1$, Q_{S} simplifies to a capacitor C_{S}).

The other approach is via a second linear extrapolation of the high frequency resistance R_{HFR} and a subsequent calculation by

$$R_{\text{ion}} = 3 \cdot (Z_{\text{LFR}} - R_{\text{HFR}}) \tag{4.6}$$

The obtained tortuosity values in the case of LG electrodes are 4.892 for the "top graphite" and 4.907 for the "top mesh" measurement which is within the margin of error, so an influence of the mesh could be ruled out. The SG electrode tortuosity value is smaller with 2.723 for the "top graphite" and 3.684 for the "top mesh" measurement. This can be expected due to the higher porosity of the SG electrodes ($\varepsilon_{\text{SG}} \approx 79\,\%$ versus $\varepsilon_{\text{LG}} \approx 32\,\%$). As the overall uncertainty of this measurement is about ± 0.5 for all tortuosity values, we use $\tau_{\text{SG}} = 3.7$ for SG electrodes – as the mesh has to be passed by lithium-ions – and $\tau_{\text{LG}} = 4.9$ for LG electrodes as the medium value for subsequent studies. Both electrodes' tortuosities are in the range of tortuosities as demonstrated by Landesfeind et al.[170] for commercial electrodes.

Disks with 15 mm in diameter were punched out for both electrodes and resulted in a capacity of 1.20 mAh and 2.48 mAh per layer, respectively. All properties comparing both electrode disks are listed in Table 4.1.

Table 4.1: Properties of electrode disks from SG and LG. All values are measured or consequently calculated.

	SG	LG
Material properties		
D10 value	0.9 µm	7 µm
D50 value	2.3 µm	19 µm
D90 value	5.7 µm	47 µm
Mesh thickness	9 µm (MC33)	24 µm (Microgrid Cu25)
Electrode properties		
Coating thickness	70 µm	60 µm
Resulting thickness	42.5 ± 1 µm	44 ± 1 µm
Porosity	79 ± 2 %	32 ± 2 %
Tortuosity	3.7 ± 0.5	4.9 ± 0.5
Graphite loading	$1.82\,\text{mg/cm}^2$	$4.13\,\text{mg/cm}^2$
Capacity per disk	1.20 mAh	2.48 mAh

Assembly and formation of MLC Each electrode disk was contacted with a strip of copper mesh beneath it. On top of each disk a 25 µm thick Celgard 2325 separator with 19 mm in diameter was placed and 40 µl of LP57 electrolyte ($1\,\text{M LiPF}_6$ in 3:7 EC:EMC; *BASF*) were added. After repeating this step for the other two electrode disks, a 260 µm glass fiber separator was used as an electrolyte reservoir prior to the lithium-metal (*Rockwood Lithium*) counter electrode. With this setup, a stack thickness of 467 µm (from lowest current collector to top of topmost separator) with 132 µm of active electrode was achieved.

The formation of the MLC was performed while the graphite layers were short-circuited with a current of 0.37 mA corresponding to a theoretical C/20 rate on a VMP3 potentiostat. Prior to the formation procedure, the cell was put to rest in a 25 °C temperature chamber for 10 h to guarantee complete

soaking of separators and electrodes with electrolyte. The cell was cycled with a CCCV procedure for
2.5 cycles, ending with a voltage phase at 50 mV for 96 h to achieve full lithiation of all three layers.

4.2.2 Measurement protocol

As already introduced in Figure 4.3, each layer can be operated and measured independently due to
the usage of a separate potentiostat channel for each layer. A master channel operates the lithium
electrode versus the graphite layers and represents a typical half-cell setup which is, therefore, called
complete cell. Please be aware that a charge in a half-cell setup of lithium and graphite means a
delithiation of graphite, since graphite acts as the cathode in this setup. A delithiation of graphite
in a commercial lithium-ion cell with lithium transition-metal oxide or lithium iron phosphate as a
cathode, by contrast, corresponds to a discharge of the cell, since graphite acts as the anode. The
single channels used for the graphite layers are called slave channels, since they are only operated in
an observer mode and all driving currents are provided by the master channel. By a time controlled
measurement protocol, the slave and master channels switch between an open-circuit mode (OCV) and
a chronoamperometry mode (CA), the latter basically corresponding to a short-circuit of the chosen
channel with passed charge recording.

Starting from the fully lithiated state at the end of the formation process, the graphite electrodes were
delithiated via the master channel with the slave channels in CA mode which means that all graphite
electrode layers are on the same potential. The drawn current was 0.75 mA (corresponds to C/10) in
the case of LG electrodes, resulting in a charge of the cell of 1.5 mAh when the current was applied
for 2 h. For SG electrodes the C/10 current was 0.36 mA. The charging time was varied to investigate
different states of delithiation.

After the charging step, the slaves switched to OCV mode for 6 h, separating the three layers from each
other. The simultaneous short-circuiting of the master channel enabled a potential measurement of
each layer versus lithium (refer to Figure 4.3 (b)) and potential relaxation for each layer was recorded.

In a next step, for equilibrating the individual layers, the three slave channels were short-circuited for
29 min and OCV measured for 1 min afterward. The master channel was operated in reverse (29 min
OCV and short-circuited for 1 min) to the slaves during that time so that a potential measurement
versus the lithium electrode was possible after each equilibration step. This allowed electrons to move
from one graphite layer to another to compensate a possible lithium-ion exchange between the layers
during the 29 min time slot. The equilibration regime was repeated for up to 191 times to identify
when the layers are equilibrated. This lead to a total equilibration time between the electrodes of 96 h.

4.3 Long-term equalization effects in lithium-ion batteries due to local state of charge inhomogeneities and their impact on impedance measurements

This section introduces the paper *Long-term equalization effects in Li-ion batteries due to local state
of charge inhomogeneities and their impact on impedance measurements*. We considered EIS mea-
surements a promising candidate to determine the quality of the formation in an end-of-line testing
scenario as EIS is a commonly used method for state estimation. There are several publications

dealing with the sensitivity of EIS regarding inner states, i.e. SOC,[158,162,206–208] SOH[137,159,162,208–214] and cell temperature.[158,162,215–217] Additionally, SEI identification has been a focus of electrochemical impedance investigations.[31,58,129,160,218]

Besides the sensitivities toward the mentioned state variables, a dependency of the previous system excitation by an SOC change on cell impedance is detectable.[158,162,216,219,220] Some of the above cited studies acknowledge that effect by adding a pause step between the last SOC change and the EIS measurement. The assumed durations of the relaxation time (also referred to as equilibration time) differ significantly in literature. In references[31,211,213,214,221] a relaxation time of less than or equal to 1 h was applied. Moreover, practices of 1.5 h,[162] 2 h,[158,207,216] 12 h,[222] 15 h[210] and 24 h[223] are presented. Others[159,206,208,209,212,215,217,224] did not explicitly consider or mention relaxation. The choice of relaxation time is not discussed in any of the above listed papers, nor is any explanation presented for relaxation phenomena. Accordingly, the effect of system excitation on cell impedance was not sufficiently investigated.[158] On the other hand there are some publications dealing with the relaxation of cell potential in more detail,[199,225–228] however, those articles do not include a discussion of the impedance effect which is part of the following paper. Barai et al.[219] studied impedance relaxation phenomena with fixed SOC as well as temperature conditions and pointed out that after a relaxation period of 4 h the influence of previous operation history on the measured impedance is negligible. The authors assumed that the impedance relaxation is due to the relaxation of ions in the double layer capacity and the redistribution of the concentration gradient in the electrolyte and the solid state.

In this paper we investigated five different cell types. A 300 mAh commercial pouch cell was utilized for testing temperature and SOC dependencies on impedance relaxation. Subsequently, when looking at the influence of the cathode chemistry, four different types of round cells with a capacity of about 2 Ah were chosen for reasons of comparability. Three cells of each type were taken into account.

We found that the time to reach a relaxed state for phenomena represented in the low frequency range of an impedance measurement depends strongly on temperature and SOC. For comparing different cells – with the same or different cathode chemistry – it has to be ensured that the cells are in a relaxed state or that only frequency ranges (higher $\sim 500\,\mathrm{Hz}$) are considered that are time-independent.

To explain the observed relaxation in impedance measurements, a hypothesis of three solid phase lithium-ion redistribution effects, one intra-particle (I) and two inter-particle (normal to surface (II) and transverse through electrode (III)), is introduced. A representation of the equilibration pathways for the lithium-ions is depicted in Figure 4.5. To check for validity, a P2D model to simulate the interdependencies of effects (I) and (II) is set up. As calculated by the model, liquid phase gradients are already subsided after 60 s whereas solid phase effects are in the order of hours. Effect (I) is dominant during the beginning of the relaxation process and is later replaced by effect (II) which is probably dominated by the flat open-circuit potential of graphite. The smaller time scales in the model results compared to the measurements can be attributed to the missing implementation of effect (III) transverse through the electrodes.

The paper thereby shows that EIS measurements can be used as a qualitative measurement technique to determine whether equilibration processes in a full cell are completed.

Author contribution While suggesting the experiment and setting up an automatic measurement protocol was my contribution to the paper, the experiments were run and processed together with Andreas Noel who implemented an analyzing script. The hypothesis of the three equilibration processes
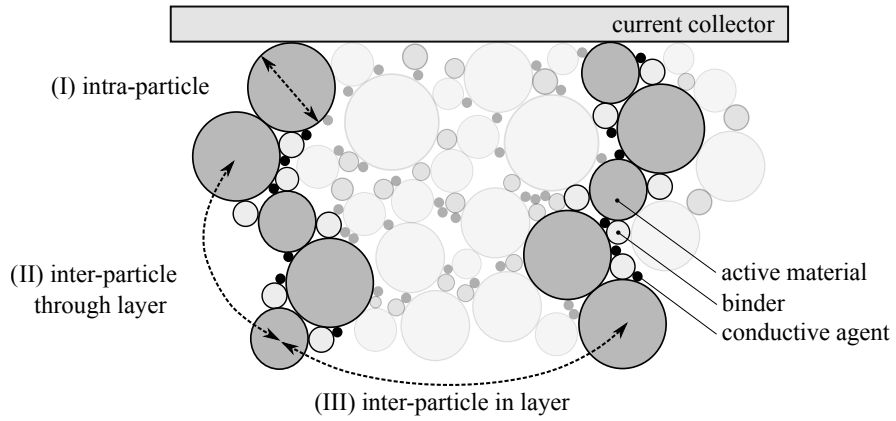
Figure 4.5: Schematic section of a porous electrode consisting of active material, binder and conductive
agent. Three possible ways of lithium-ion movement within relaxation are considered: First,
the assimilation of local lithium-ion concentration gradients within a particle (I), second,
the lithium-ion movement either in liquid or solid phase through the electrode layer (II),
and third, the relaxation laterally along the electrode layer (III).

was developed in collaboration with Simon V. Erhard who set up the P2D model.

Long-term equalization effects in Li-ion batteries due to local state of charge inhomogeneities and their impact on impedance measurements

Frank M. Kindermann, Andreas Noel, Simon V. Erhard, Andreas Jossen
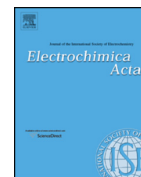
Long-term equalization effects in Li-ion batteries due to local state of charge inhomogeneities and their impact on impedance measurements

Frank M. Kindermann[*], Andreas Noel, Simon V. Erhard, Andreas Jossen

Institute for Electrical Energy Storage Technology, Technische Universität München, Arcisstr. 21, 80333 München, Germany

ABSTRACT

Electrochemical impedance spectroscopy (EIS) is a powerful technique for characterizing Li-ion batteries. Besides the well-known state variables such as state of charge (SOC), state of health (SOH) and temperature, relaxation time after previous conditioning has a crucial impact on EIS measurements. By showing the EIS dependencies of three different temperatures, five SOCs and five cells with different cathode chemistries towards relaxation behavior, the importance of acknowledging relaxation time as an inner state is emphasized. After a single 1C cycle a deviation in the spectra compared to the relaxed state is detectable for up to 40 hours.

In order to explain relaxation behavior, a mind model is introduced, which accounts for three equalization effects inside a particle and through an electrode layer. By means of a 1-D Newman model implemented in COMSOL Multiphysics 4.3b, two of the three proposed effects are discussed in more detail. Qualitatively, simulation data show the same dependencies towards relaxation as the experimental data, indicating that the model is a proper tool to investigate processes inside a cell. Certain deviations between experimental and modeling data can be explained by the 1-D approach and the fact that wiring and cell connections are not accounted for in the model. Modeling results strongly indicate that relaxation processes mainly take place in the graphite anode, which is assumed to be due to the flat open-circuit potential of graphite.

© 2015 Elsevier Ltd. All rights reserved.

1. Introduction

The performance of Li-ion batteries is directly linked to their operating conditions. Thus, an accurate identification of the inner states, such as state of charge (SOC), state of health (SOH) and cell temperature, is elementary for an improvement of battery performance. A commonly used method for state estimation is electrochemical impedance spectroscopy (EIS). There are several publications dealing with the sensitivity of EIS regarding SOC [1–5], SOH [4–14] and cell temperature [3,4,15–17]. Besides the sensitivities towards the mentioned state variables a dependency of the previous system excitation by a SOC change on cell impedance is detectable [3,4,15,18,19]. Some of the above cited studies acknowledge that effect by adding a pause step between the last SOC change and the EIS measurement. The assumed durations of the relaxation time (also referred to as equilibration time) differ significantly in literature. In references [12–14,20,21] a

relaxation time of less than or equal to 1 h was applied. Moreover, practices of 1.5 h [4], 2 h [2,3,15], 12 h [22], 15 h [10] and 24 h [23] are presented. Others [1,5–9,16,17] did not explicitly consider or mention relaxation. The choice of relaxation time is not discussed in any of the above listed papers, nor is any explanation presented for relaxation phenomena. Accordingly, the effect of system excitation on cell impedance is not sufficiently investigated [3]. On the other hand there are some publications dealing with the relaxation of cell potential in more detail [24–28], however, those articles do not include a discussion of the impedance effect which is part of this paper. Barai et al. [18] studied impedance relaxation phenomena with fixed SOC as well as temperature conditions and pointed out that after a relaxation period of 4 h the influence of previous operation history on the measured impedance is negligible. The authors assumed that the impedance relaxation is due to the relaxation of ions in the double layer capacity and the redistribution of the concentration gradient in the electrolyte and the solid state.

Fig. 1 shows EIS measurements during the relaxation process of a Li-ion cell. The testing conditions were kept similar to the measurements of Barai et al. [18]. The drift of cell impedance is still

* Corresponding author.
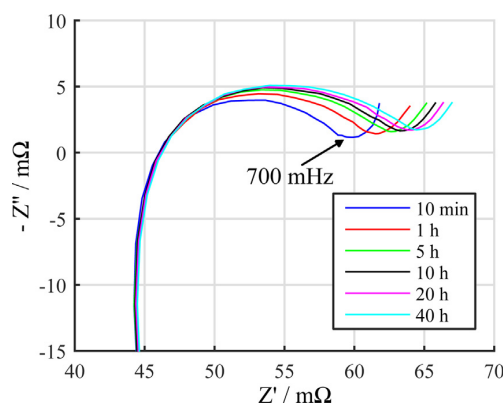*E-mail address:* f.kindermann@tum.de (F.M. Kindermann).

Fig. 1. EIS measurements in Nyquist depiction of *Samsung* cell A at 25 °C and 50 % SOC after increasing relaxation times.

noticeable after a relaxation time of more than 10 h (for more measurement details see section 2). Thus, the dependency of relaxation time on cell impedance is obviously underestimated. Moreover, the influence of SOC and cell temperature on impedance relaxation as well as an evaluation of the proposed transport mechanisms regarding their contribution to the relaxation effect were left open by Barai et al. [18]. In order to address these issues an experimental screening with commercial Li-ion batteries including the cathode chemistries lithium-nickel-manganese-cobalt-oxide (NMC), lithium-manganese-based blend (LiMn), and lithium-iron-phosphate (LFP) was executed. The experiment also considered a SOC and temperature variation.

In section 2 the experimental setup, the method for data analysis and the results will be presented. Respecting the experimental results a mind model was developed, which proposes different long-term transport mechanisms in the solid state domain as an explanation for the relaxation phenomena. The theoretical examination of the proposed mind model will be given in section 3 by presenting a 1-D numerical simulation model, which is derived from the publications of Doyle, Fuller and Newman [29–31]. The paper concludes with a discussion of the measured impedance relaxation respecting the presented Li-ion redistribution processes from the modeling part in section 4.

2. Experimental

2.1. Setup

For the performed tests five different cell types were used. A 300 mAh commercial pouch cell from *Hellpower Industries* was utilized for testing temperature and SOC dependencies on impedance relaxation. Subsequently, when looking at the influence of the cathode chemistry, four different types of round cells with a capacity of about 2 Ah were chosen for reasons of comparability. All considered cell types and their corresponding

properties are summarized in Table 1. Three cells of each type were taken into account.

Cycling and impedance measurements were carried out with a VMP3 potentiostat from *Bio-Logic SAS* in a temperature chamber. The temperature was set prior to all charge changing actions for at least 1 h to give the cells enough time to adapt to a temperature change. Previous to all EIS measurements all cells were charged with a 1C-rate to the maximum potential given by the manufacturer in a CC-CV charging mode (CV terminated after 1 h). After a pause of 15 min the cells were discharged with 1C to their respective minimum potential which was also kept for an hour or terminated when the remaining current dropped beneath C/100 (i.e. CC-CV mode). Before charging again with the same parameters as before, another pause of 15 min was kept. This charging step was followed by a 1 h pause and at last the cells were discharged with 1C to their intended SOC by ampere-hour counting.

Following the SOC setting of the cell, impedances were measured over a time of 48 hours, starting with every 10 min for the first hour, then every 30 min for the next two hours and finally every hour for the remaining time. Since no change in cell potential was observed after 4 to 5 h, self-discharge or side reactions are not considered to be of significant influence.

Each impedance measurement was succeeded by an open-circuit potential phase. The tested frequencies were 10 kHz to 70 mHz with 6 points per decade and 3 sine waves per frequency (only 2 for frequencies lower than 700 mHz). Measurements were carried out in galvanic mode (current excitation and potential response) with a 50 mA amplitude, which was small compared to the capacities of the tested cells, and no DC offset. The resulting measurement time of about 120 seconds was short compared to the overall relaxation time. With the small excitation amplitude and the short perturbation time, the requirement of stationary conditions was fulfilled [32]. An example for measured impedances at increasing relaxation time is shown in Fig. 1 in Nyquist depiction.

Besides the influences of the cathode chemistry, five SOC levels (10, 30, 50, 70 and 90 %) were tested with every mentioned cell. The temperature dependency of 10, 25 and 40 °C was only measured with *Hellpower Industries* cells. All considered tests are shown in Table 2 with their respective parameters and cells.

By looking at the impedance development over time of an exemplary cell in a Bode plot (see Fig. 2(a)), it is obvious that the

Table 2
Overview of tested parameters on respective cells.

Temperature	10 °C					25 °C					40 °C				
SOC in %	10	30	50	70	90	10	30	50	70	90	10	30	50	70	90
Hellpower Industries	x	x	x	x	x	x	x	x	x	x	x	x	x	x	x
Efest						x	x	x	x	x					
Sony						x	x	x	x	x					
Samsung						x	x	x	x	x					
A123 Systems						x	x	x	x	x					

Table 1
Overview of considered cell types and their respective properties.

| Manufacturer	Identifier	Format	Cathode Chemistry*	Capacity in mAh	Discharge Rate (max.)	Voltage range
Hellpower Industries	3.7 V/300 mAh	Pouch	LiMn	300	10C	2.50–4.20 V
Efest	18650 2000 mAh	18650	LiMn	2000	10C	3.00–4.20 V
Sony	US18650V3	18650	NMC	2250	4C	2.50–4.20 V
Samsung	ICR18650-22F	18650	NMC	2200	2C	2.75–4.20 V
A123 Systems	ANR26650 M1A	26650	LFP	2300	30C	2.00–3.60 V

*   as stated by the manufacturer.
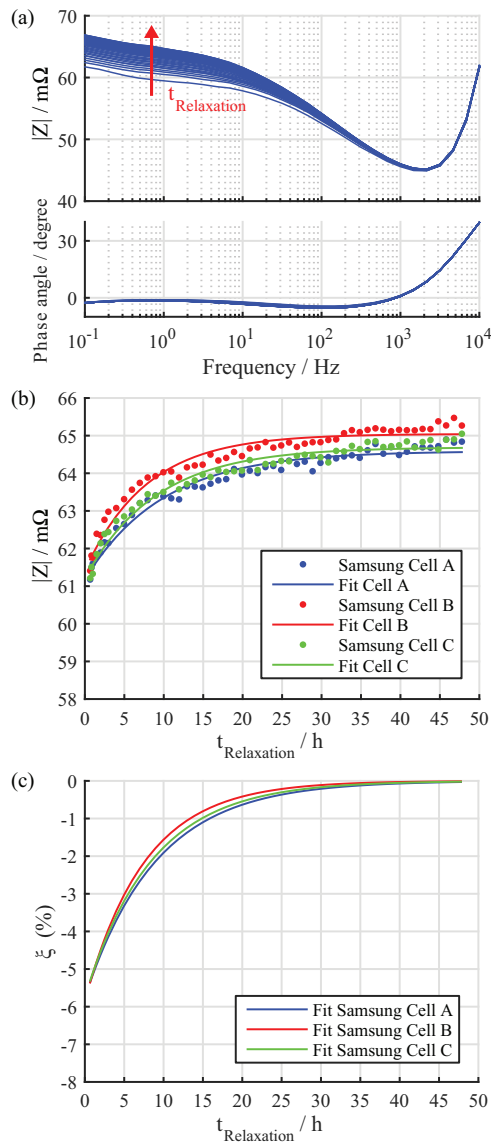
Fig. 2. Impedance development over time of an exemplary cell (*Samsung* cell A) at 50 % SOC and 25 °C in Bode plot (a). The change of the 700 mHz measuring point over recorded relaxation time with fitted exponential function in absolute values (b) becomes almost the same when looking at deviation ξ from relaxed state over time (c).

growth in absolute value of the impedance is almost non-existent in high frequency areas and reaches its maximum at a frequency of lower or equal to 1 Hz. The phase curve in contrast does not change significantly over time, independent of the frequency.

For better comparison of the results and also illustration of the maximum development over time, only the change of the 700 mHz measuring point over the recorded relaxation time of 48 h will be depicted. By fitting a single exponential function to the measured data, the trend of relaxation is easier to grasp. Both, measured data and fitted function, are pictured in Fig. 2(b). The considered frequency of 700 mHz corresponds to a point in the area of a Nyquist plot that is attributed to the charge transfer of a battery cell [18].

Although using cells from one ordering batch and choosing cells with equal measured capacities, a difference in the absolute values of the corresponding impedances could be detected. Therefore, by scaling the measured data to the respective final relaxed value, a deviation ξ from relaxed state over the relaxation period was depicted.

$$\xi = \frac{|Z_t| - |Z_\infty|}{|Z_\infty|} \tag{1}$$

This deviation, in contrast to absolute values, turned out to be very similar for all cells of one batch (compare Fig. 2(b) and (c)).

2.2. Chemistry dependency

One of the executed tests focused on the influence of "chemistry" of the cell on relaxation characteristics. Since commercially available cells were used in the test and cells were not opened, only the approximate composition of the cathode as stated by the manufacturer can be given as the chemistry of the cell. As given in Table 1 cells from *A123 Systems* are made of LFP, *Hellpower Industries* and *Efest* cells of LiMn and *Sony* and *Samsung* cells of NMC. All anodes were stated to be made of carbon without giving further details. Since the composition of the anode, e.g. electrode porosity, particle size (distribution) and thickness of the electrode, is believed to contribute decisively to relaxation, not knowing the morphology of the cells' anodes initially is a drawback. With an experimental setup of commercially available cells it is not possible to elude this without opening the cells. Despite this drawback, Fig. 3(a) reveals that all cells – independent of the chemistry – show the same characteristics in their relaxation behavior (convergence towards relaxed state) and that a certain similarity of the behavior can be observed between cells that are assumed to contain the same chemistry.

LFP reaches its relaxed state faster than the metal oxides (1 % deviation mark after 4 h compared to about 12 to 18 h). The fast relaxation of LFP is probably due to the ultra-high-power dimensioning of the *A123 Systems* cell which are designed to deliver a current up to 30C continuous whereas the other cells are designed for 10C and less. Still, also within the metal oxide cells, NMC containing cells relax slightly faster than the ones comprised of LiMn. A distinction of the contributions from anode and cathode towards relaxation behavior will be drawn in chapter 4.

In measurements comparing different cells via impedance measurements, it is suggested to take these different relaxation times into account. Otherwise one might compare cells in different relaxation states.

2.3. State of charge dependency

Another inner parameter tested with regard to relaxation time was SOC at SOC-levels of 10, 30, 50, 70 and 90 %. Fig. 3(b) depicts that cells at higher SOC relax faster than at lower SOC with *Samsung* cells as an example. The derivable dependency of relaxation time and SOC is nonlinear but monotonically increasing with decreasing SOC. This behavior was detected for most cells and their measured states whereas some cases showed local anomalies for relaxation time over SOC similar to anomalies in decreasing impedances over the SOC as mentioned by [2,3].

2.4. Temperature dependency

The temperature dependency of relaxation time was tested with *Hellpower Industries* cells. Tested temperatures were 10, 25 and 40 °C which were well within defined operating conditions. Fig. 3(c) and (d) show the deviation at the mentioned temperatures for 70 %
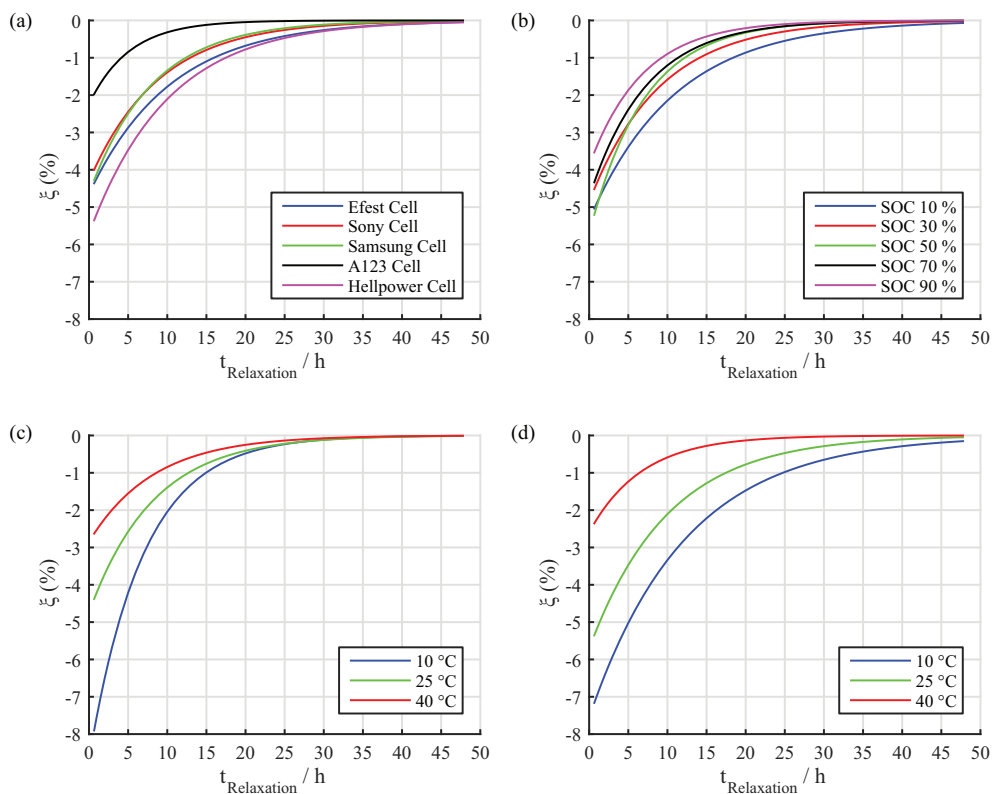
Fig. 3. Chemistry dependency on relaxation time at 25 °C and 70 % SOC (a). SOC dependency on relaxation time at 25 °C (b) with *Samsung* cell. Temperature dependency on relaxation time at 70 (c) and 30 % SOC (d) with *Hellpower Industries* cell. All graphs show the respective 700 mHz value.

and 30 % SOC respectively. As can be seen, relaxation takes the longest at 10 °C and, in agreement with SOC dependency, takes longer at a SOC of 30 % than at 70 %. At 10 °C and 30 % SOC the depicted cell is not fully relaxed during the 48 hour waiting period which is apparent in the still existing deviation at 48 h. This temperature dependence behaves as expected with faster kinetics which support a faster equalization process at higher temperatures.

2.5. Derived mind model of relaxation effects

Impedance relaxation could be observed for an unexpectedly long time, so a mind model was developed to explain those long-time effects. Although cell potential relaxation could not be observed for more than 4 to 5 h, after that time there might still be local polarization in the particles which is not visible in the cell
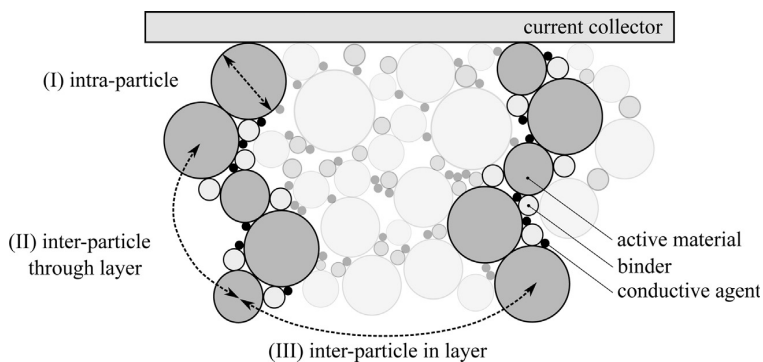
Fig. 4. Schematic section of a porous electrode consisting of active material, binder and conductive agent. Three possible ways of Li-ion movement within relaxation are considered: First, the assimilation of local Li-ion concentration gradients within a particle (I), second, the Li-ion movement either in liquid or solid phase through the electrode layer (II), and third, the relaxation laterally along the electrode layer (III).

potential measured at the battery's terminals. Since liquid diffusivity in common electrolytes is about $10^{-10}\,\text{m}^2\,\text{s}^{-1}$ [33], whereas active materials such as graphite or NMC show much slower diffusivities in the range of 10^{-14} to $10^{-16}\,\text{m}^2\,\text{s}^{-1}$ [34–36], it is expected that the solid phase is responsible for those long relaxation times. Even if the pathway of liquid diffusion (inside the electrode) is longer than that of solid diffusion (within the particles), the difference of more than 4 orders of magnitude highlights the larger impact of solid-state diffusion. Therefore, three effects in the solid phase – associated with relaxation – are proposed and are presented in Fig. 4. The first effect (I) is an intra-particle assimilation process of Li-ions which decreases concentration gradients inside a particle (high concentration near the surface and low concentration in the bulk or vice versa) caused by slow solid-state diffusion during charge or discharge. The other two effects both occur between different particles and are therefore called "inter-particle". Effect (II) is due to a SOC gradient perpendicular through the electrode. Klink et al. showed this effect with a segmented electrode and were able to see changes in SOC assimilation currents through the electrode for two hours even when a fixed potential was applied to speed up the process [37]. In case (II) there are two possible means of transport. One is Li-ion diffusion within the solid phase, the other could be a charge transfer and mass transport in the liquid phase. The transport in the liquid phase is expected to be dominant, since effective diffusion is faster in the liquid than the solid phase. At last, effect (III) is an inter-particle transport transverse through the electrode. Especially in wound 18650 and 26650 cells with few tabs and electrodes between 0.5 m and 1.5 m in length this effect could lead to very long relaxation times since inhomogeneities are spread over a great length in the electrode. For this effect it is likely that diffusion of Li-ions will happen in the liquid phase and electrons travel through the respective current collector.

3. Physico-chemical Model Setup

For the model setup, the well-known approach by Newman and co-workers [29–31] which addresses liquid potentials and porous electrodes is adopted and implemented in the commercial software COMSOL Multiphysics 4.3b. Usually, this model is solved within time domain but here a coupled analysis within time and frequency domain is established. Thus, impedance relaxation, which is a strongly interdepending phenomenon, can be simulated by this framework. Within time domain a backward differential formula (BDF) is set. After solving time steps, the results are handed over as an initial value set to a frequency solver which allows calculation of complex impedance by a harmonic perturbation at the model's boundary. After that, the time stepping continues where any number of additional spectra can be processed at desired time steps.

The model geometry is defined as a one dimensional interval divided into three parts corresponding to the negative electrode, the separator and the positive electrode domain. An additional dimension is set for the description of species intercalation within the particle domain. For a detailed model description, the reader is referred to [30,31,38]. The main equations are mass balance for Li-ion concentration in the electrolyte c_l

$$\varepsilon_l \frac{\partial c_l}{\partial t} = -\nabla\left(-D_{l,eff}\nabla c_l + \frac{\mathbf{i}_l t_+}{F}\right) + a_s j_n \tag{2}$$

and charge balance

$$\nabla\left(-\kappa_{eff}\nabla\varphi_l + \frac{2\kappa_{eff}RT}{F}\left(1 + \frac{\text{dln}f_\pm}{\text{dln}c_l}\right)(1-t_+)\nabla\text{ln}c_l\right)$$
$$= Fa_s j_n + i_{dl} \tag{3}$$

throughout the electrode domain. The current within liquid phase is described by current density $\mathbf{i}_l$ and potential φ_l, while the pore wall flux at the electrode-electrolyte interface is named j_n. R describes the gas constant, F the Faraday's constant and T the local temperature which is kept constant in this case. Within the separator domain the equations simplify to

$$\varepsilon_l \frac{\partial c_l}{\partial t} = -\nabla\left(-D_{l,eff}\nabla c_l + \frac{\mathbf{i}_l t_+}{F}\right) \tag{4}$$

and

$$\nabla\left(-\kappa_{eff}\nabla\varphi_l + \frac{2\kappa_{eff}RT}{F}\left(1 + \frac{\text{dln}f_\pm}{\text{dln}c_l}\right)(1-t_+)\nabla\text{ln}c_l\right) = 0 \tag{5}$$

To couple solid and liquid phase, Butler-Volmer kinetics are assumed for the pore wall flux

$$j_n = (k_c)^{\alpha_a}(k_a)^{\alpha_c}(c_{s,max,pos/neg} - c_s)^{\alpha_a}(c_s)^{\alpha_c}\left(\frac{c_l}{c_{l,ref}}\right)^{\alpha_a}\left[exp\left(\frac{\alpha_a F\eta}{RT}\right) - exp\left(-\frac{\alpha_c F\eta}{RT}\right)\right] \tag{6}$$

including the Li-ion concentration at the particle's surface c_s and the overpotential

$$\eta = \varphi_s - \varphi_l - E_{pos/neg} \tag{7}$$

where φ_s corresponds to the solid phase potential.

All transport parameters are scaled by Bruggeman's expression [39]

$$\Psi_{eff} = \Psi_0\left(\varepsilon_{s/l}\right)^{1.5} \tag{8}$$

and to describe electrolyte characteristics properly, a concentration dependence is implemented for conductivity, diffusivity and activity [33]. Additionally, a double-layer capacity is assumed to represent impedance behavior correctly. It is set as a specific capacity which is charged or discharged corresponding to the potential drop across the double layer

$$i_{dl} = a_s C_{dl,pos/neg}\left(\frac{\partial\varphi_s}{\partial t} - \frac{\partial\varphi_l}{\partial t}\right) \tag{9}$$

The chosen parameters represent a common NMC/graphite cell with medium sized electrode layers as well as an anode oversizing and are summarized in Table 3. Diffusion coefficients are values estimated from various literature sources [34–36,40,41]. Conductivity, diffusivity and mean molar activity coefficient of the electrolyte are taken from fittings of measurements [33] while presuming a constant transport number. The porosity and active material fractions are estimated to represent a parameter range of common Li-ion cells which usually have porosities of about 30 % [25,36] and active material volume fraction between 40 and 60 % [25,30,35,42]. The equilibrium potentials are taken from literature [36,40] as well as the maximum concentration of lithium within active material particles [40,43]. Additional parameters such as reaction rate constants [36,40] and specific double layer values [44] are assumed based on references from literature.

The frequency analysis of the model reveals certain limitations when high frequencies are considered. Usually, impedance spectra of Li-ion cells feature a region representing a low-frequency, a mid-frequency and a high-frequency domain. The first is connected to a diffusive section whereas the second is interpreted as a charge-transfer and surface layer diffusion section. The third, at the intersection with the real part axis, is considered purely ohmic and an inductive domain is in the positive imaginary half-plane. The presented model is not capable of showing the intersection with the real part axis and inductive parts in a Nyquist plot due to strictly capacitive behavior. Since this study is focusing on

Table 3
Model parameters representing a common NMC/graphite cell.

Parameter	Value	Source
Geometry		
Cathode layer thickness t_{pos}	50 μm	s
Anode layer thickness t_{neg}	60 μm	s
Separator thickness t_{sep}	20 μm	s
Volume fraction of solid phase $\varepsilon_{s,pos}$	0.5	a [25,30,35,36,42]
Volume fraction of solid phase $\varepsilon_{s,neg}$	0.6	a [25,30,35,36,42]
Volume fraction of electrolyte $\varepsilon_{l,pos}$	0.3	a [25,30,35,36,42]
Volume fraction of electrolyte $\varepsilon_{l,neg}$	0.3	a [25,30,35,36,42]
Volume fraction of electrolyte in separator $\varepsilon_{l,sep}$	0.5	s
Particle radius $r_{p,pos}$	4 μm	s
Particle radius $r_{p,neg}$	12 μm	s
Maximum concentration $c_{s,max,pos}$	51000 mol/m^3	a [43]
Maximum concentration $c_{s,max,neg}$	31370 mol/m^3	a [40]
Specific surface area a_s	$3\frac{\varepsilon_s}{r_p}$	s
Kinetics		
Equilibrium potential E_{pos}	$E_{pos}(y) = 6.0826 - 6.9922y + 7.1062y^2 - 0.54549 \times 10^{-4}\exp(124.23y - 114.2593) - 2.5947y^3$	[36]
Equilibrium potential E_{neg}	$E_{neg}(x) = 0.6379 + 0.5416\exp(-305.5309x) + 0.044\tanh\left(-\frac{x - 0.1958}{0.1088}\right) -$	[40]
	$0.1978\tanh\left(\frac{x - 1.0571}{0.0854}\right)0.6875\tanh\left(\frac{x + 0.0117}{0.0529}\right) - 0.0175\tanh\left(\frac{x - 0.5692}{0.0875}\right)$	
Reaction rate constant k_{pos}	$k_c = k_a = 3e - 12 m/s$	a [36]
Reaction rate constant k_{neg}	$k_c = k_a = 3.5e - 12 m/s$	a [40]
Temperature T	298.15 K	s
Transport		
Electronic conductivity $\sigma_{pos,0}$	10 S/m	a [41]
Electronic conductivity $\sigma_{neg,0}$	10 S/m	a [41]
Diffusion coefficient $D_{s,pos}$	1e-15 m^2/s	a [34–36,40,41]
Diffusion coefficient $D_{s,neg}$	5e-14 m^2/s	a [34–36,40,41]
Charge transfer coefficient α_{pos}	$\alpha_c = \alpha_a = 0.5$	s
Charge transfer coefficient α_{neg}	$\alpha_c = \alpha_a = 0.5$	s
Salt diffusivity in electrolyte $D_{l,0}$	$D_{l,0} = 10^{-0.22c_l - 8.43 - \frac{54}{T - 229 - 5c_l}}$	[33]
Ionic conductivity of electrolyte κ_0	$\kappa_0 = \frac{c_l}{10}\left(-10.5 + 0.074T - 6.96 \times 10^{-5}T^2 + 0.668c_l - 0.0178c_lT + 2.8 \times 10^{-5}c_lT^2 + 0.494c_l^2 - 8.86 \times 10^{-4}c_l^2T\right)^2$	[33]
Activity dependency $\left(\frac{d\ln f_{\pm}}{d\ln c_l}\right)$	$\frac{0.601 - 0.24c_l^{0.5} + 0.982(1 - 0.0052(T - 298.15))c_l^{1.5}}{(1 - t_+)} - 1$	[33]
Transference number t_+	0.38	[33]
Double layer properties		
Specific capacity $C_{dl,pos}$	0.1 F/m^2	a [44]
Specific capacity $C_{dl,neg}$	0.1 F/m^2	a [44]

^{a}assumed based on Ref.; ^{s}specified.

frequencies lower than this high frequency range, this limitation has no effect on the results.

4. Simulation Results

Prior to starting model simulations, the initial state for the conducted analyses was a fully charged and relaxed state from where the model was discharged to 3.6 V with 20 A m^{-2} which is approximately equivalent to a 1C-rate. The cell potential corresponds to a mean potential of a NMC/graphite cell that can be cycled in the range of 3.0 to 4.2 V. After that, the boundary is set to zero current and impedance spectra were calculated for different times during relaxation.

4.1. Comparison to Measured Data

When first looking at the calculated impedances in the Nyquist diagram of Fig. 5(a), it is obvious that an increase in the real part (Z') of the low frequency range can be seen as depicted in the measured data in Fig. 1. Additionally, in agreement with the measurement, no changes can be seen in the high frequency range. By depicting the simulated data in a Bode plot, the same dependencies as in measured data also appear. Whereas no change over time is visible in the phase angle data, an expansion can be detected in the absolute value reaching a steady gap at frequencies lower than 1Hz (Fig. 5(b)). Finally, Fig. 5(c) shows the evolution of the 700 mHz point of the absolute value as previously
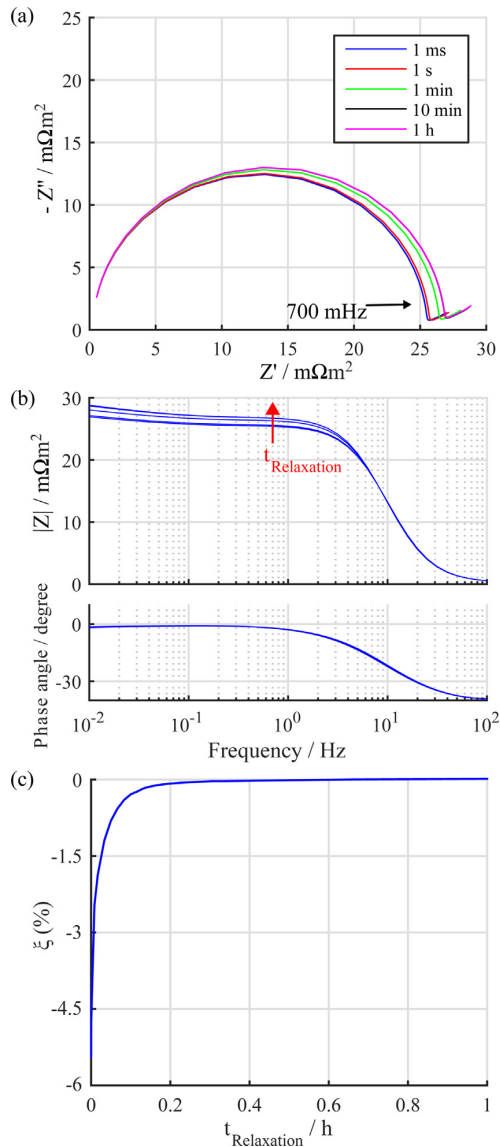
Fig. 5. Results of the simulation show (a) a Nyquist diagram at five time steps after the end of a discharge; (b) the corresponding absolute value and phase angle in a Bode diagram; (c) the absolute impedance at 700 mHz over relaxation time.

done with the measured data. The simulation data also follow an exponential growth, starting from 5 to 6 % deviation (same as measurements), but reach their steady state after a time of approximately 1 h.

In conclusion of this comparison between simulated and measured data, it was shown that the model is capable of describing all measured impedance and cell relaxation effects in the same distinctive way. Compared to measurement data a frequency offset of about one decade can be observed. This offset is probably due to the simplified 1-D representation of the problem and the negligence of internal cell contacting and/or wiring. Absolute values of relaxation time that do not correspond that well also have to be attributed to simplifications and, therefore, limitations of the model. For example, besides the previously mentioned lack of connection implementation, effect (III), the

inter-particle transport transverse through the electrode, cannot be reproduced by a 1-D model. With electrodes being up to 1 m in length in 18650 cells this can very well contribute to much longer relaxation times (compared to 50 to 100 μm through the electrode). At last, in contrast to the measurements the starting point of the model was always a fully charged and fully relaxed state. Although the CV and pause phase in the measurements tried to compensate for that, it is impossible to determine the state of relaxation previously to the discharging process preceding the impedance measurements.

Since all basic dependencies were pointed out, the next section will take a look at effect (I) and (II) and possible distinctions of both.

4.2. Discussion of liquid and solid phase Li-ion concentration

As presented in Table 3 the simulated model cell has an anode thickness of 60 μm and a cathode thickness of 50 μm with a 20 μm separator in between. Fig. 6(a) shows the evolution of Li-ion concentration in those three cell domains at different times after the end of discharge. Due to a comparatively high diffusion coefficient of the electrolyte (about 10^{-10} m^2 s^{-1}), the simulation model shows an assimilation of Li-ion concentration in less than 1 min throughout the electrolyte. Therefore, relaxation has to be attributed to assimilation processes in the solid phase.

By looking at Fig.6(b) and (c) solid phase equalization is observable for 1 h in the cathode (c) and the anode shows concentration gradients even after 3 hours of relaxation (b). The SOC in this presented case is a correlated variable of the current value of Li-ion concentration at particle surface compared to the theoretical maximum Li-ion capacity. Within the anode domain, concentration gradients of up to 2 % occur across the thickness of the anode layer. In contrast to that, the cathode seems to be evenly discharged / charged. The parallel offset evolving over time in Fig. 6(b) and (c) indicates relaxation due to the proposed effect (I), since surface concentration is changing uniformly throughout the electrode. This corresponds to diffusion of Li-ions within the particle domain. A decrease or increase of slope suggests that the concentration of Li-ions is balanced across the electrode domain, by which particles deviating from the electrode's average concentration adapt. The main flux of Li-ions is between particles, as indicated by relaxation effect (II). Within the first 10 min of relaxation, process (I) is dominant. After that time, relaxation process (II) seems to prevail.

Fig. 7 highlights the distinction of relaxation processes within the electrodes. The normalized deviation within a particle is depicted for the anode (a) as well as the cathode (b). This definition of internal balancing can be attributed to relaxation path (I), where Li-ions are re-distributed within a particle. In anode particles the small concentration gradient is negligible after 10 min. Since the chemical potential is the driving force, the re-balancing rate only depends on the diffusivity, which is high in contrast to the cathode, and the diffusion length. Within the cathode domain strong concentration gradients in a particle are established during discharge. Still, the time needed for re-balancing within the particle is almost the same as for anode particles. This can be attributed to smaller particle radii of the cathode material. In general, small particle radii and high diffusivity are preferable for relaxation path (I) which is independent of the open-circuit profile. Within minutes or up to a few hours this process should be finished.

Additionally, a second deviation number is defined. It indicates the deviation of particles towards the average concentration within the electrode in correspondence to relaxation process (II). Thus, the values can also be negative which reflects unevenly discharged regions within the electrode. The anode shows only
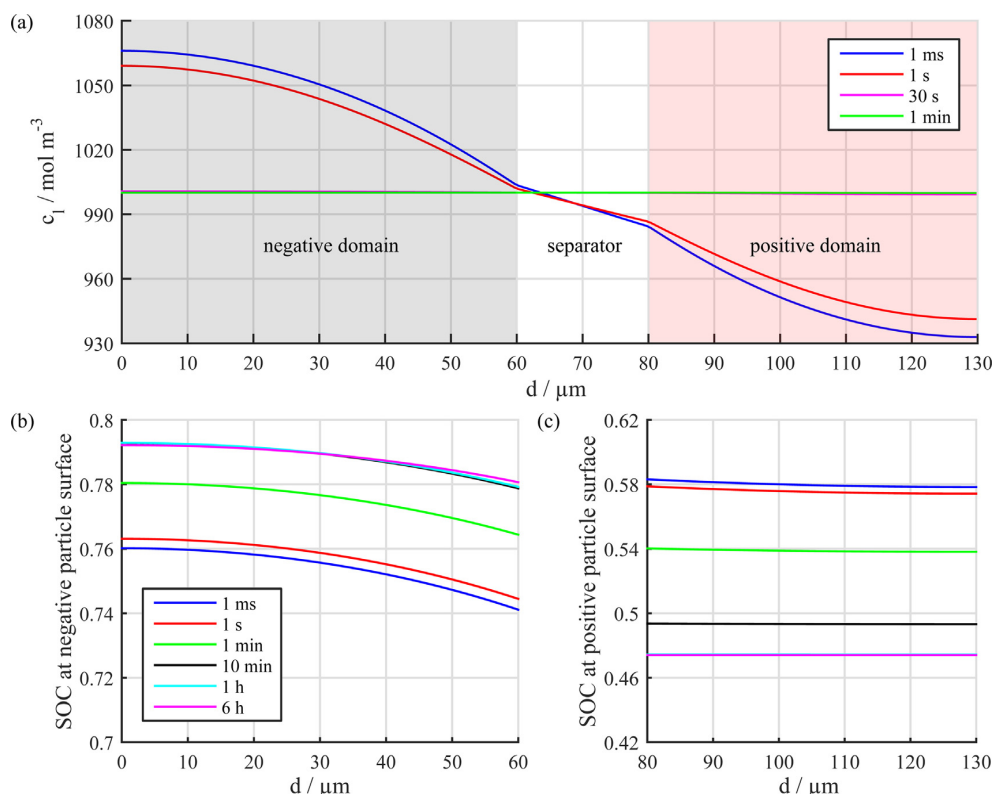
Fig. 6. Simulation results of (a) liquid phase Li-ion concentration throughout cell domain at depicted time steps after discharge; (b) simulated state of charge of negative electrode at particle surface; (c) simulated state of charge of positive electrode at particle surface.

small values of about 0.5 % (see Fig. 7(c)) of inhomogeneity throughout the electrode, but even this small deviation is not equalized within 6 h. Since the potential difference between the particles' surfaces is the driving force for relaxation path (II), this slow equalization could be explained by the flat open-circuit potential of graphite within this state of charge which provides almost no gradient to balance concentration across the electrode [42]. Even after 6 h a visible deviation remains which gives some indication for long-term impedance relaxation of up to 40 h. This assumption is in agreement with Ng et al. [28], who experimentally investigated current density distribution perpendicular through graphite electrodes and showed that equilibration of local Li-ion concentrations is not completed after 15 h of relaxation. In contrast to that, the cathode is balanced within less than 2 h (see Fig. 7(d)). This can be explained by the steeper open-circuit potential profile of NMC throughout the entire state of lithiation in contrast to the flat profile of graphite.

The explanation of the long-term relaxation effects shown in the batteries' impedance is assumed to be connected with the balancing currents in the electrodes. According to Butler-Volmer type kinetics, a differential charge-transfer resistance is increasing as long as the current density is decreasing since the corresponding kinetics curve is not linear. This leads to a macroscopically increase of the cell impedance in the low frequency region. Fig. 8(a) shows a Butler-Volmer kinetics graph with a steady Δj_{ct} at two exemplary bias points at times t_1 and t_2. The potential response to the current excitation during the impedance measurement increases when the

balancing current density decreases. In Fig. 8(b) the effect for an impedance in Nyquist depiction at the two mentioned points is presented.

5. Conclusions

In this paper the dependency of relaxation time as a state variable on EIS measurements was shown. The time to reach a relaxed state for phenomena represented in the low frequency range of an impedance measurement depends strongly on temperature and SOC. For comparing different cells – with the same or different cathode chemistry – it has to be ensured that the cells are in a relaxed state or that only frequency ranges (higher ~500 Hz) are considered that are time-independent. To explain the observed relaxation in impedance measurements a theory of three solid phase Li-ion redistribution effects, one intra-particle ((I)) and two inter-particle (normal to surface (II) and transverse through electrode (III)), was introduced. A model to simulate the interdependencies of effects (I) and (II) was set up. As calculated by the model, liquid phase gradients were already subsided after 60 seconds whereas solid phase effects were in the order of hours. Effect (I) was dominant during the beginning of the relaxation process and was later replaced by effect (II) which is probably dominated by the flat open-circuit potential of graphite. The smaller time scales in the model results compared to the measurements can be attributed to the missing implementation of effect (III) transverse through the electrodes.
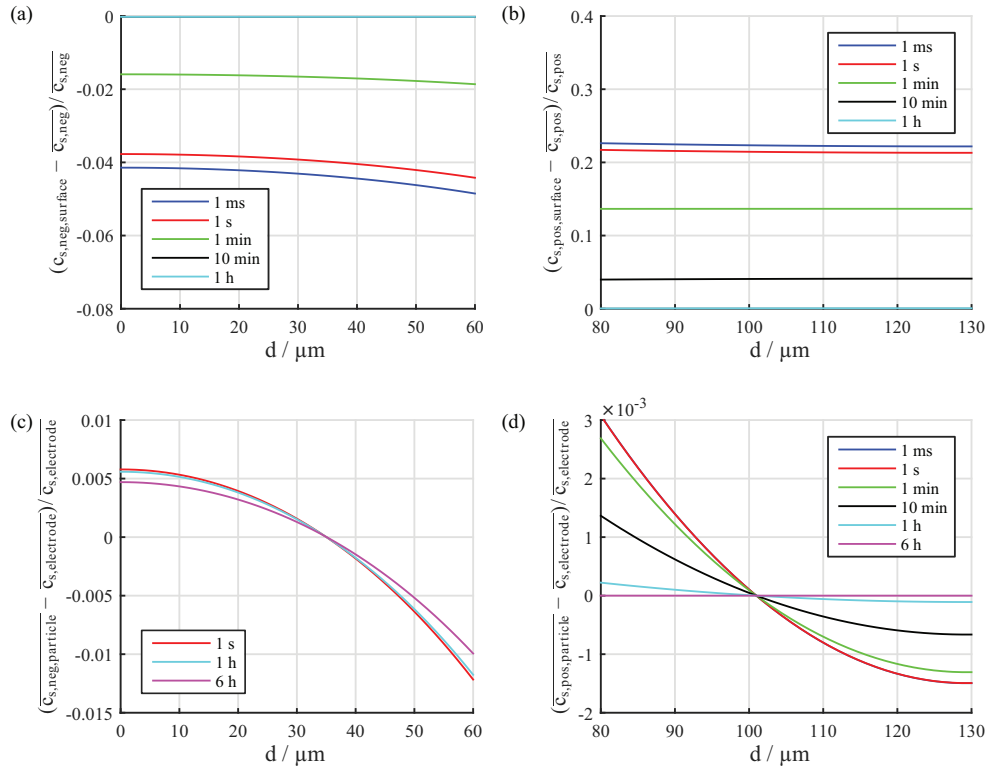
Fig. 7. Simulation results of deviation within a particle from average concentration in anode domain (a) and cathode domain (b) corresponding to relaxation path (I); simulated deviation of a particle from averaged electrode concentration in anode domain (c) and cathode domain (d) corresponding to relaxation path (II). Please note that there is no further change after 10 min (black line exactly underneath the 1 h cyan line) in the anode domain (a).
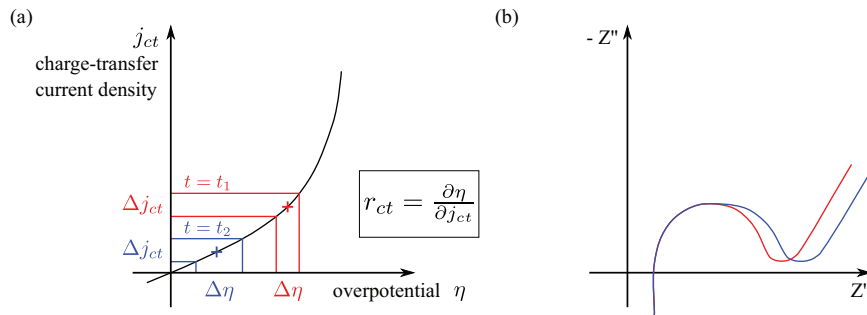

Fig. 8. Exemplary increase of potential response and therefore, increase of charge-transfer resistance during relaxation for two bias points at times t_1 and t_2. Butler-Volmer kinetics are shown in (a) and resulting Nyquist impedance in (b).

The above mentioned anomalies in relaxation time growth with decreasing SOC could also be due to the open-circuit potential of graphite. When setting the SOC, it could not be determined whether the graphite was in one of its plateaus or in a transition zone of the intercalation stages. Those issues have to be addressed in future work.

References

[1] V. Pop, H.J. Bergveld, P.H.L. Notten, P.P.L. Regtien, State-of-the-art of battery state-of-charge determination, Meas. Sci. Technol. 16 (2005) R93–110.
[2] L. Ran, W. Junfeng, W. Haiying, L. Gechen, Prediction of state of charge of Lithium-ion rechargeable battery with electrochemical impedance spectroscopy theory, 5th IEEE Conference on Industrial Electronics and Applications (ICIEA), Taichung, Taiwan, 2010, pp. 684–688.
[3] W. Waag, S. Käbitz, D.U. Sauer, Experimental investigation of the lithium-ion battery impedance characteristic at various conditions and aging states and its influence on the application, Applied Energy 102 (2013) 885–897.

[4] D. Andre, M. Meiler, K. Steiner, C. Wimmer, T. Soczka-Guth, D.U. Sauer, Characterization of high-power lithium-ion batteries by electrochemical impedance spectroscopy. I. Experimental investigation, Journal of Power Sources 196 (2011) 5334–5341.

[5] W. Waag, C. Fleischer, D.U. Sauer, Critical review of the methods for monitoring of lithium-ion batteries in electric and hybrid vehicles, Journal of Power Sources 258 (2014) 321–339.

[6] U. Tröltzsch, O. Kanoun, H.-R. Tränkler, Characterizing aging effects of lithium ion batteries by impedance spectroscopy, Electrochimica Acta 51 (2006) 1664–1672.

[7] J. Shim, Electrochemical analysis for cycle performance and capacity fading of a lithium-ion battery cycled at elevated temperature, Journal of Power Sources 112 (2002) 222–230.

[8] C. Fleischer, W. Waag, H.-M. Heyn, D.U. Sauer, On-line adaptive battery impedance parameter and state estimation considering physical principles in reduced order equivalent circuit battery models part 2. Parameter and state estimation, Journal of Power Sources 262 (2014) 457–482.

[9] M. Ecker, J.B. Gerschler, J. Vogel, S. Käbitz, F. Hust, P. Dechent, D.U. Sauer, Development of a lifetime prediction model for lithium-ion batteries based on extended accelerated aging test data, Journal of Power Sources 215 (2012) 248–257.

[10] Y. Li, M. Bettge, B. Polzin, Y. Zhu, M. Balasubramanian, D.P. Abraham, Understanding Long-Term Cycling Performance of $Li_{1.2}Ni_{0.15}Mn_{0.55}Co_{0.1}O_2$-Graphite Lithium-Ion Cells, J. Electrochem. Soc. 160 (2013) A3006–A3019.

[11] J. Vetter, P. Novák, M.R. Wagner, C. Veit, K.-C. Möller, J.O. Besenhard, M. Winter, M. Wohlfahrt-Mehrens, C. Vogler, A. Hammouche, Ageing mechanisms in lithium-ion batteries, Journal of Power Sources 147 (2005) 269–281.

[12] Y. Zhang, C.-Y. Wang, X. Tang, Cycling degradation of an automotive $LiFePO_4$ lithium-ion battery, Journal of Power Sources 196 (2011) 1513–1520.

[13] Y. Zhang, C.-Y. Wang, Cycle-Life Characterization of Automotive Lithium-Ion Batteries with $LiNiO_2$ Cathode, J. Electrochem. Soc. 156 (2009) A527.

[14] G. Ning, B. Haran, B.N. Popov, Capacity fade study of lithium-ion batteries cycled at high discharge rates, Journal of Power Sources 117 (2003) 160–169.

[15] J.G. Roth, Impedanzspektroskopie als Verfahren zur Alterungsanalyse von Hochleistungs-Lithium-Ionen-Zellen, 1st ed., Verlag Dr. Hut, München, 2013.

[16] J.P. Schmidt, S. Arnold, A. Loges, D. Werner, T. Wetzel, E. Ivers-Tiffée, Measurement of the internal cell temperature via impedance: Evaluation and application of a new method, Journal of Power Sources 243 (2013) 110–117.

[17] H.-M. Cho, W.-S. Choi, J.-Y. Go, S.-E. Bae, H.-C. Shin, A study on time-dependent low temperature power performance of a lithium-ion battery, Journal of Power Sources 198 (2012) 273–280.

[18] A. Barai, G.H. Chouchelamane, Y. Guo, A. McGordon, P. Jennings, A study on the impact of lithium-ion cell relaxation on electrochemical impedance spectroscopy, Journal of Power Sources 280 (2015) 74–80.

[19] F.M. Kindermann, A. Noel, P. Keil, A. Jossen, Influence of Relaxation Time on EIS Measurements of Li-ion Batteries, 6th International Workshop on Impedance Spectroscopy, Chemnitz, 2013.

[20] S.S. Zhang, K. Xu, T.R. Jow, Electrochemical impedance study on the low temperature of Li-ion batteries, Electrochimica Acta 49 (2004) 1057–1061.

[21] X. Zhang, P.N. Ross, R. Kostecki, F. Kong, S. Sloop, J.B. Kerr, K. Striebel, E.J. Cairns, F. McLarnon, Diagnostic Characterization of High Power Lithium-Ion Batteries for Use in Hybrid Electric Vehicles, J. Electrochem. Soc. 148 (2001) A463–A470.

[22] INEEL, PNGV Test Plan for Advanced Technology Development GEN 2 Lithium-ion Cells: EHV-TP-121, 6th ed., 2002.

[23] M. Gaberscek, R. Dominko, J. Jamnik, The meaning of impedance measurements of $LiFePO_4$ cathodes: A linearity study, Journal of Power Sources 174 (2007) 944–948.

[24] D.M. Bernardi, R. Chandrasekaran, J.Y. Go, Solid-state transport of lithium in lithium-ion-battery positive electrodes, J. Electrochem. Soc. 160 (2013) A1430–A1441 8208.

[25] D.M. Bernardi, J.-Y. Go, Analysis of pulse and relaxation behavior in lithium-ion batteries, Journal of Power Sources 196 (2011) 412–427.

[26] L. Pei, T. Wang, R. Lu, C. Zhu, Development of a voltage relaxation model for rapid open-circuit voltage prediction in lithium-ion batteries, Journal of Power Sources 253 (2014) 412–418.

[27] W. Waag, D.U. Sauer, Adaptive estimation of the electromotive force of the lithium-ion battery after current interruption for an accurate state-of-charge and capacity determination, Applied Energy 111 (2013) 416–427.

[28] S.-H. Ng, F. La Mantia, P. Novák, A Multiple Working Electrode for Electrochemical Cells: A Tool for Current Density Distribution Studies, Angew. Chem. Int. Ed. 48 (2009) 528–532.

[29] C.M. Doyle, T.F. Fuller, J.S. Newman, Modeling of Galvanostatic Charge and Discharge of the Lithium/Polymer/Insertion Cell, J. Electrochem. Soc. 140 (1993) 1526–1533.

[30] T.F. Fuller, C.M. Doyle, J.S. Newman, Simulation and Optimization of the Dual Lithium Ion Insertion Cell, J. Electrochem. Soc. 141 (1994) 1–10.

[31] C.M. Doyle, Design and simulation of lithium rechargeable batteries. Ph.D. Thesis, Berkeley, 1995.

[32] G.S. Popkirov, Fast time-resolved electrochemical impedance spectroscopy for investigations under nonstationary conditions, Electrochimica Acta 41 (1996) 1023–1027.

[33] L.O. Valoen, J.N. Reimers, Transport Properties of $LiPF_6$-Based Li-Ion Battery Electrolytes, J. Electrochem. Soc. 152 (2005) A882–A891.

[34] C.X. Ding, Y.C. Bai, X.Y. Feng, C.H. Chen, Improvement of electrochemical properties of layered $LiNi_{1/3}Co_{1/3}Mn_{1/3}O_2$ positive electrode material by zirconium doping, Solid State Ionics 189 (2011) 69–73.

[35] J. Christensen, V. Srinivasan, J.S. Newman, Optimization of Lithium Titanate Electrodes for High-Power Cells, J. Electrochem. Soc. 153 (2006) A560–A565.

[36] S.G. Stewart, V. Srinivasan, J.S. Newman, Modeling the Performance of Lithium-Ion Batteries and Capacitors during Hybrid-Electric-Vehicle Operation, J. Electrochem. Soc. 155 (2008) A664–A671.

[37] S. Klink, W. Schuhmann, F. La Mantia, Vertical Distribution of Overpotentials and Irreversible Charge Losses in Lithium Ion Battery Electrodes, ChemSusChem 7 (2014) 2159–2166.

[38] S. Erhard, F. Spingler, A. Rheinfeld, S. Kosch, K. Rumpf, A. Jossen, Physico-chemical modelling of Li-ion batteries: Parameter analysis in the frequency domain, in: O. Kanoun (Ed.), Lecture notes on impedance spectroscopy, CRC Press, Boca Raton, 2015.

[39] D.A.G. Bruggeman, Berechnung verschiedener physikalischer Konstanten von heterogenen Substanzen. I. Dielektrizitätskonstanten und Leitfähigkeiten der Mischkörper aus isotropen Substanzen, Ann Phys. 416 (1935) 636–664.

[40] M. Safari, C. Delacourt, Modeling of a Commercial Graphite/$LiFePO_4$ Cell, J. Electrochem. Soc. 158 (2011) A562–A571.

[41] X. M. Park, M. Zhang, G.B. Chung, A.M. Sastry Less, A review of conduction phenomena in Li-ion batteries, Journal of Power Sources 195 (2010) 7904–7929.

[42] T.F. Fuller, C.M. Doyle, J.S. Newman, Relaxation Phenomena in Lithium-Ion-Insertion Cells, J. Electrochem. Soc. 141 (1994) 982–990.

[43] S. Tippmann, D. Walper, L. Balboa, B. Spier, W.G. Bessler, Low-temperature charging of lithium-ion cells part I: Electrochemical modeling and experimental investigation of degradation behavior, Journal of Power Sources 252 (2014) 305–316.

[44] S. Brown, N. Mellgren, M. Vynnycky, G. Lindbergh, Impedance as a Tool for Investigating Aging in Lithium-Ion Porous Electrodes: II. Positive Electrode Examination, J. Electrochem. Soc. 155 (2008) A320–A338.

4.4 Measurements of lithium-ion concentration equilibration processes inside graphite electrodes

Based on our previous work on impedance relaxation phenomena, we conducted experiments with a laboratory cell developed and introduced by Klink et al.[200] to prove our hypothesis of relaxation processes. A thorough introduction of the cell and the measurement protocol was given in Section 4.2.

In this work, we presented a way to measure equilibration processes caused by an inhomogeneous utilization inside an electrode layer during charging and discharging processes. With the cell developed by Klink et al.[200] and using LG as an exemplary electrode material, it is possible to differentiate between two relaxation processes – one inside the particles and one between the particles throughout the electrode layers. An overview of the potentials of the three electrode layers as well as the charge going in and out of each layer is given in Figure 4.6.
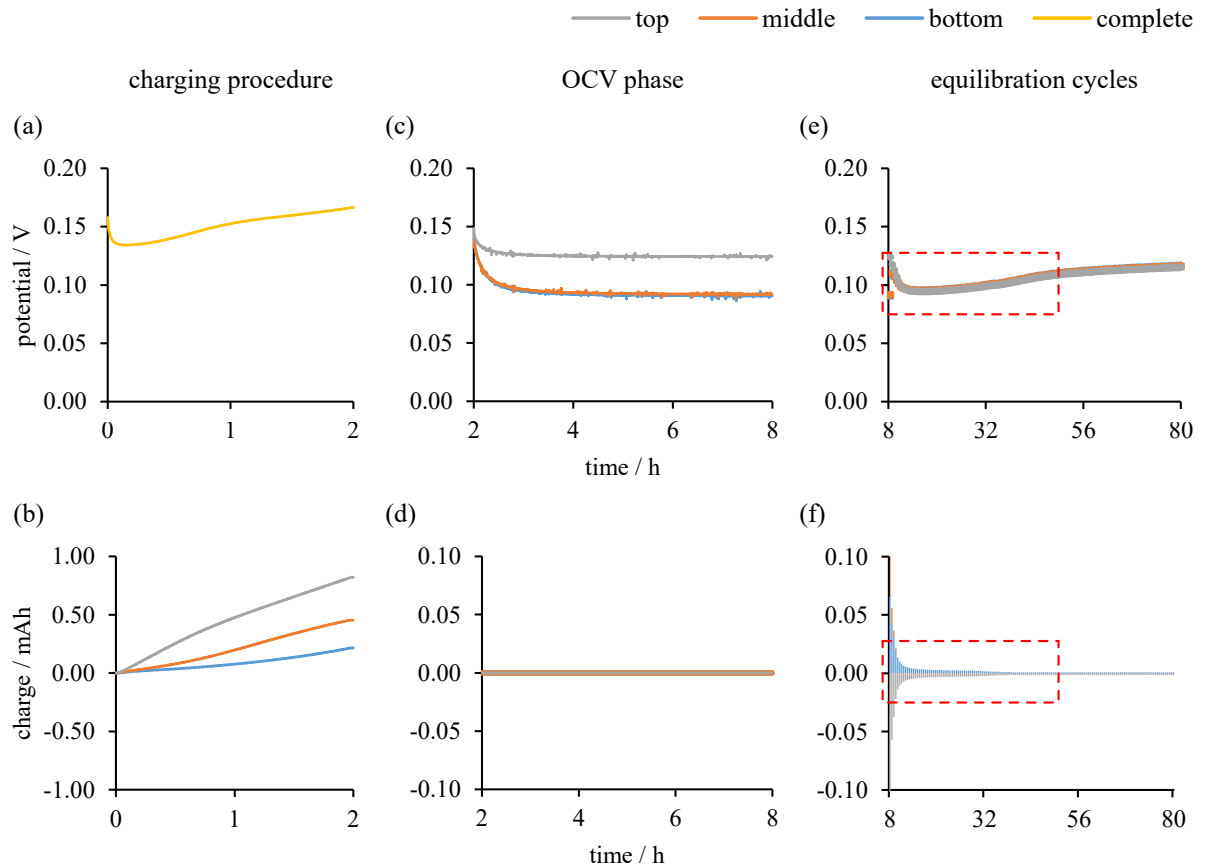
Figure 4.6: The upper array depicts the potentials of the three electrode layers or the complete cell, whereas the lower array shows the corresponding shifted charge during the charging step (a)–(b) and the following two relaxation steps (c)–(f). All plots are arranged sequentially, so the overall measurement time starting from the beginning of the charge phase is given

Starting from the fully lithiated state at the end of the formation process, the three graphite electrodes were delithiated via the master channel with the slave channels in CA mode which means that all graphite electrode layers are on the same potential. A C/10 current was applied for 2 h resulting in a charge of 20 % SOC. After the charging step, the equilibration measurement protocol as described in Section 4.2.2 was carried out. The total measurement time for the charging step, the 6 h OCV phase and the consecutive equilibration between the electrodes for 96 h added up to 104 h.

When looking into full cell arrangements both the intra-particle and the inter-particle processes are superimposed. The time for an assimilated electrode is in the order of 48 h and during that time an electrode is considered not to be in its equilibrium state. Although a C/10 rate as used in the experiments is not known for causing such great inhomogeneities, it appears to be reasonable with the comparably thick electrode of 132 µm (plus 25 µm of separator between the layers) resulting in a total electrode stack thickness of 182 µm.

We can thereby conclude that the hypothesis which was developed to explain long-time equilibration effects detectable with EIS measurements on lithium-ion cells[229] was accurate for – at least – the case of intra-particle and inter-particle equilibration through the electrode layer. The observed equilibration time of up to 48 h in EIS measurements is in accordance with the time a capacity exchange can be observed in the MLC cell after a comparable prior short-term history (see Figure 4.6 (f)).

Author contribution   The collaboration for the presented paper was initiated by me to prove our previous hypothesis. Stefan Klink at Ruhr University Bochum taught me how to use the MLC, while Jörg Schuster and Günter Ehlert helped producing the graphite mesh electrodes in the laboratory at TUM. Patrick J. Osswald, Andreas Noel and Simon V. Erhard supported me in adapting our measurement equipment to the respective requirements.

Measurements of lithium-ion concentration equilibration processes inside graphite electrodes

Frank M. Kindermann, Patrick J. Osswald, Stefan Klink, Günter Ehlert, Jörg Schuster, Andreas Noel, Simon V. Erhard, Wolfgang Schuhmann, Andreas Jossen

Permanent weblink:
`http://dx.doi.org/10.1016/j.jpowsour.2016.12.093`

Short communication

Measurements of lithium-ion concentration equilibration processes inside graphite electrodes

Frank M. Kindermann [a, *], Patrick J. Osswald [a], Stefan Klink [c], Günter Ehlert [a], Jörg Schuster [b], Andreas Noel [a], Simon V. Erhard [a], Wolfgang Schuhmann [c], Andreas Jossen [a]

[a] Institute for Electrical Energy Storage Technology, Technical University of Munich (TUM), Munich, Germany
[b] Chair of Technical Electrochemistry, Technical University of Munich (TUM), Munich, Germany
[c] Analytical Chemistry - Center for Electrochemical Sciences (CES), Ruhr-University Bochum, Bochum, Germany

HIGHLIGHTS

- Laboratory cell to measure spatial charge distribution in graphite electrode.
- Inhomogeneous current density distribution leads to long-term equilibration process.
- Intra-particle relaxation up to 4 h.
- Inter-particle relaxation can be measured more than 40 h.

ARTICLE INFO

ABSTRACT

Methods for estimating inner states in a lithium-ion cell require steady state conditions or accurate models of the dynamic processes. Besides often used inner states such as state-of-charge, state-of-health or state-of-function, relaxation processes strongly influence the mentioned states. Inhomogeneous utilization of electrodes and consequent limitations in the operating conditions have recently been brought to attention. Relaxation measurements after an inhomogeneous current distribution through the thickness of an electrode have not been addressed so far. By using a previously developed laboratory cell, we are able to show an inhomogeneous retrieval of lithium-ions from a graphite electrode through the layer with spatial resolution. After this inhomogeneity caused by a constant current operation, equilibration processes are recorded and can be assigned to two different effects. One effect is an equilibration inside the particles (intra-particle) from surface to bulk and vice versa. The other effect is an assimilation between the particles (inter-particle) to reach a homogeneous state-of-charge in each particle throughout the electrode layer. While intra-particle relaxation is observed to be finished within 4 h, inter-particle relaxation through the layer takes more than 40 h. The overall time for both equilibration processes shows to be in the order of 48 h.

© 2016 Elsevier B.V. All rights reserved.

1. Introduction

The field of applications for lithium-ion batteries grew considerably in the last decades. The initial device market has now expanded towards electric and hybrid vehicles as well as stationary storage systems. Each application includes a battery management system (BMS) that has to monitor the inner states of the involved lithium-ion cells. Various states are taken into account, e.g. state-of charge (SOC), state-of-health (SOH) or state-of-function (SOF). Knowing the mentioned states is crucial for a safe and meaningful operation of a cell.

Methods for state estimation (impedance or open circuit voltage (OCV) based) require a steady state condition or an accurate model of the cell's dynamics [1–5]. Since a battery is usually in operation, knowledge about the state-of-relaxation is indispensable for defining a steady state in the field or modeling the cell's dynamics accurately. Generally, relaxation processes can be described for

---

thermal, mechanical and electrical conditions. This work focuses on electrochemical relaxation processes, especially on equilibration processes due to state-of-charge inhomogeneities in graphite which is the anode in most commercial lithium-ion batteries. It is assumed that the equilibration in the graphite layer are long-term processes which is in accordance with experiments and simulation models in literature that address this issue [5–7]. To our knowledge, a quantitative measurement of the equilibration of lithium-ions spatially through a graphite anode has not been presented in the literature yet. SOC equilibration along the length of an electrode in a modified 26650 cell has recently been published by Osswald et al. [8].

Addressing the current distribution through a porous electrode with an experimental setup was first published by Coleman in 1951 [9]. In the context of lithium-ion batteries, Ng et al. [10] developed a setup based on a multi-layered graphite anode (three graphite layers) in a pouch cell for the measurement of a local SOC inhomogeneity due to the respective current distributions. A further development of this setup was presented by Klink et al. [11,12] to measure irreversible charging losses with advantages regarding the reproducibility and the possibility to address up to six layers of active material. This experimental setup is used in the presented work for measuring equilibration processes within a graphite particle on the one hand and through the graphite layer of a lithium-ion cell on the other hand.

2. Experimental

For the experiment, a laboratory cell introduced by Klink [11] was used to measure relaxation effects inside an electrode layer. The setup of the cell with its several individual working electrode layers — therefore called multi-layer cell (MLC) — can be seen in the provided scheme in Fig. 1. In this work, a setup with three graphite electrodes was chosen for a proof-of-principle.

Details on the used cell and measurement setup will be given in the following subsections.

2.1. Cell setup

2.1.1. Electrodes

A slurry containing graphite with a D50 value of 19 μm (provided by *SGL Carbon GmbH*) and PVdF binder (polyvinylidene fluoride; *Sigma-Aldrich*) in a 95:5 wt. ratio was prepared in NMP (*N*-methylpyrrolidone; *Sigma-Aldrich*) solvent. The slurry was coated on a Microgrid Cu25 copper mesh (provided by *Dexmet Corporation*) by an automatic coater (*RK Print*). The coating speed was 1.5 m min^{-1}. The mesh was chosen for its thickness of only 24 μm and a porosity of about 60%. Pressing the coated electrodes with a hydraulic stamping press, resulted in an electrode porosity of 32% and a thickness of 44 μm which corresponds to a loading of 4.13 mg cm^{-2}. Disks with 15 mm in diameter were punched out and resulted in a capacity of 2.48 mAh per layer. Measurements of the electrodes regarding the tortuosity (about $\tau = 5$) — as demonstrated by Landesfeind et al. [13] — showed similar results as commercial electrodes.

2.1.2. Assembly

Each electrode disk was contacted with a strip of copper mesh beneath it. On top of each disk a 25 μm thick Celgard 2325 separator with 19 mm in diameter was placed and 40 μl of LP57 electrolyte (1 M LiPF$_6$ in 3:7 EC:EMC; *BASF*) were added. After repeating this step for the other two electrode disks, a 260 μm glass fiber separator was used as an electrolyte reservoir prior to the lithium-metal (*Rockwood Lithium*) counter electrode. With this setup, a stack thickness of 467 μm (from lowest current collector to top of
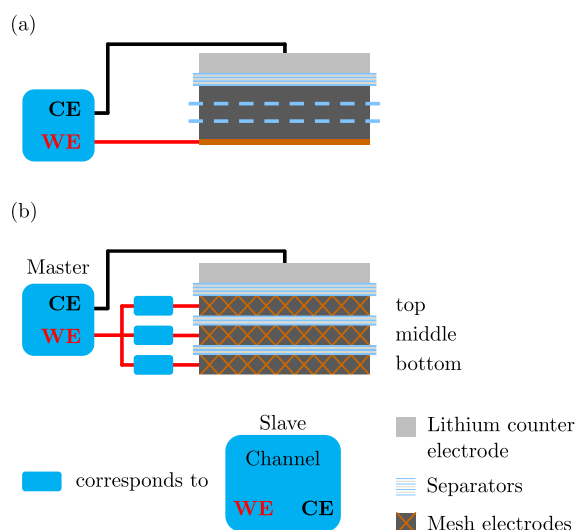

Fig. 1. Scheme of MLC with (a) showing the cross section of a typical half cell measurement versus a lithium-metal counter electrode (CE) (dashed lines represent the exemplary sectioning of this electrode) and (b) depicting the MLC setup with each layer being connected to a single potentiostat — called slave channel. A separate master channel is used for applying the "cell current" between the lithium counter electrode and the three working electrodes (WE).

topmost separator) with 132 μm of active electrode was achieved.

2.1.3. Formation

The formation of the MLC was performed while the graphite layers were short-circuited with a current of 0.37 mA corresponding to a theoretical C/20 rate on a VMP3 potentiostat/galvanostat by *Bio-Logic SAS*. Prior to the formation procedure, the cell was put to rest in a 25 °C temperature chamber for 10 h to guarantee complete soaking of separators and electrodes with electrolyte. The cell was cycled with a constant-current/constant-voltage (CCCV) procedure for 2.5 cycles, ending with a voltage phase at 50 mV for 96 h to achieve full lithiation of all three layers.

2.2. Measurement setup

As already introduced in Fig. 1, each layer can be operated and measured independently due to the usage of a separate potentiostat channel for each layer. A master channel operates the lithium electrode versus the graphite layers and represents a typical half cell setup which is, therefore, called complete cell. The single channels used for the graphite layers are called slave channels, since they are only operated in an observer mode and all driving currents are provided by the master channel. By a time controlled measurement protocol, the slave and master channels switch between an open-circuit mode (OCV) and a chronoamperometry mode (CA), the latter basically corresponding to a short-circuit of the chosen channel with passed charge recording.

Starting from the fully lithiated state at the end of the formation process, the graphite electrodes were delithiated via the master channel with the slave channels in CA mode which means that all graphite electrode layers are on the same potential. The drawn current was 0.75 mA (corresponds to C/10) for 2 h, resulting in a charge of the cell of 1.5 mAh. Please be aware that a charge in a half cell setup of lithium and graphite means a delithiation of graphite, since graphite acts as a cathode in this setup. A delithiation of graphite in a commercial lithium-ion cell with lithium transition

metal oxide or lithium-iron phosphate as a cathode, by contrast, corresponds to a discharge of the cell, since graphite acts as the anode.

After this charging step, the slaves switched to OCV mode for 6 h, separating the three layers from each other. The simultaneous short-circuiting of the master channel enabled a potential measurement of each layer versus lithium (refer to Fig. 1(b)) and potential relaxation for each layer was recorded.

In a next step, for equilibrating the individual layers the three slave channels were short-circuited for 29 min and OCV measured for 1 min afterwards. The master channel was operated in reverse (29 min OCV and short-circuited for 1 min) to the slaves during that time so that a potential measurement versus the lithium electrode was possible after each equilibration step. This allowed electrons to move from one graphite layer to another to compensate a possible lithium-ion exchange between the layers during the 29 min time slot. The equilibration regime was repeated for 191 times to identify when the layers are equilibrated. This lead to a total equilibration time between the electrodes of 96 h.

3. Theory

The measurement protocol was designed to prove the concept of a previously developed hypothesis to explain relaxation effects as observed in repeated long-term impedance measurements [5].

The hypothesis assumes three equilibration processes inside an electrode which emerge from observed inhomogeneities in the state-of-charge distribution due to overpotentials and kinetic limitations during cycling [14—16]. Effect (I) describes an intra-particle equalization process that compensates for slow diffusion inside each particle leading to a higher (or lower) concentration on the particle's surface compared to the particle's bulk. The surface lithium-ion concentration of a particle actually gives the potential measured for that particle. Both inter-particle effects (II)/(III) are due to a preferential utilization caused by the geometrical setup of a cell. Effect (II) causes a higher utilization near the separator and, therefore, counter electrode due to limitations in the conductivity of the electrolyte by porosity and tortuosity through the electrode. In contrast, the differing utilization by effect (III) is due to the connection of the electrodes and conductivity limitations in the electrical path of the current collector. All three effects and their equilibration paths can be seen in Fig. 2.

Since the used electrode disks with their diameter of 15 mm are quite small in their areal extent and the connection is proportionally large, effect (III) is considered negligible in this work. Osswald and co-workers already showed a variation in the current density distribution along the electrode length of a modified

commercial 26650 cell [15,17] whereas this work focuses on effects (I) and (II).

4. Results and discussion

As introduced in section 2, the graphite electrodes were delithiated (charged) from a fully lithiated state for 2 h with a 0.75 mA current, therefore, moving a charge of 1.5 mAh. Fig. 3(a) shows the recorded potential of the complete cell which is increasing during the charging step. The potential difference between the electrode layers is 0 V, since they are shorted for behaving like a single electrode. Please note that the time is given as the overall time from the start of the delithiation process to the end of the monitoring phase.

By comparing the charge throughput of the three electrodes in Fig. 3(b), it becomes evident that the electrode layers are used inhomogeneously. The top electrode delivered most of the lithium-ions with 0.82 mAh (corresponds to 55% of the overall charge throughput), the middle one less with 0.45 mAh (30%) and the bottom the least with 0.22 mAh (15%).

4.1. Intra-particle equilibration

After the charging current was turned off, the electrodes were monitored separately in an OCV phase versus the lithium electrode for 6 h to observe the relaxation process in each layer.

Fig. 3(c) shows a potential relaxation that is finished within 4 h (corresponds to 6 h absolute time). The middle and bottom electrode are in the same potential window versus lithium, despite different amounts of lithium were deintercalated. Due to the flat voltage profile for a certain SOC range, it is assumed that both layers still remain at the same lithiation stage which corresponds to a stage-1 plateau at about 85 mV versus Li/Li^+ as reported by Ohzuku et al. [18]. The top electrode exhibits a higher potential than the other two electrodes as most of the charge was extracted from this layer. The higher utilization of the top layer due to transport limitations through the electrode, resulted in a final delithiation state in the stage-2 plateau of graphite at about 120 mV versus Li/Li^+ [18]. As can be seen in the corresponding Fig. 3(d), no charge was transferred between the electrode layers.

Since the used electrodes are comparably thin (44 μm in mesh holes and 20 μm on mesh with 19 μm particles), a relaxation effect (II) within each layer cannot be excluded but is expected to be small. Therefore, the observed potential decrease in Fig. 3(c) can be explained approximately with effect (I), the intra-particle equilibration of lithium-ions between the particle's bulk and surface. As the cell — and the particles — gets delithiated, a lithium-ion depletion on the surface is expected which leads to a higher
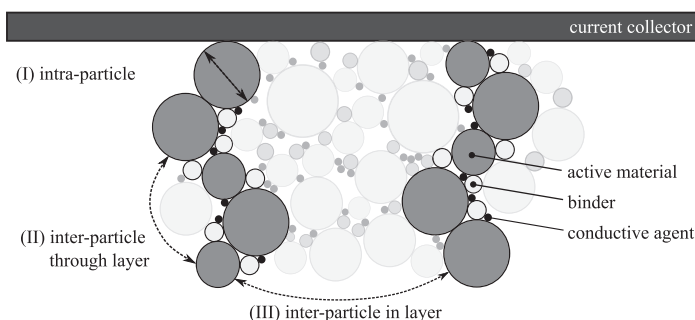

Fig. 2. Hypothesis to describe different equilibration effects inside the particles (I) and between the particles (II) and (III) [5].
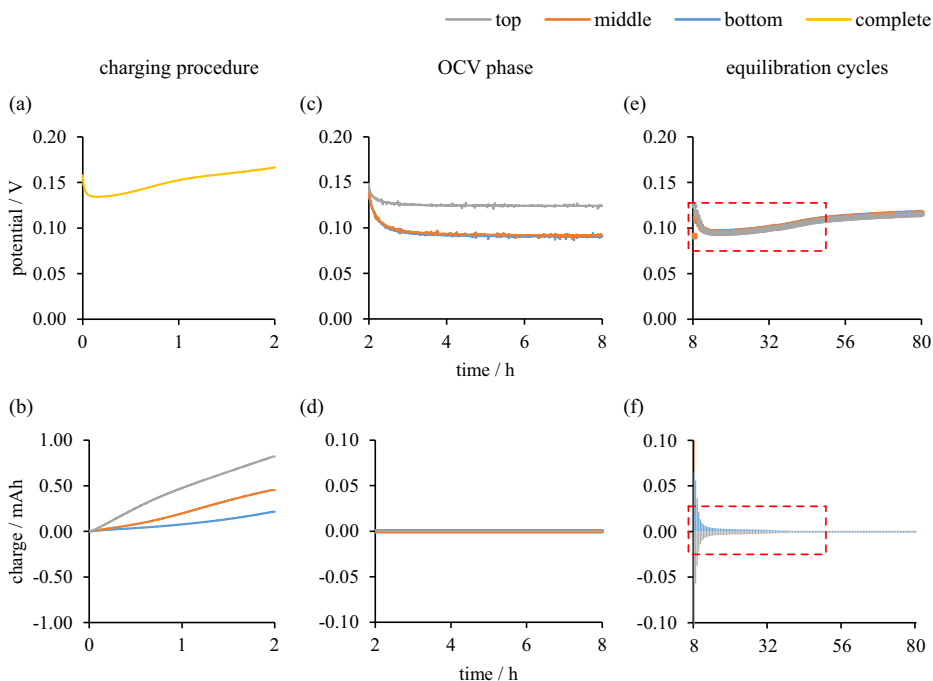
Fig. 3. The upper array depicts the potentials of the three electrode layers or the complete cell, whereas the lower array shows the corresponding shifted charge during the charging step (a)–(b) and the following two relaxation steps (c)–(f). All plots are arranged sequentially, so the overall measurement time starting from the beginning of the charge phase is given.

potential. After terminating the delithiation process, lithium-ions will diffuse from the bulk to the surface of the particle and thereby decrease the measurable potential.

Furthermore, the initial drop from the complete cell to the starting potential of the relaxation (2 h value in Fig. 3(a) and (c)) is caused by the ohmic drop after cutting off the charging current.

4.2. Inter-particle equilibration

The previously described OCV phase was followed by a 29 min short-circuiting of the layers to enable equilibration between the three layers (i.e. electrons take the path through the slave channels and lithium-ions diffuse through the electrolyte phase via the
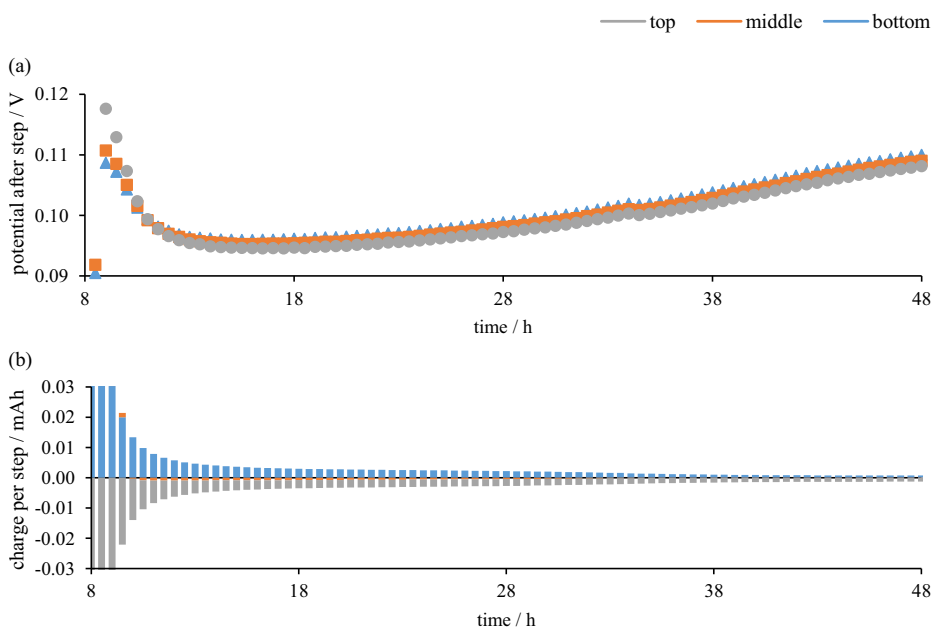
Fig. 4. Zooming into plots (e)–(f) of Fig. 3, shows (a) fast assimilation of the layers' potentials and (b) small charges transferred during equilibration steps for 40 h.

separators). Each equilibration phase was followed by a 1 min OCV phase to measure the potentials of each layer. The last measured value of the potential results for 72 h (i.e. 8 h—80 h total time) out of 96 h (afterwards no further changes can be seen) during that equalization process are depicted in Fig. 3(e).

As can be seen in Fig. 3(e), the potentials drop and reach a minimum after about 8 h (16 h total time) and increases afterwards. Since the OCV phase to measure the potential of each electrode layer is rather short, an intra-particle relaxation cannot be concluded during that time. Therefore, an overall potential decrease can be observed that subsides after the exchanged charge between the layers decreases and shows in an increase of the potential. The finally reached potential of the three electrodes is slightly below the potential of the top electrode before the equilibration phase. This can be seen in detail in Fig. 4(a) and (b). The potential difference of approximately 1 mV is assumed to originate from the geometrical setup of the cell. Each layer below the top electrode includes an additional distance of about 69 μm (separator and mesh electrode) towards the counter electrode that results in a larger electrolyte resistance causing the potential increase.

Fig. 4(a) and (b) show the potential development of the OCV phase and the exchanged charge during each short-circuit cycle on an enlarged scale. Since the top electrode was the most delithiated one, in the beginning charge the lower two electrodes is transferred into the top layer (see negative half-plane). For the lower two electrodes the measurement shows that the middle one, which was more delithiated than the bottom one, delivers less capacity for the redistribution than the least delithiated bottom electrode (see Fig. 3(a)). After 2 h the middle electrode switches from delithiation to lithiation. By comparison with Fig. 4(a), it can be observed that there is still a small charge exchange for hours even after the potentials of the three graphite layers have assimilated. The overall decrease of the potential during the first hours of the equilibration between the layers is due to an assimilation current of up to 0.75 mA within the first CA phase. This results in overpotentials that decrease the measurable potential during the 1 min OCV phase. Since the exchanged current decreases with each equilibration cycle due to smaller differences between the layers, the overpotential subsides and the measured potential increases. Also, the convergence towards an overall stage-2 potential is responsible for the increase.

Summarizing the introduced measurements, it becomes obvious that a charging or discharging step leads to an inhomogeneous utilization of the electrode although just an overall mixed potential can be recorded on the outside of a cell. Equilibration processes in the electrode can be observed for 40 h, although the potentials already assimilated, which is consistent with simulations and impedance measurements shown before [5].

5. Conclusion

In this work, we presented a way to measure equilibration processes caused by an inhomogeneous utilization inside an electrode layer during charging and discharging processes. With the cell developed by Klink et al. [11] and using graphite as an example, it is possible to differentiate between two relaxation processes — one inside the particles and one between the particles.

When looking into full cell arrangements both the intra-particle and the inter-particle processes are superimposed. The time for a mostly assimilated electrode is in the order of 48 h and during that time an electrode is not in its equilibrium state. Although a C/10

rate as used in the experiments is not known for causing such great inhomogeneities, it appears to be reasonable with the very thick electrode.

We can thereby conclude that the hypothesis which was developed to explain long-time equalization effects detectable in impedance measurements on lithium-ion cells [5] was accurate for — at least — the case of effect (I) and (II). The observed assimilation time of up to 48 h is in accordance with the time a capacity exchange can be observed in the MLC cell after a comparable prior short-term history.

Future work will elaborate on the influence of particle sizes and their distribution on the ratio between effect (I) and (II).

Acknowledgment

References

[1] H. He, X. Zhang, R. Xiong, Y. Xu, H. Guo, Online model-based estimation of state-of-charge and open-circuit voltage of lithium-ion batteries in electric vehicles, Energy 39 (1) (2012) 310—318, http://dx.doi.org/10.1016/j.energy.2012.01.009.

[2] W. Waag, D.U. Sauer, Adaptive estimation of the electromotive force of the lithium-ion battery after current interruption for an accurate state-of-charge and capacity determination, Appl. Energy 111 (2013) 416—427, http://dx.doi.org/10.1016/j.apenergy.2013.05.001.

[3] M. Petzl, M.A. Danzer, Advancements in OCV measurement and analysis for lithium-ion batteries, IEEE Trans. Energy Convers. 28 (3) (2013) 675—681, http://dx.doi.org/10.1109/TEC.2013.2259490.

[4] E. Barsoukov, J.R. Macdonald, Impedance Spectroscopy, John Wiley & Sons, Inc., Hoboken, NJ, USA, 2005, http://dx.doi.org/10.1002/0471716243 arXiv:0709.1163.

[5] F.M. Kindermann, A. Noel, S.V. Erhard, A. Jossen, Long-term equalization effects in li-ion batteries due to local state of charge inhomogeneities and their impact on impedance measurements, Electrochimica Acta 185 (2015) 107—116, http://dx.doi.org/10.1016/j.electacta.2015.10.108.

[6] D.M. Bernardi, J.-Y. Go, Analysis of pulse and relaxation behavior in lithium-ion batteries, J. Power Sources 196 (1) (2011) 412—427, http://dx.doi.org/10.1016/j.jpowsour.2010.06.107.

[7] T.F. Fuller, Relaxation phenomena in lithium-ion-insertion cells, J. Electrochem. Soc. 141 (4) (1994) 982, http://dx.doi.org/10.1149/1.2054868.

[8] P.J. Osswald, S.V. Erhard, A. Rheinfeld, B. Rieger, H.E. Hoster, A. Jossen, Temperature dependency of state of charge inhomogeneities and their equalization in cylindrical lithium-ion cells, J. Power Sources 329 (2016) 546—552, http://dx.doi.org/10.1016/j.jpowsour.2016.08.120.

[9] J.J. Coleman, Distribution of current in porous electrodes, J. Electrochem. Soc. 98 (7) (1951) 26, http://dx.doi.org/10.1149/1.2778099.

[10] S.-H. Ng, F. La Mantia, P. Novák, A multiple working electrode for electrochemical cells: a tool for current density distribution studies, Angew. Chem. Int. Ed. 48 (3) (2009) 528—532, http://dx.doi.org/10.1002/anie.200803981.

[11] S. Klink, W. Schuhmann, F. La Mantia, Vertical distribution of overpotentials and irreversible charge losses in lithium ion battery electrodes, ChemSusChem 7 (8) (2014) 2159—2166, http://dx.doi.org/10.1002/cssc.201400056.

[12] S. Klink, P. Weide, M. Muhler, W. Schuhmann, F. La Mantia, New insights into sei formation in lithium ion batteries: inhomogeneous distribution of irreversible charge losses across graphite electrodes, ECS Trans. 62 (2014) 265—271, http://dx.doi.org/10.1149/06201.0265ecst.

[13] J. Landesfeind, J. Hattendorff, A. Ehrl, W.A. Wall, H.A. Gasteiger, Tortuosity determination of battery electrodes and separators by impedance spectroscopy, J. Electrochem. Soc. 163 (7) (2016) A1373—A1387 doi:0.1149/2.1141607jes.

[14] P.J. Osswald, S.V. Erhard, J. Wilhelm, H.E. Hoster, A. Jossen, Simulation and measurement of local potentials of modified commercial cylindrical cells i: cell preparation and measurements, J. Electrochem. Soc. 162 (10) (2015) A2099—A2105, http://dx.doi.org/10.1149/2.0561510jes.

[15] S.V. Erhard, P.J. Osswald, J. Wilhelm, A. Rheinfeld, S. Kosch, A. Jossen, Simulation and measurement of local potentials of modified commercial cylindrical cells ii: multi-dimensional modeling and validation, J. Electrochem. Soc. 162 (14) (2015) A2707–A2719, http://dx.doi.org/10.1149/2.0431514jes.

[16] G. Zhang, C.E. Shaffer, C.-Y. Wang, C.D. Rahn, In-situ measurement of current distribution in a Li-Ion cell, J. Electrochem. Soc. 160 (4) (2013) A610–A615, http://dx.doi.org/10.1149/2.046304jes.

[17] P.J. Osswald, S.V. Erhard, A. Noel, P. Keil, F.M. Kindermann, H. Hoster, A. Jossen, Current density distribution in cylindrical li-ion cells during impedance measurements, J. Power Sources 314 (2016) 93–101, http://dx.doi.org/10.1016/j.jpowsour.2016.02.070.

[18] T. Ohzuku, Y. Iwakoshi, K. Sawai, Formation of lithium-graphite intercalation compounds in nonaqueous electrolytes and their application as a negative electrode for a lithium ion (shuttlecock) cell, J. Electrochem. Soc. 140 (9) (1993) 2490–2498, http://dx.doi.org/10.1149/1.2220849.

4.5 Reducing inhomogeneous current density distribution in graphite electrodes by design variation

The goal of this paper was to derive an electrode design that allowed for a more homogeneous current density distribution during operation of the cell and subsequent shorter equilibration times.

To understand the influence of particle sizes, we repeated the MLC measurements with another graphite composed of smaller particle radii. When comparing the current density distribution and equilibration data from both particle sizes, it was shown that electrodes with higher porosity and smaller particle sizes were utilized more homogeneously than with large particles.

With the collected data, we parametrized a P2D model with three distinctive particle sizes to account for relaxation process in the laboratory MLC design for a graphite half-cell. As a standard P2D model is not able to reproduce the geometry of the MLC with three separated layers, a new coupling boundary condition based on Kirchhoff's laws was introduced for the first time. This modeling approach showed very good agreement with the previously collected data.

To identify the contributions of the different solid and liquid phase properties, we conducted a variation study of the influencing parameters. Within our model we saw that electrodes with smaller particles were utilized more homogeneously and also equilibrate faster due to the higher surface to volume ratio of the small particles and the shorter diffusion pathways from center to surface of the particles. For a homogeneous utilization, liquid phase parameters such as porosity, tortuosity, electrolyte conductivity and the diffusion coefficient of the electrolyte still showed a higher impact than parameters of the solid phase i.e. particle radius, electrode conductivity and solid phase diffusion.
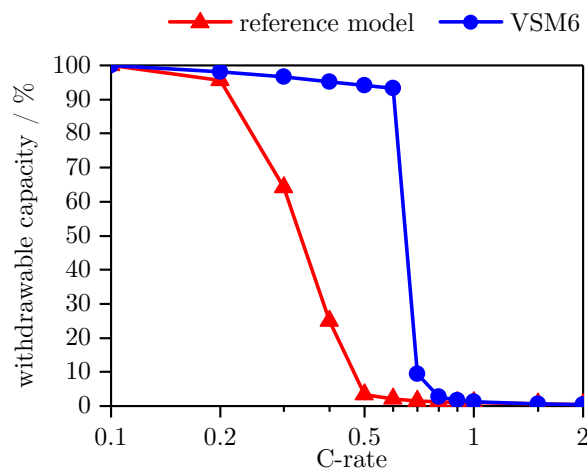

Figure 4.7: Comparison of reference (unstructured) and VSM6 (structured) electrode in a rate capability test. The withdrawable capacity is normalized to the capacity at C/10. The sudden decrease in withdrawable capacity can be attributed to diffusion limitations in the electrolyte.

Due to the experiences gained by identifying parameter influences on electrode utilization and equilibration, we carried out design variation studies for improving electrode utilization with the aid of the model. During the variation studies, it was observed that smaller graphite particles are beneficial near the current collector and larger particles near the separator toward the counter electrode. Also, a porosity increase from separator to current collector showed a better utilization as the hard to

reach pores near the current collector present a larger reservoir for lithium-ions which postpones rate limitations toward higher C-rates. The biggest improvement was achieved by reducing the tortuosity overall and from separator to current collector. The latter case could be implemented by including pore channels into the graphite electrode by means of laser beam structuring after the coating and calendering process during manufacturing. When performing a rate capability test for a cell with a standard electrode (reference model) and the best-performing electrode design from the variation studies (VSM6), Figure 4.7 shows an improved rate behavior for the structured electrode.

Although the structuring leads to a better rate capability, it also increases the volume of the cell as the cell capacity is kept constant while the porosity increases. As the additional volume will be filled with electrolyte, the mass of the cell will increase as well. If energy density and specific energy are defined at a rate where the reference cell does not run into diffusion limitations (e.g. at C/10), the structured electrode cell shows inferior properties than the reference cell. However, at e.g. C/2 the increase in retrievable capacity outperforms the increase in volume and mass and the structured cell will be considered superior.

In conclusion, the structuring of electrodes is a promising way to achieve a more homogeneous utilization in thick electrodes for high energy cells. The more homogeneous utilization during operation will lead to shorter equilibration times and also to a more homogeneous aging behavior which is largely caused by the current density distribution.

Reducing Inhomogeneous Current Density Distribution in Graphite Electrodes by Design Variation

Frank M. Kindermann, Patrick J. Osswald, Günter Ehlert, Jörg Schuster, Alexander Rheinfeld, Andreas Jossen

Permanent weblink:
`http://dx.doi.org/10.1149/2.0131711jes`

Reducing Inhomogeneous Current Density Distribution in Graphite Electrodes by Design Variation

Frank M. Kindermann,[a,*,z] Patrick J. Osswald,[a] Günter Ehlert,[a] Jörg Schuster,[b,*] Alexander Rheinfeld,[a,*] and Andreas Jossen[a]

[a]*Technical University of Munich (TUM), Institute for Electrical Energy Storage Technology, Munich, Germany*
[b]*Technical University of Munich (TUM), Chair of Technical Electrochemistry, Garching, Germany*

Inhomogeneous utilization of electrodes and consequent limitations in the operating conditions are a severe problem, reducing lifetime and safety. By using a previously developed laboratory cell setup, we are able to show an inhomogeneous retrieval of lithium-ions from a graphite electrode throughout the layer with spatial resolution for two different graphites. After provoking inhomogeneities via constant current operations, equilibration processes are recorded and are assigned to two different effects. One effect is an equilibration inside the particles (intra-particle) from surface to bulk whereas the second effect is an equalization between the particles (inter-particle) to reach a homogeneous degree of lithiation in each particle throughout the electrode layer. With the recorded data, we implemented a P2D model with multiple particle sizes and considered the electrode thickness in several separate domains. Using the relaxation data of intra- and inter-particle relaxation for parametrizing the model, we investigated the influence of different solid and liquid phase parameters. As the liquid phase parameters scaled via porosity and tortuosity showed the biggest impact, we performed a design variation study to achieve a more homogeneous utilization of the electrode. Structuring the electrode to lower tortuosity is identified as the most promising design variation for homogeneous utilization.

Lithium-ion cells are the electrochemical power source of choice, not only for portable electronic devices but also for plug-in hybrid electric vehicles (PHEVs) and electric vehicles (EVs). Despite significant improvements regarding energy density and cycle stability, drawbacks remain, preventing the acceptance of EVs as a coequal alternative to internal combustion engine vehicles.

Resulting from advancements in the quality of manufacturing processes, the ratio between active and inactive components could be improved by realizing thicker electrode coatings and thinner current collector foils.[1] This increase in the energy density of the cells, however, comes with longer charging times due to a reduced rate capability. While concepts such as intelligent charging strategies require a comprehensive framework to be implemented,[2] the most obvious approach is to increase the charging power. As presented by Tesla's Supercharger concept, the battery is charged up to 80% state of charge (SOC) within 40 min using a charging power of up to 120 kW.[3] The high charging power requires high charging currents due to current limitations for 400 V high voltage on-board power systems.

Various publications address the variations in current density distribution and the resulting SOC inhomogeneities. The impact of the cell design and the resulting equalization processes along the electrodes are presented using experimental cells[4–11] or by a modeling approach.[12,13] The resulting inhomogeneous utilization of the active material leads to undesired side reactions and accelerated degradation, especially lithium plating[14,15] and an uneven mechanical expansion of the anode.[16] This is further provoked by the increasing thickness of the cell's electrodes. In contrast to the equalizing process along the electrode, only limited knowledge regarding the process throughout the electrode thickness are available.

Consequently, a fundamental understanding of the lithium-ion transport mechanisms is a crucial requirement to enable intelligent fast charging strategies. In our previous work,[17] a hypothesis was presented, discussing possible lithium-ion relaxation processes inside a lithium-ion cell. The first effect is an equilibration inside the particles, where the concentration gradient between the bulk and the surface of graphite particles leads to an intra-particle equalization process. The

second effect addresses the equalization between different particles (inter-particle), where the equalization of the lithium-ion concentration gradient occurs through the electrolyte. This equalization was successfully observed using an experimental test cell, where the anode consisted of three separated graphite layers[18] based on the works of La Mantia et al.,[19] Ng et al.[20] and Klink et al.[21,22] During normal operation, the layers were connected and performed as a single electrode. After full lithiation, a charge step was performed and the layers, based on the geometric proximity to the counter electrode, provided an unequal amount of the required charge. After switching off the current, the potential of all three layers was observed individually and the equalization currents between the single layers were measured.

In this paper we show measurements of inhomogeneous extraction of lithium-ions and following equalization processes for two different types of graphite. With these data we implement a P2D model with three separated electrodes to study the influence of several solid and liquid phase parameters on the observed current density distribution. According to the investigated parameters, we perform a design variation study to achieve a more homogeneous utilization.

Experimental and Measurements

The measurement data were gathered with a previously presented laboratory cell design called multi-layer cell (MLC).[21] These data was then used to parametrize our model for a consecutive design variation study.

Experiment.—In addition to our previous work that was carried out on a graphite with a D50 value of 19 μm (referred to as large particle graphite – LG), we repeated the same equilibration measurements after an inhomogeneous utilization of the electrodes for a smaller particle graphite with a D50 value of 2.3 μm (small particle graphite – SG) according to the manufacturer. The experimental setup can be seen in Figure 1 and is described in more detail in Reference 18.

Both graphites were processed in a similar fashion. The graphite containing slurry and PVdF binder (polyvinylidene fluoride; Sigma-Aldrich) were mixed in a 95:5 wt ratio in NMP (N-methylpyrrolidone;

*Electrochemical Society Student Member.
[z]E-mail: f.kindermann@tum.de

(a)

(b)

Master

top
middle
bottom

corresponds to

Slave

Channel

WE   CE

Lithium counter electrode
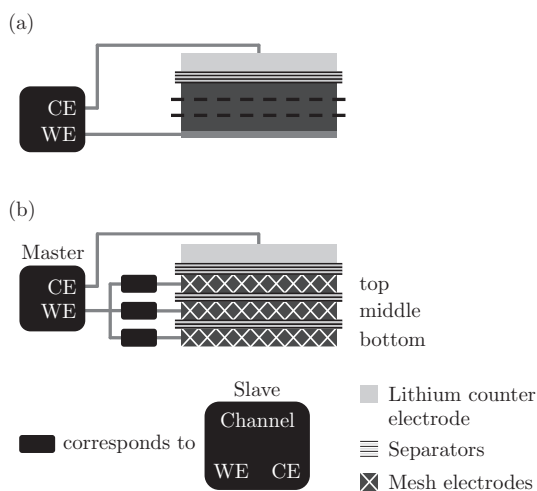
Separators

Mesh electrodes

Figure 1. Scheme of cell setup showing (a) the cross section of a typical half-cell measurement versus a lithium-metal counter electrode (CE). The dashed lines represent the exemplary sectioning of this electrode which is implemented in (b) with each layer being connected to a single potentiostat – called slave channels. A separate master channel is used for applying the "cell current" between the lithium counter electrode and the three working electrodes (WE).[18,21]

Sigma-Aldrich) solvent. The slurry was coated by an automatic coater (RK Print) on a Microgrid Cu25 copper mesh (provided by Dexmet Corporation) in the case of LG and on a MC33 copper mesh (Pre-

Table I. Properties of electrode disks from SG and LG. All values are measured or consequently calculated.

	SG	LG
Material properties		
D10 value	0.9 μm	7 μm
D50 value	2.3 μm	19 μm
D90 value	5.7 μm	47 μm
Mesh thickness	9 μm (MC33)	24 μm (Microgrid Cu25)
Electrode properties		
Coating thickness	70 μm	60 μm
Resulting thickness	42.5 ± 1 μm	44 ± 1 μm
Porosity	79 ± 2 %	32 ± 2 %
Tortuosity	3.7 ± 0.5	4.9 ± 0.5
Graphite loading	1.82 mg cm^{-2}	4.13 mg cm^{-2}
Capacity per disk	1.20 mA h	2.48 mA h

cision Eforming Ltd.) in the case of SG. The coating speed for both coatings was 1.5 m min^{-1}. The LG electrodes were compressed for 2 min with 2.5 t, whereas the SG electrodes were not treated due to mechanical instabilities arising during the pressing process. Porosities for both kinds of electrodes were calculated and respective tortuosities were measured as suggested by Landesfeind et al.[23] All properties comparing both electrode disks that were punched out with 15 mm in diameter are listed in Table I.

Measurement comparison.—By using the setup shown in Figure 1 with three electrode disks separated by a Celgard 2325 separator, we are able to measure the capacity going in or out of each layer
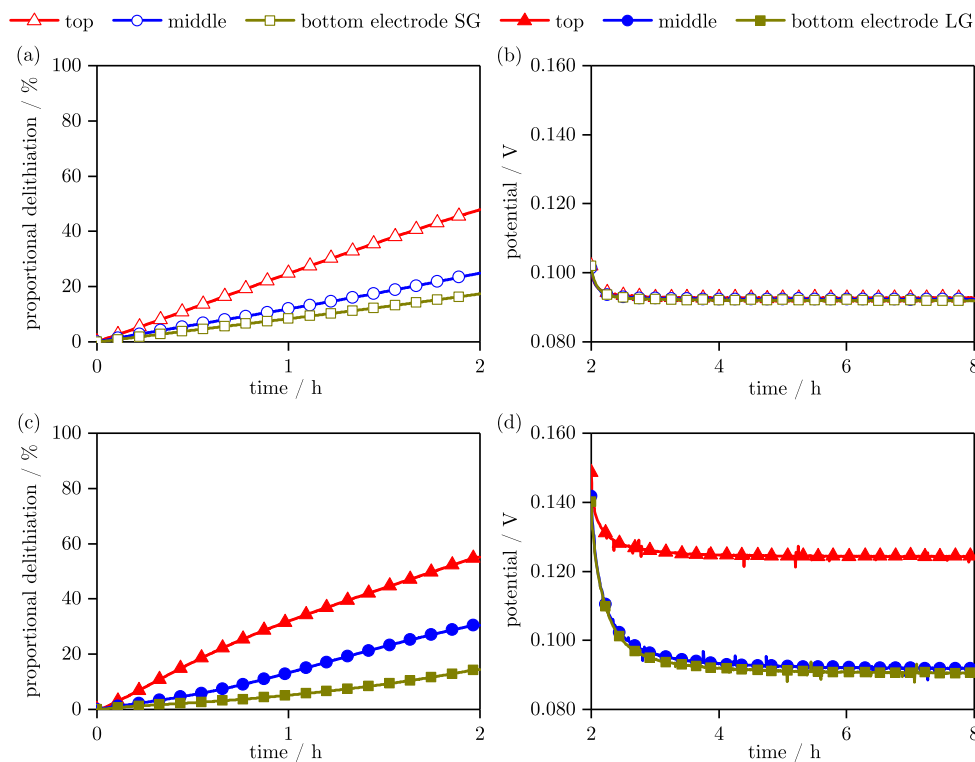

Figure 2. Comparison of SG (upper array) and LG (lower array) with respect to input capacity to each layer during 2 h delithiation process with C/10 current shown as percentage of overall capacity ((a) and (c)) and following intra-particle potential relaxation where no charge is exchanged between the layers ((b) and (d)). As can be seen, the disks were not delithiated equally by 33.3% but quite inhomogeneously. The most obvious effect can be seen in (d) as the top electrode of the LG was discharged that much more than the lower two electrodes that it relaxes to a stage-2 potential whereas the lower two electrodes stay in stage-1.

during a half-cell measurement mode and can additionally measure the potential of each disk versus Li/Li$^+$.

When comparing both graphites incorporated in a MLC setup during delithiation with a C/10 current for 2 h from a fully lithiated state, we can see that the SG electrodes show a more homogeneous utilization (Figure 2a and 2c) and a faster intra-particle relaxation (Figure 2b and 2d). The more homogeneous utilization with all particles still in the same lithiation stage (Figure 2b) is probably due to lower gradients in the electrolyte potential that come with the higher porosity and, therefore, lower tortuosity. The faster intra-particle equilibration of SG (slope/gradient in Figure 2b) is due to smaller concentration gradients inside the particles as the average diameter are much smaller (almost factor 10) for SG (D10/50/90 value = 0.9 μm/2.3 μm/5.7 μm) compared to LG (D10/50/90 value = 7 μm/19 μm/47 μm).

Prior to the measurements, the MLC was cycled with a C/20 formation regime at 25 °C.[18]

Model

To get a more fundamental understanding of the dominating processes resulting in an inhomogeneous utilization and to discuss possible design implications to improve the homogeneity of utilization, we implemented the MLC design in a model environment using COMSOL Multiphysics 5.2a.

The established model is of a pseudo-two-dimensional (P2D) class as introduced by Newman and co-workers[24,25] and used extensively in literature for different applications.[26–30] This modeling class was chosen for its accuracy in describing transport phenomena in the solid and liquid phase of a single electrode stack.[31] As the P2D model is extensively discussed in literature, we only show the modifications to the basic model and included a short summary with all relevant parameters in the Appendix.

Particle size distribution.—For the graphite electrodes we implemented three overlapping domains each with a different distinct particle radius to overcome the restriction made by the P2D approach in homogenizing all particles.[32–35] We used the given D values for the two graphites as the three representative sizes. To not change the

overall active volume V_s of the cell, the volumetric share k_m of each particle size needs to be considered.

$$V_s = \sum_m k_m \cdot V_{P,m} \qquad [1]$$

The impact of different particle sizes on relaxation has already been shown before by Darling et al.[36] The relatively slow lithium-ion transport inside the particles leads to high gradients especially in large particles. As a realistic distribution, we assumed a volumetric share of 2% for the D10, 67% for the D50 and 31% for the D90 particles as measured by Wilhelm et al.[37]

Separated electrode model.—To validate our model to the measured data, we first implemented just one electrode domain with a thickness of 132 μm which corresponds to adding up the three 44 μm electrode disks from the MLC. At the theoretical tab positions we included a measurement probe to compare the behavior to the MLC measurement data. As this model featured the observed inhomogeneous lithium-ion retrieval qualitatively but not in its actual distinctness, we extended the model by implementing the three electrode domains and the in-between separator domains separately. This lead to a better agreement of simulation and measurement data as transport limitations in the additional lengths of the separators were included. Another advantage was that the three electrode simulation enabled to distinguish between the relaxation effects (I) and (II). A comparison between the two modeled geometries and inherent data can be seen in Figure 3.

As the active domains with the charge-transfer reaction were separated, a single current density source boundary condition at $x = L$ was not sufficient. To allow for a collective current flow from all three electrodes and equilibration currents between the layers after stopping the overall current, the domains need to be coupled by extra boundary conditions. This coupling of three electronically separated electrodes in a one-dimensional model, where the boundary conditions mimic an external circuitry, has to our knowledge not been published yet and will be introduced in the following.

Figure 4 depicts all necessary potential and current definitions for the coupled operation. The overall applied current density i_{app} is split
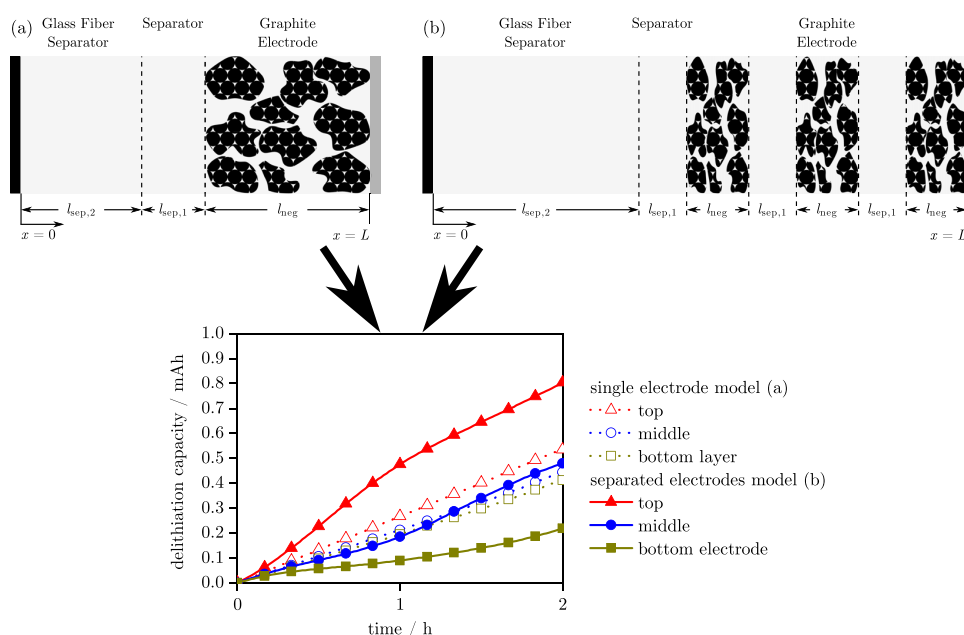

Figure 3. Comparison of modeling with (a) single thick electrode and (b) three separated electrodes.
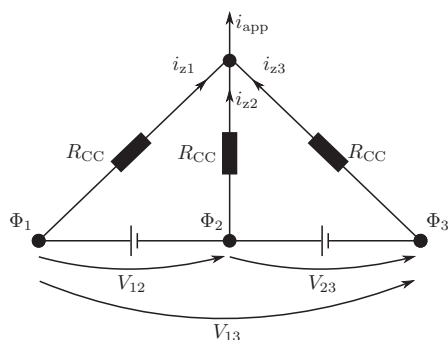
Figure 4. Depiction of potential and current definitions used in the coupling of the three separated electrode layers.

in a current for each layer $i_{z,i}$

$$i_{app} = \sum_i i_{z,i} \qquad [2]$$

The voltage V_{ij} in-between the separated layers is defined by the difference in their respective average potential at the current collector Φ_i and Φ_j

$$V_{ij} = \Phi_i - \Phi_j \qquad [3]$$

Applying Kirchhoff's laws to the scheme in Figure 4, the current density for each layer is dependent on the current density of the next layer, their voltage difference and the connection through a current

collector (R_{CC}) which is assumed the same for all layers

$$i_{z,i} = i_{z,j} + \frac{V_{ij}}{R_{CC}} \qquad [4]$$

We can sum up the model development part by stating that the three electrode modeling approach is superior in terms of matching the actual measurements to simulation results, although the thick single electrode approach is already sufficient to predict the degree of homogeneous utilization in a real application. The agreement of measurement and model data can be seen in Figure 5.

Results and Discussion

The purpose of developing a model to account for inhomogeneous utilization and following equilibration is being able to examine the extent of influence of different design parameters.

Identification of influencing parameters.—Starting with the parametrized three electrode model of LG, we varied parameters describing lithium-ion transport in the electrolyte phase as apparently the transport through the thickness of the electrode poses a limitation. (To achieve a better comparability, the total active material amount stays the same in all simulations, i.e. when increasing the porosity, the electrode length/thickness is also increased.) As the duration of equilibration is directly linked to the inhomogeneity of electrode utilization, Figures 6 and 7 only show the behavior of the retrieved charge from each layer compared to the initial values.

Changes of porosity and tortuosity are expected to have a similar impact on the diffusion coefficient and the electrolyte conductivity as they are scaling the transport parameters to effective values (see Equation A7). To achieve a 10 times larger effective diffusion coefficient of the electrolyte (Figure 6c) without changing the electrolyte
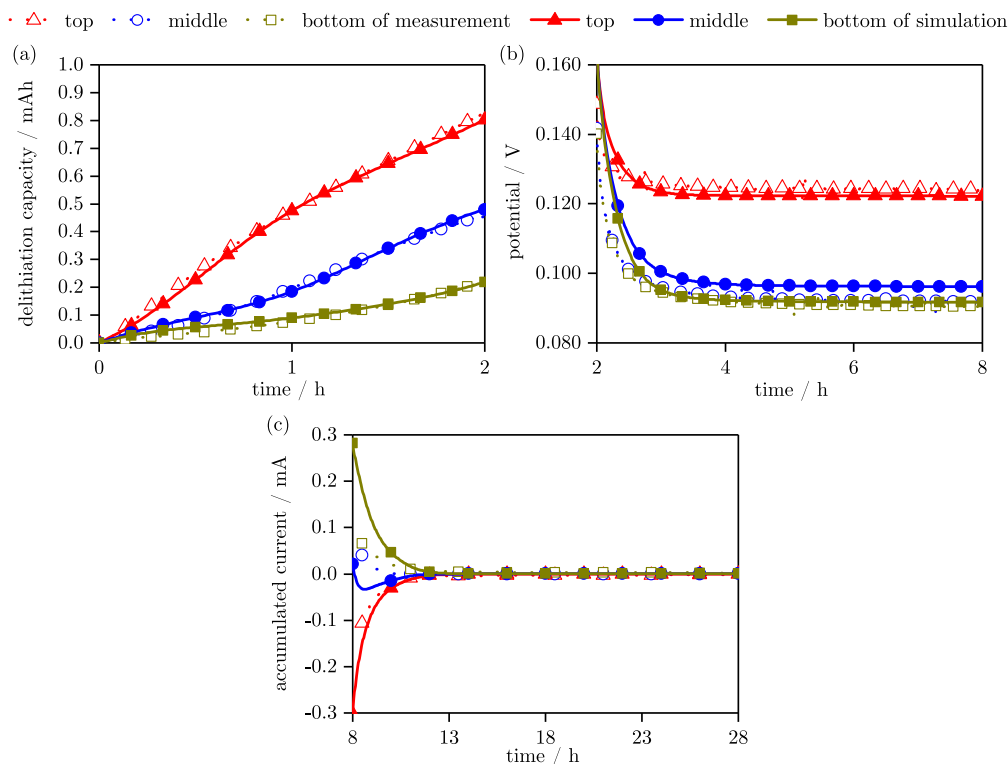

Figure 5. Comparison of measurement (hollow markers) and modeling (filled markers) results for MLC with LG particles during delithiation with C/10 rate and subsequent relaxation. (a) depicts the delithiation process of the three electrodes and (b) the intra-particle relaxation phase during which no charge is exchanged between the layers. (c) shows the current flowing during the 29 min inter-particle relaxation phases between the shorted layers (lines are for guidance purposes).
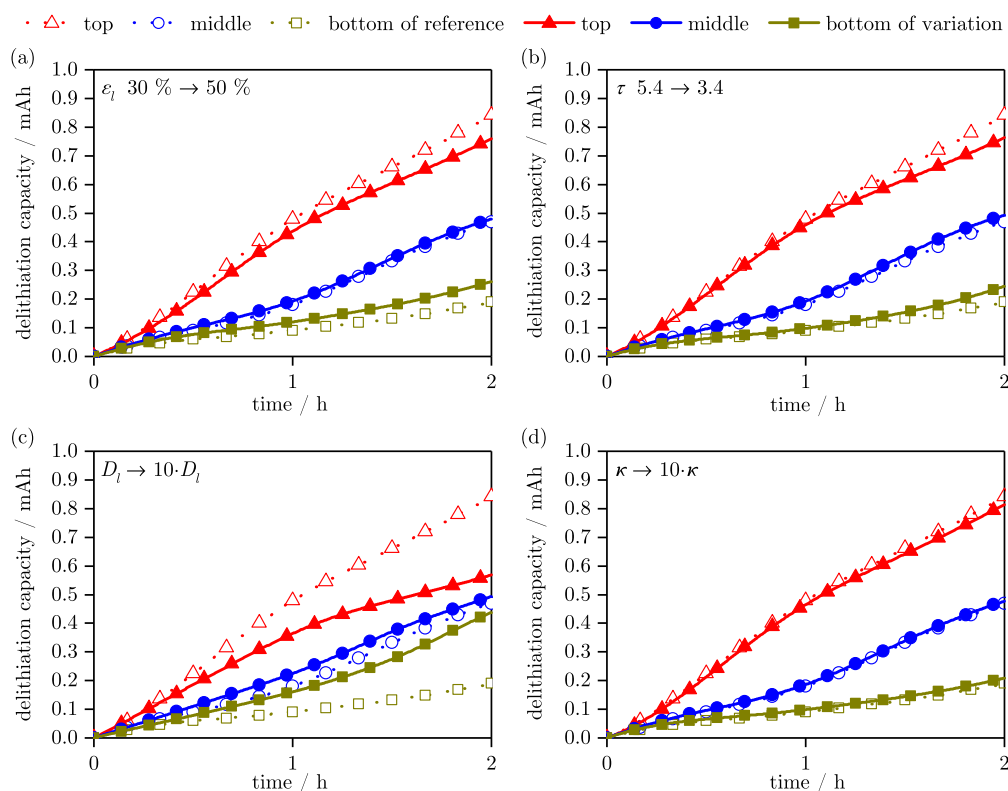
Figure 6. Utilization of the three layers by varying parameters regarding the electrolyte phase. The increase in (a) porosity (+20 %) and (b) decrease in tortuosity (−2) only shows minor improvement. Increasing the diffusion coefficient (c) by a factor of 10 shows a drastically more homogeneous utilization whereas the same increase for the conductivity (d) has almost no effect.

itself, the factor $\frac{\varepsilon_l}{\tau}$ would need to be ten times larger. In its extreme scenarios this implies that the porosity would need to increase by a factor of ten (which would result in a porosity larger than 100%) or the tortuosity would need to decrease by a factor of ten (which would result in a tortuosity smaller than 1). As both cases are impossible increasing the diffusion coefficient of the electrolyte itself seems like the only viable option. The fact that the mass and charge transport in the electrolyte is mainly diffusion controlled is consolidated as the increase in electrolyte conductivity shows no significant improvement (Figure 6d).

Similar to the comparison of parameters referring to the liquid phase, Figure 7 shows the influence of solid phase parameters. First, we included the particle radii distribution of the SG in the LG parametrized model as that gives a larger reacting surface at otherwise same conditions. As depicted in Figure 7a, this lead to consecutively following behavior where in the beginning the top electrode delivers even more charge which is later followed by the middle electrode. This behavior can be explained by the proportionally larger surface area of the SG that gets delithiated prior to the development of inhomogeneous surface potentials across the electrode that influence the charge-transfer. Increasing the particle radii would lead to a more homogeneous distribution in a first approximation but relaxation times would also rise significantly and are therefore left out of further discussions. Doubling the reaction rate constant – we assume the reaction rate constant as a parameter of the solid phase as the electrolyte is the same in all prior experiments – to allow for a faster (de-)intercalation of lithium-ions also leads to a slightly more inhomogeneous utilization as charge-transfer is encouraged even though there is a smaller driving potential. Similar to the change in reaction rate constant, increasing the diffusion coefficient in the graphite by a factor of 100 to allow for a faster homogenization inside the particle has only a

minor effect as the overall limitations originate from the liquid phase transport.

To summarize the study of influencing parameters, we see that the parameters influencing the effective electrolyte diffusivity have the biggest impact on the homogeneity of current density distribution across an electrode.

***Variation of electrode design for more homogeneous current density distribution.*—**Following the parameter analysis, we varied porosity, tortuosity and particle radii in the different layers to find a more homogeneous utilization by electrode design variation. The parameter combinations of the variation studies can be seen in Table II and the results are depicted in Figure 8. Primary modeling results showed a better utilization when using LG near the separator and SG near the current collector, so this is assumed in all following variations. An opposite distribution discharges the SG even faster due to the larger surface.[32] In addition to the previously introduced SG and LG samples, we modeled a made-up medium sized graphite (MG) for the variation studies that has a D10 value of 3.9 μm, a D50 value of 10.7 μm and a D90 value of 26.4 μm. Also, the effective thickness of the electrode layer varies in order to keep a constant area specific capacity per electrode layer with changing porosities. The overall thickness of all three electrodes is then in the range of 150 μm to 200 μm which is in the order of the goal for future high-energy cells.[38]

The first variation between variation study model 1 (VSM1) and 2 (VSM2) is a change in porosity. Whereas VSM1 has a decreasing porosity from top to bottom, VSM2 incorporates an increase. In Figure 8 we see a slightly more homogeneous utilization from (a) to (b). This is based on a larger reservoir of electrolyte within the pores near the current collector which dominates the rate limitation due to
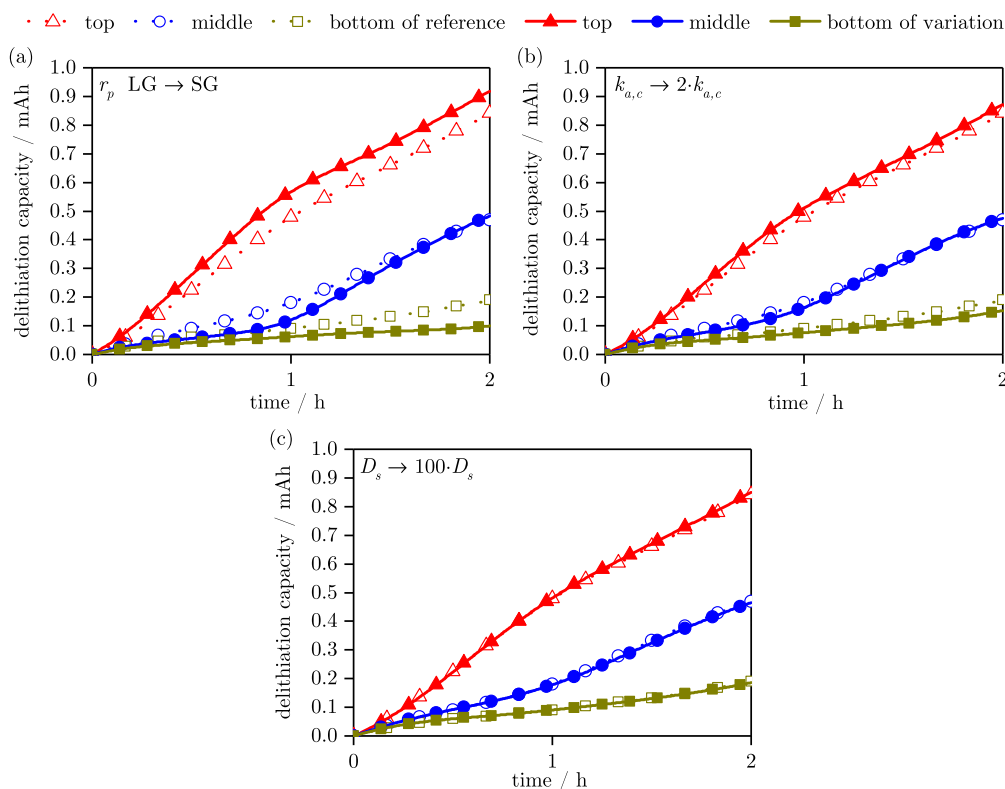
Figure 7. Reducing the particle radii by almost a factor of ten leads to an even more inhomogeneous, wave-like utilization (a). Doubling the reaction rate constant (b) or increasing the solid phase diffusion coefficient by a factor of 100 (c) shows a minor influence.

lithium-ion depletion (i.e. $c_l = 0$) as also suggested by e.g. Gallagher et al.[38]

A correlation of higher porosity leading to lower tortuosity was tested in VSM3. Compared to a more theoretical inverse correlation in VSM4, we can see better results for VSM4 in Figure 8c and 8d. The compensation of a lower porosity by a low tortuosity in VSM4 outperforms the very good effective transport parameters of the middle and bottom electrode of VSM3.

Based on the previous findings, we decreased the overall tortuosity which could represent an electrode morphology modified (i.e. structured) after coating and calendaring with the aid of a laser beam

to include "pore channels" through the electrode layer similar to the idea proposed by Bae et al.[39] As can be seen for VSM5 in Figure 8e, this bi-tortuos electrode morphology – which also leads to an increase in porosity due to extraction of material – allows for a considerably better electrode utilization. With VSM6, we investigated the actual impact of porosity for a pore channel electrode and simplified the assumption to a uniform 50%. By comparing Figure 8e and 8f, we see that the exact porosity has only a minor impact but that a structured electrode improving the overall tortuosity benefits a homogeneous utilization even in case of an almost 200 μm thick electrode.

Table II. Parameter combinations for the variation study models (VSM).

|	Reference	VSM1	VSM2	VSM3	VSM4	VSM5	VSM6
Top electrode							
Porosity ε_l	30%	50%	30%	30%	30%	40%	50%
Tortuosity τ	5.4	5.4	5.4	5.4	3.4	1.4	1.4
Particles	LG	LG	LG	LG	LG	LG	LG
Effective thickness	44.0 μm	64.0 μm	44.0 μm	44.0 μm	44.0 μm	52.1 μm	64.0 μm
Middle electrode							
Porosity ε_l	30%	40%	40%	40%	40%	50%	50%
Tortuosity τ	5.4	5.4	5.4	4.4	4.4	2.4	2.4
Particles	LG	MG	MG	MG	MG	MG	MG
Effective thickness	44.0 μm	52.1 μm	52.1 μm	52.1 μm	52.1 μm	64.0 μm	64.0 μm
Bottom electrode							
Porosity ε_l	30%	30%	50%	50%	50%	60%	50%
Tortuosity τ	5.4	5.4	5.4	3.4	5.4	3.4	3.4
Particles	LG	SG	SG	SG	SG	SG	SG
Effective thickness	44.0 μm	44.0 μm	64.0 μm	64.0 μm	64.0 μm	82.8 μm	64.0 μm
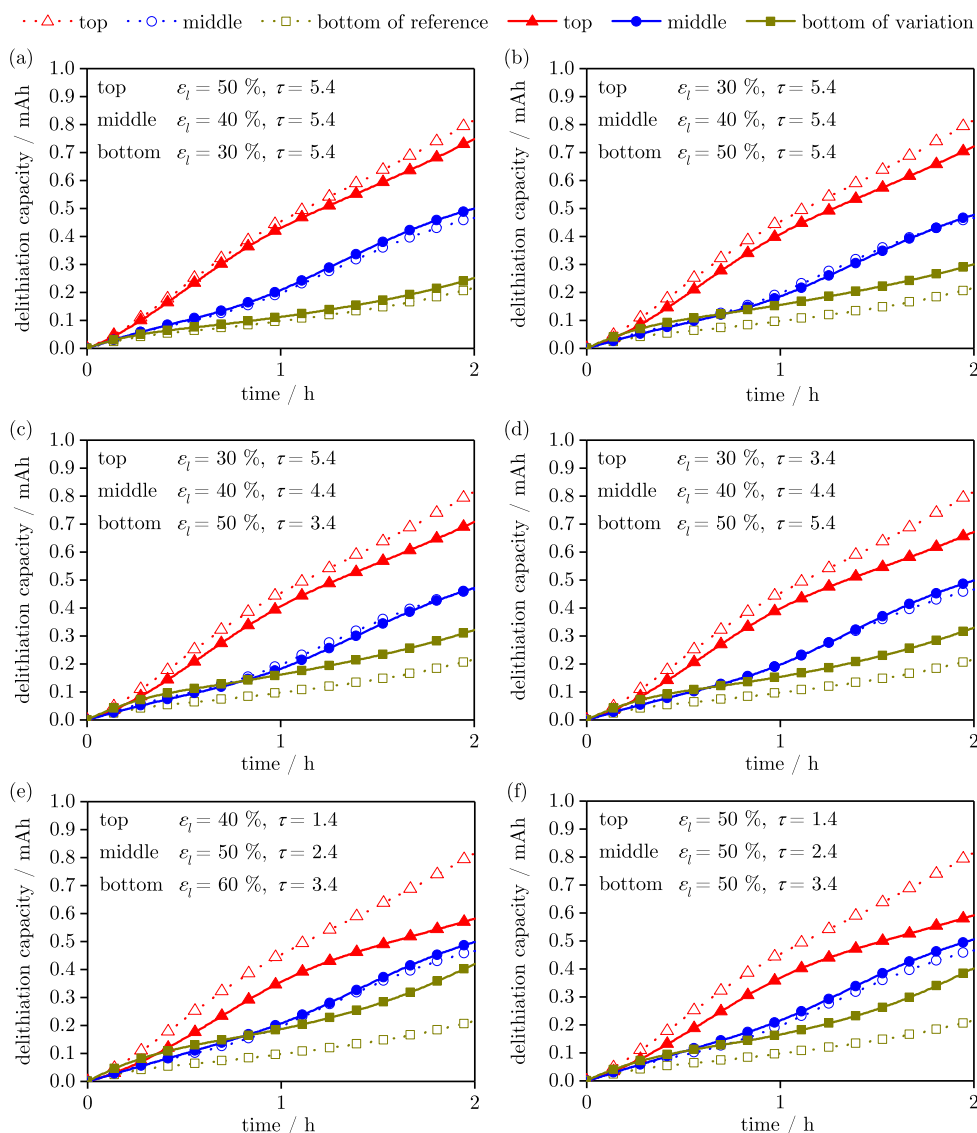
Figure 8. Effects of parameter variation studies as shown in Table II. (a)–(f) corresponds to VSM1–VSM6 and dashed lines represent the utilization of the reference for comparison.

To check if our variation shows a better performance, we simulated a rate capability test for electrodes in a normal (lithium-metal electrode//Celgard separator//graphite electrode) half-cell setup with parameters of the reference model and VSM6. As can be seen in Figure 9 the VSM6 electrode performs significantly better compared to the reference model electrode. A diffusion limitation at a C-rate higher than 0.6 C can be observed. Nevertheless this is still superior to the 0.2 C limitation seen for the reference.

In future work, we will try to experimentally verify the findings regarding the impact of electrode structure on rate capability. At the moment, we still face problems of manufacturing the appropriate electrodes.

Conclusions

In this paper, we parametrized a P2D model with three distinctive particle sizes to account for relaxation process in a laboratory, multi-layer cell design for a graphite half-cell. Two in particle size different graphites were investigated and implemented. For reproducing the actual withdrawn capacity from each layer of the MLC, we introduced a coupling procedure that had not been shown before.

Within our model we saw that smaller particles equilibrate faster due to their higher surface to volume ratio. For a homogeneous utilization, liquid phase parameters such as porosity, tortuosity and the diffusion coefficient of the electrolyte showed a higher impact than e.g. solid phase diffusion.

During the variation studies carried out with the aid of the model, it was observed that smaller graphite particles are beneficial near the current collector and larger particles near the separator toward the counter electrode. Also a porosity increase from separator to current collector showed a better utilization as the hard to reach pores near the current collector present a larger reservoir for lithium-ions which postpones rate limitation toward higher C-rates (compare VSM1 and VSM2). The biggest improvement was achieved by reducing the
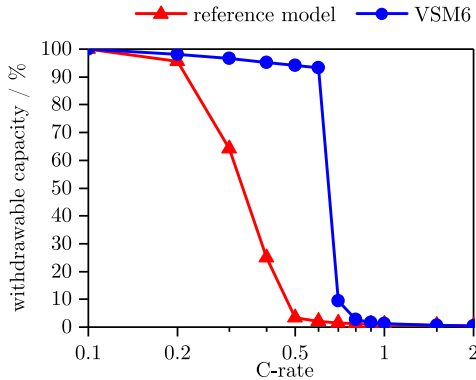
Figure 9. Comparison of reference and VSM6 electrode in a rate capability test. The withdrawable capacity is normalized to the capacity at 0.1 C. The sudden decrease in withdrawable capacity can be attributed to diffusion limitations in the electrolyte.

tortuosity overall and from separator to current collector (VSM3 to VSM5). The latter case could be implemented by including pore channels into the graphite electrode by means of laser beam structuring after the coating and calendering process during manufacturing.

In conclusion, the structuring of electrodes is a promising way to achieve a more homogeneous utilization in thick electrodes for high energy cells. The more homogeneous utilization during operation will lead to shorter equalization times and also to a more homogeneous aging behavior as that is largely caused by the current density distribution.

Appendix

Basics of P2D model.—The P2D model is based on porous electrode and concentrated solution theory and solves lithium-ion concentration c_i and potential Φ_i within the liquid electrolyte (subscript $i = l$) and the solid active material (subscript $i = s$) phase. The model geometry is defined as a one dimensional interval divided into two main domains corresponding to the separator and the graphite electrode. An additional dimension is set for the description of species intercalation within the particle domain. For a detailed model description, the reader is referred to Reference 27. The main equations are mass balance for lithium-ions in the electrolyte c_l

$$\varepsilon_l \frac{\partial c_l}{\partial t} = \nabla \left(D_{l,eff} \nabla c_l - \frac{i_l t_+}{F} \right) + a_s j_n \qquad [A1]$$

and charge balance

$$\nabla \left(-\kappa_{eff} \nabla \Phi_l + \frac{2\kappa_{eff} RT}{F} \left(1 + \frac{\partial \ln f_\pm}{\partial \ln c_l} \right) (1 - t_+) \nabla \ln c_l \right) = F a_s j_n \qquad [A2]$$

throughout the electrode domain. The current within the liquid phase is described by the current density i_l and potential Φ_l, while the pore wall flux at the electrode-electrolyte interface is named j_n. R describes the universal gas constant, F the Faraday's constant and T the local absolute temperature which is kept constant in this case. Within the separator domain the equations simplify to

$$\varepsilon_l \frac{\partial c_l}{\partial t} = \nabla \left(D_{l,eff} \nabla c_l - \frac{i_l t_+}{F} \right) \qquad [A3]$$

and

$$\nabla \left(-\kappa_{eff} \nabla \Phi_l + \frac{2\kappa_{eff} RT}{F} \left(1 + \frac{\partial \ln f_\pm}{\partial \ln c_l} \right) (1 - t_+) \nabla \ln c_l \right) = 0 \qquad [A4]$$

To couple solid and liquid phase, Butler-Volmer kinetics are assumed for the pore wall flux

$$j_n = k_c^{\alpha_a} k_a^{\alpha_c} \left(c_{s,max} - c_s|_{r=r_p} \right)^{\alpha_a} \left(c_s|_{r=r_p} \right)^{\alpha_c} \left(\frac{c_l}{1 \text{ mol m}^{-3}} \right)^{\alpha_a} \left(e^{\frac{\alpha_a F}{RT} \eta} - e^{-\frac{\alpha_c F}{RT} \eta} \right) \qquad [A5]$$

including the lithium-ion concentration at the particle's surface c_s and the overpotential

$$\eta = \Phi_s - \Phi_l - E_{Eq} \qquad [A6]$$

where Φ_s corresponds to the solid phase potential.

Effective transport parameters are used to account for tortuosity in the homogenized P2D model by scaling material parameters with a function of porosity ε_l and tortuosity τ [40]

$$\Psi_{l,eff} = \frac{\varepsilon_l}{\tau} \Psi_l \qquad [A7]$$

To describe the electrolyte's characteristics properly, a concentration dependence is implemented for conductivity, diffusivity and mean molar activity coefficient of the electrolyte. These are taken from fittings to measurements[41] while presuming a constant transport number. The applied diffusion coefficients are estimated from various literature sources.[26,27,30,42] The equilibrium potential is taken from literature[42] as well as the maximum concentration of lithium within the active material particles.[42,43] Additional parameters such as reaction rate constants[30,42] are assumed based on references from literature. The chosen parameters measured or taken from literature are summarized in Table AI and AII.

Table AI. Physicochemical parameters for the two graphites. Superscript *m* indicates measured values and superscript *e* values estimated from literature.

Parameter	SG	LG
Geometry		
Solid phase fraction ε_s	0.15 [m]	0.62 [m]
Liquid phase fraction ε_l	0.79 [m]	0.3 [m]
Tortuosity τ	3.7 [m]	5.4 [m]
Thermodynamics		
Equilibrium voltage $E_{Eq,neg}$	*analytic term*[42]; see Equation A8	
Maximum lithium concentration $c_{s,max}$	30555 mol/m^{3e}	30555 mol/m^{3e}
Initial state of charge $\frac{c_{s,0}}{c_{s,max}}$	0.75 [e]	0.7 [e]
Kinetics		
Reaction rate constant $k_{a,c}$	4×10^{-11} m/s [e]	2×10^{-11} m/s [e]
Anodic charge-transfer coefficient α_a	0.5 [e]	0.5 [e]
Cathodic charge-transfer coefficient α_c	0.5 [e]	0.5 [e]
Transport		
Solid diffusivity D_s	3.9×10^{-14} m^2/s [e]	3.9×10^{-14} m^2/s [e]
Solid conductivity σ	100 S/m [e]	100 S/m [e]
SEI resistance R_{SEI}	0.001 Ω^2m [e]	0.001 Ω^2m [e]

Table AII. Additional model parameters applicable for both graphites.

Parameter	Value
Electrolyte	
Electrolyte diffusivity D_l	*analytic term*[41]; see equation A9
Electrolyte conductivity κ	*analytic term*[41]; see equation A10
Activity dependency $\frac{\partial \ln f_\pm}{\partial \ln c_l}$	*analytic term*[41]; see equation A11
Transport number t_+	0.363[41]
Separator	
Celgard separator thickness $l_{\text{sep},1}$	25 μm
Celgard separator porosity $\varepsilon_{\text{Celgard}}$	0.39[23]
Celgard separator tortuosity τ_{Celgard}	4.1[23]
Glass fiber separator thickness $l_{\text{sep},2}$	260 μm
Glass fiber separator porosity ε_{GF}	0.6 ^{m}
Glass fiber separator tortuosity τ_{GF}	2.7 ^{m}
Additional	
Temperature T	25 °C

Equilibrium voltage curve for graphite as a function of lithiation degree x. The original definition by Safari et al.[42] is increased by 5 mV to agree with our graphite measurements.

$$E_{\text{Eq,neg}} = 0.6379 + (0.5416 \exp(-305.5309x)) + 0.044 \tanh\left(\frac{-x + 0.1958}{0.1088}\right)$$

$$- 0.1978 \tanh\left(\frac{x - 1.0571}{0.0854}\right) - 0.6875 \tanh\left(\frac{x + 0.0117}{0.0529}\right)$$

$$- 0.0175 \tanh\left(\frac{x - 0.5692}{0.0875}\right) \quad [A8]$$

Analytical dependencies for electrolyte diffusivity D_l, conductivity κ and activity $\frac{\partial \ln f_\pm}{\partial \ln c_l}$ as functions of temperature T, lithium-ion concentration in the liquid phase c_l and transport number t_+ as measured by Valøen et al.[41] The electrolyte diffusivity was scaled to 0.3 as the used electrolyte had a lower diffusivity compared to the one used by Valøen which is still in the order of known diffusivity values.[44]

$$D_l = 0.3 \times \left(10^{-4.43 - \frac{54}{T - (229 + 5c_l)} - 0.22c_l} \times 10^{-4} \right) \quad [A9]$$

$$\kappa = 0.1c_l \Big(-10.5 + 0.074T - 6.96 \times 10^{-2}T^2 + 0.668c_l - 0.0178c_lT$$

$$+ 2.8 \times 10^{-5}c_lT^2 + 0.494c_l^2 - 8.86 \times 10^{-4}c_l^2T \Big)^2 \quad [A10]$$

$$\frac{\partial \ln f_\pm}{\partial \ln c_l} = \frac{0.601 - 0.24c_l^{0.5} + 0.982c_l^{1.5}(1 - 0.0052(T - 294))}{1 - t_+} - 1 \quad [A11]$$

References

1. B. Scrosati and J. Garche, *Journal of Power Sources*, **195**, 2419 (2010).
2. A. E. Trippe, R. Arunachala, T. Massier, A. Jossen, and T. Hamacher, *IEEE PES Innovative Smart Grid Technologies Conference Europe*, 1 (2014).
3. Tesla, Supercharger. 2017; https://www.tesla.com/supercharger.
4. G. Zhang, C. E. Shaffer, C.-Y. Wang, and C. D. Rahn, *Journal of the Electrochemical Society*, **160**, A610 (2013).
5. P. J. Osswald, S. V. Erhard, J. Wilhelm, H. E. Hoster, and A. Jossen, *Journal of the Electrochemical Society*, **162**, A2099 (2015).
6. P. J. Osswald, S. V. Erhard, A. Rheinfeld, B. Rieger, H. E. Hoster, and A. Jossen, *Journal of Power Sources*, **329**, 546 (2016).
7. S. J. Harris and P. Lu, *The Journal of Physical Chemistry C*, **117**, 6481 (2013).
8. S. J. Harris, A. Timmons, D. R. Baker, and C. W. Monroe, *Chemical Physics Letters*, **485**, 265 (2010).
9. K. Kitada, H. Murayama, K. Fukuda, H. Arai, Y. Uchimoto, Z. Ogumi, and E. Matsubara, *Journal of Power Sources*, **301**, 11 (2016).
10. H. Abe, H. Kubota, M. Nemoto, Y. Masuda, Y. Tanaka, H. Munakata, and K. Kanamura, *Journal of Power Sources*, **334**, 78 (2016).
11. H. Tanida, H. Yamashige, Y. Orikasa, Y. Gogyo, H. Arai, Y. Uchimoto, and Z. Ogumi, *The Journal of Physical Chemistry C*, **120**, 4739 (2016).
12. S. V. Erhard, P. J. Osswald, J. Wilhelm, A. Rheinfeld, S. Kosch, and A. Jossen, *Journal of the Electrochemical Society*, **162**, A2707 (2015).
13. S. V. Erhard et al., *Journal of the Electrochemical Society*, **164**, A6324 (2017).
14. V. Zinth, C. von Lüders, M. Hofmann, J. Hattendorff, I. Buchberger, S. V. Erhard, J. Rebelo-Kornmeier, A. Jossen, and R. Gilles, *Journal of Power Sources*, **271**, 152 (2014).
15. C. von Lüders, V. Zinth, S. V. Erhard, P. J. Osswald, M. Hofmann, R. Gilles, and A. Jossen, *Journal of Power Sources*, **342**, 17 (2017).
16. B. Rieger, S. F. Schuster, S. V. Erhard, P. J. Osswald, A. Rheinfeld, C. Willmann, and A. Jossen, *Journal of Energy Storage*, **8**, 1 (2016).
17. F. M. Kindermann, A. Noel, S. V. Erhard, and A. Jossen, *Electrochimica Acta*, **185**, 107 (2015).
18. F. M. Kindermann, P. J. Osswald, S. Klink, G. Ehlert, J. Schuster, A. Noel, S. V. Erhard, W. Schuhmann, and A. Jossen, *Journal of Power Sources*, **342**, 638 (2017).
19. F. La Mantia, Characterization of Electrodes for Lithium-Ion Batteries through Electrochemical Impedance Spectroscopy and Mass Spectrometry: Nr. 17848. Ph.D. thesis, ETH Zürich, Zürich, 2008.
20. S.-H. Ng, F. La Mantia, and P. Novák, *Angewandte Chemie (International edition)*, **48**, 528 (2009).
21. S. Klink, W. Schuhmann, and F. La Mantia, *ChemSusChem*, **7**, 2159 (2014).
22. S. Klink, P. Weide, M. Muhler, W. Schuhmann, and F. La Mantia, *ECS Transactions*, **62**, 265 (2014).
23. J. Landesfeind, A. Ehrl, M. Graf, W. A. Wall, and H. A. Gasteiger, *Journal of the Electrochemical Society*, **163**, A1254 (2016).
24. J. S. Newman and C. W. Tobias, *Journal of the Electrochemical Society*, **109**, 1183 (1962).
25. J. S. Newman and K. E. Thomas-Alyea, *Electrochemical systems*, 3rd ed.; Wiley-Interscience: Hoboken, NJ, 2004.
26. C. M. Doyle, T. F. Fuller, and J. S. Newman, *Journal of the Electrochemical Society*, **140**, 1526 (1993).
27. T. F. Fuller, C. M. Doyle, and J. S. Newman, *Journal of the Electrochemical Society*, **141**, 982 (1994).
28. T. R. Ashwin, Y. M. Chung, and J. Wang, *Journal of Power Sources*, **328**, 586 (2016).
29. M. Ecker, T. K. D. Tran, P. Dechent, S. Käbitz, A. Warnecke, and D. U. Sauer, *Journal of the Electrochemical Society*, **162**, A1836 (2015).
30. S. G. Stewart, V. Srinivasan, and J. S. Newman, *Journal of the Electrochemical Society*, **155**, A664 (2008).
31. A. Jokar, B. Rajabloo, M. Désilets, and M. Lacroix, *Journal of the Electrochemical Society*, **163**, A2876 (2016).
32. G. S. Nagarajan, J. W. van Zee, and R. M. Spotnitz, *Journal of the Electrochemical Society*, **145**, 771 (1998).
33. Z. Mao, M. Farkhondeh, M. Pritzker, M. Fowler, and Z. Chen, *Journal of the Electrochemical Society*, **163**, A458 (2015).
34. P. Albertus, J. Christensen, and J. S. Newman, *Journal of the Electrochemical Society*, **156**, A606 (2009).
35. M. Ender, *Journal of Power Sources*, **282**, 572 (2015).
36. R. B. Darling and J. S. Newman, *Journal of the Electrochemical Society*, **144**, 4201 (1997).
37. J. Wilhelm, S. V. Erhard, I. Buchberger, and A. Jossen, Simulation of Lithium-Ion Battery Equalization Effects. ModVal 13. 2016.
38. K. G. Gallagher, S. E. Trask, C. Bauer, T. Woehrle, S. F. Lux, M. Tschech, P. Lamp, B. J. Polzin, S. Ha, B. Long, Q. Wu, W. Lu, D. W. Dees, and A. N. Jansen, *Journal of the Electrochemical Society*, **163**, A138 (2016).
39. C.-J. Bae, C. K. Erdonmez, J. W. Halloran, and Y.-M. Chiang, *Advanced materials*, **25**, 1254 (2013).
40. M. J. Martínez-Rodríguez, S. Shimpalee, and J. W. Van Zee, *Journal of the Electrochemical Society*, **156**, B80. (2009).
41. L. O. Valøen and J. N. Reimers, *Journal of the Electrochemical Society*, **152**, A882 (2005).
42. M. Safari and C. Delacourt, *Journal of the Electrochemical Society*, **158**, A562 (2011).
43. P. Ramadass, B. S. Haran, P. M. Gomadam, R. E. White, and B. N. Popov, *Journal of the Electrochemical Society*, **151**, A196 (2004).
44. M. Guo and R. E. White, *Journal of Power Sources*, **221**, 334 (2013).

5 Conclusion

As the SEI is perhaps the most important component in a lithium-ion battery, this thesis studied the current density distribution in graphite anodes and the subsequent implications on the SEI formation at the particles' surface. From a literature review on many aspects regarding the SEI, an overview of the mainly formed components on different anode materials and the conceptual basics of SEI formation was given. The formed products on lithium-metal, carbon and lithium alloy anodes are very similar and the influence of the electrolyte composition has to be acknowledged. Besides the anodic SEI, an interphase on the cathode is often detected. Measurement methods are still under development to get a profound picture of the SEI without altering its composition during the measurement.

A further screening of the literature revealed that SEI formation depends on cell-dependent variables as well as process variables in the formation process. The first kind includes all components of the electrolyte, the electrodes and also the separator. As a result, it was shown that the choice of using a certain system – being comprised of a specific electrolyte mixture, a composition of the anode as well as the cathode and a separator – already predetermines the SEI evolution. The process variables beginning with the filling of the electrolyte and then applying charging as well as temperature profiles has then only a partial influence on the further SEI growth. As the interdependencies between the different components rely on statistical experiments, manufacturers try to keep their formulations and resulting formation regimes proprietary.

To investigate the spatial evolution of SEI growth over the lifetime of a cell, a capacity fade model considering a loss of lithium-ion inventory due to SEI growth and a loss of active material was introduced. The chosen model was of a P2D class as those models are the state of the art for describing cell behavior over many cycles with physically based resolution. The model that was validated by comparison with a previously published aging study by Ecker et al.[175] considered the SEI with a separated electronic and ionic conductivity for the first time. This approach offers the opportunity to describe different behaviors of capacity and power fade for different cell chemistries. By running the model in a calendar aging mode, the side reaction exchange current density could be determined with temperature dependency. An experimental C-rate factor accounts for the re-formation of SEI after cracking due to graphite intercalation expansion. The non-linear aging behavior of the modeled NCM/graphite cell is emulated by a cathode transition-metal dissolution that reverses the limitation of the cell from an anode limitation to a cathode limitation. A crucial point that emerged during the capacity fade studies was the distribution of the SEI throughout the electrode. It was observed that the SEI after 1000 cycles was more than two times thicker (~600 nm to ~250 nm) near the separator compared to near the current collector. This can be ascribed to an inhomogeneous current density distribution through the electrode thickness.

When studying EIS as a method to determine formation quality, the same current density inhomogeneities were causing long-term relaxation phenomena that can be explained by a hypothesis considering three intra-electrode equilibration effects. EIS is, therefore, a useful qualitative measurement method to determine whether a cell is equilibrated. The observed equilibration effect (I) is due to the

radially inhomogeneous lithium-ion distribution within graphite particles, whereas effect (II) and (III) consider a balancing effect between differently lithiated particles spatially through (II) and along (III) the electrode. As seen in the impedance measurements the equilibration effects can take up to 48 h. To substantiate the hypothesis, a multiple working electrode cell developed by Klink et al.[200] – called MLC – was used to investigate effects (I) and (II) in a three layer graphite electrode setup. With the setup, the charge going in and out of each of the three graphite mesh electrodes which were electronically separated was measured by a separate potentiostat. When interrupting the current, the potential of each electrode could be measured versus the lithium counter electrode. Intra-particle equilibration effects could be observed for up to 4 h after a 2 h delithiation process. By shorting the electrodes after that relaxation period, a equilibration between the layers (effect (II)) could be observed over 40 h.

The experiments with the MLC were conducted with two different graphites whose distinct particle radii were apart approximately by a factor of ten. With the collected data, another P2D model was implemented to study the influences of liquid and solid phase parameters on the current density distribution through the electrode. The model incorporated a particle size distribution and the MLC electrode setup was realized with a new coupling procedure. Studies of the influencing parameters showed that the current density distribution is mainly controlled by liquid phase diffusion limitations. The effective diffusion is described by the diffusion coefficient of the electrolyte as well as the porosity and tortuosity of the electrode. For design implications, only the latter two parameters can be adjusted. By a design variation study with the MLC model it was found that increasing the porosity from separator to current collector had a beneficial effect. Lowering the tortuosity close to the separator and an average porosity of 50 % showed the most homogeneous utilization in this study. This could be realized as a structuring of a coated electrode with e.g. a laser beam to include pore channels in the electrode during manufacturing. The resulting electrode from that study had a total thickness of 196 µm and performed noticeably better in a rate capability test than an electrode with commercial porosity and tortuosity values of the same capacity that was 132 µm thick.

5.1 Incorporating new electrode design into aging model

Revisiting the main goal of this thesis – to derive requirements for an electrode design that ensures a homogeneous SEI growth through the electrode over the lifetime of a cell to decrease the overall capacity fade – the aging model from Section 3.3 and the improved electrode design from Section 4.5 need to be combined to accomplish that goal. Therefore, the structured electrode design from the variation studies is implemented in the aging model to investigate the aging behavior of the new electrode design.

Figure 5.1 shows the comparison of the SEI thickness evolution over 1000 cycles for the unstructured reference aging model (blue lines) and the adapted model with the structured negative electrode (red lines). Close to the current collector (dashed lines) the growth of the SEI is approximately the same for both models with about 250 nm. Near the separator (solid lines), the SEI thickness decreased from approximately 600 nm after 1000 cycles to only about 400 nm. This can be attributed to the more homogeneous liquid phase lithium-ion concentration and the subsequent more homogeneous current density distribution for the intercalation as well as side reaction during each cycle.

The more homogeneous SEI growth through the thickness of the electrode has, therefore, been achieved by the structured electrode design. The consequences for the overall capacity fade are depicted in
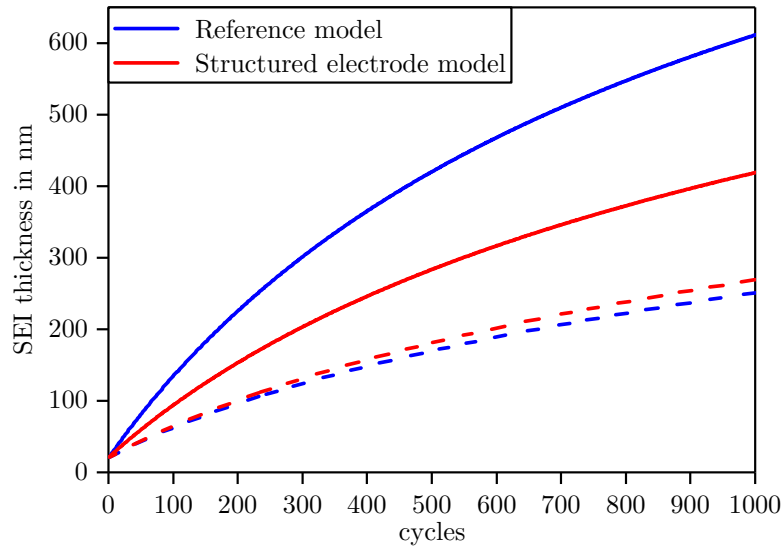
Figure 5.1: Comparison of SEI thickness close to the separator (solid lines) and close to the current collector (dashed lines) for 1000 cycles.

Figure 5.2. It has to be noted that the cathode dissolution reaction has been deactivated for the simulations in this chapter, as that aging effect would dominate the overall capacity fade after 450 cycles and the differences by SEI induced capacity fade would not be clearly distinguishable.

When comparing the capacity loss of the reference aging model and the modified electrode model in Figure 5.2, the capacity progression looks very similar. After 1000 cycles the structured electrode model retains about 3 % more capacity than the reference model. By looking at the cycle number at which the respective cell reaches the criterion of 80 % remaining capacity, almost 100 cycles more can be achieved with the structured electrode.
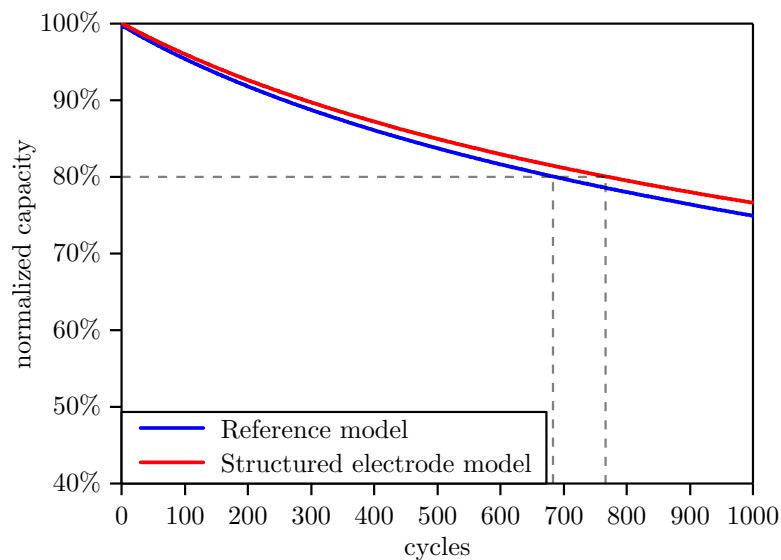

Figure 5.2: Capacity progression of the reference aging model (blue) compared to the aging model with an MLC modified electrode (green).

From the previously shown results, it can be concluded that the improvements gained from the MLC variation studies have a beneficial effect in the aging behavior of lithium-ion cell electrodes. The

structuring of the negative electrode is, therefore, predicted to be a novel electrode design that ensures a more homogeneous SEI growth and decreased capacity fade.

5.2 Possible future research tasks

Based on the presented findings regarding a more homogeneous aging behavior of lithium-ion batteries, several consecutive research tasks can be derived. This suggested future work is divided into questions regarding the structuring of electrodes and following questions from the aging model.

As laser beam structuring is still in a laboratory stage, experimental work should try to manufacture structured electrodes to verify the findings in an actual lithium-ion cell. Besides incorporating those electrodes in laboratory pouch cells, also mesh electrodes for the MLC setup could be improved to gain more insight in the resulting charge distribution.

Additionally, simulation experiments need to find an optimum for the parameters of the pore channels in the structured electrodes. The homogenization of the P2D model can only give an estimate on the overall cell behavior via the structured electrode model, whereas a 3D model seems to be adequate for defining pore channel number, distribution, depth as well as diameter.

In case of the aging model, additional knowledge on the particle size distribution contributions to the aging behavior are needed. The aging model can also serve as a base for implementing new aging effects such as lithium-plating or incorporation of transition-metals in the anodic SEI to get a better understanding for the interdependencies of the different aging mechanisms. With advances in understanding and uncovering the SEI formation process, the model can also be extended to reproduce the actual formation process during the first cycle.

References

1. Winter, M.: *The Solid Electrolyte Interphase – The Most Important and the Least Understood Solid Electrolyte in Rechargeable Li Batteries*, in: *Zeitschrift für physikalische Chemie 223*, pp. 1395–1406, 2009

2. Verma, P.; Maire, P.; Novák, P.: *A review of the features and analyses of the solid electrolyte interphase in Li-ion batteries*, in: *Electrochimica Acta 55 (22)*, pp. 6332–6341, 2010

3. Peled, E.: *The Electrochemical Behavior of Alkali and Alkaline Earth Metals in Nonaqueous Battery Systems - The Solid Electrolyte Interphase Model*, in: *Journal of The Electrochemical Society 126 (12)*, pp. 2047–2051, 1979

4. Xu, K.: *Nonaqueous Liquid Electrolytes for Lithium-Based Rechargeable Batteries*, in: *Chemical Reviews 104 (10)*, pp. 4303–4418, 2004

5. Tarascon, J.-M.: *The Li-Ion Battery: 25 Years of Exciting and Enriching Experiences*, in: *Electrochemical Society Interface 25 (3)*, pp. 79–83, 2016

6. Web of Science Core Collection: *Search History - TOPIC: (SEI) or TOPIC: ("solid electrolyte interphase") or TOPIC: ("solid electrolyte interface")*, URL: http://apps.webofknowledge.com, log-date: 2017-07-12

7. Dunn, B.; Kamath, H.; Tarascon, J.-M.: *Electrical Energy Storage for the Grid - A Battery of Choices*, in: *Science 334 (6058)*, pp. 928–935, 2011

8. Armstrong, M.J.; O'Dwyer, C.; Macklin, W.J.; Holmes, J.D.: *Evaluating the performance of nanostructured materials as lithium-ion battery electrodes*, in: *Nano Research 7 (1)*, pp. 1–62, 2014

9. Zhang, Z.; Zhang, S.S.: *Challenges of Key Materials for Rechargeable Batteries*, in: Zhang, Z.; Zhang, S.S. (eds.): *Rechargeable batteries*, Springer, Cham, 2015

10. Xu, K.: *Electrolytes and Interphases in Li-Ion Batteries and Beyond*, in: *Chemical Reviews 114 (23)*, pp. 11503–11618, 2014

11. An, S.J.; Li, J.; Sheng, Y.; Daniel, C.; Wood, D.L.: *Long-Term Lithium-Ion Battery Performance Improvement via Ultraviolet Light Treatment of the Graphite Anode*, in: *Journal of The Electrochemical Society 163 (14)*, A2866–A2875, 2016

12. Collins, J.; Gourdin, G.; Foster, M.; Qu, D.: *Carbon surface functionalities and SEI formation during Li intercalation*, in: *Carbon 92*, pp. 193–244, 2015

13. Peled, E.; Menkin, S.: *Review—SEI: Past, Present and Future*, in: *Journal of The Electrochemical Society 164 (7)*, A1703–A1719, 2017

14. Hérold, A.: *Recherches sur les composes dinsertion du graphite*, in: *Bulletin de la Société Chimique de France (7-8)*, pp. 999–1012, 1955

15. Fong, R.; von Sacken, U.; Dahn, J.R.: *Studies of Lithium Intercalation into Carbons Using Nonaqueous Electrochemical Cells*, in: *Journal of The Electrochemical Society 137 (7)*, pp. 2009–2013, 1990

16. Yazami, R.: *Surface chemistry and lithium storage capability of the graphite–lithium electrode*, in: *Electrochimica Acta 45 (1-2)*, pp. 87–97, 1999

17. Besenhard, J.O.; Winter, M.; Yang, J.; Biberacher, W.: *Filming mechanism of lithium-carbon anodes in organic and inorganic electrolytes*, in: *Journal of Power Sources 54 (2)*, pp. 228–231, 1995

18. Lin, J.; Guo, J.; Liu, C.; Guo, H.: *Artificial solid electrolyte interphase with in-situ formed porosity for enhancing lithiation of silicon wafer*, in: *Journal of Power Sources 336*, pp. 401–407, 2016

19. Lee, J.G.; Kim, J.; Park, H.; Lee, J.B.; Ryu, J.H.; Kim, J.J.; Oh, S.M.: *A Calculation Model to Assess Two Irreversible Capacities Evolved in Silicon Negative Electrodes*, in: *Journal of The Electrochemical Society 162 (8)*, A1579–A1584, 2015

20. Moradabadi, A.; Bakhtiari, M.; Kaghazchi, P.: *Effect of Anode Composition on Solid Electrolyte Interphase Formation*, in: *Electrochimica Acta 213*, pp. 8–13, 2016

21. Goodenough, J.B.; Kim, Y.: *Challenges for Rechargeable Li Batteries*, in: *Chemistry of Materials 22 (3)*, pp. 587–603, 2010

22. Melot, B.C.; Tarascon, J.-M.: *Design and preparation of materials for advanced electrochemical storage*, in: *Accounts of Chemical Research 46 (5)*, pp. 1226–1238, 2013

23. Smith, A.J.; Burns, J.C.; Zhao, X.; Xiong, D.J.; Dahn, J.R.: *A High Precision Coulometry Study of the SEI Growth in Li/Graphite Cells*, in: *Journal of The Electrochemical Society 158 (5)*, A447–A452, 2011

24. Arora, P.; White, R.E.; Doyle, C.M.: *Mathematical Modeling of the Lithium Deposition Overcharge Reaction in Lithium-Ion Batteries Using Carbon-Based Negative Electrodes*, in: *Journal of The Electrochemical Society 146 (10)*, pp. 3543–3553, 1999

25. Bar-Tow, D.; Peled, E.; Burstein, L.: *A Study of Highly Oriented Pyrolytic Graphite as a Model for the Graphite Anode in Li-Ion Batteries*, in: *Journal of The Electrochemical Society 146 (3)*, pp. 824–832, 1999

26. Peled, E.; Golodnitsky, D.; Ardel, G.: *Advanced Model for Solid Electrolyte Interphase Electrodes in Liquid and Polymer Electrolytes*, in: *Journal of The Electrochemical Society 144 (8)*, pp. L208–L210, 1997

27. Richard, M.N.; Dahn, J.R.: *Accelerating Rate Calorimetry Study on the Thermal Stability of Lithium Intercalated Graphite in Electrolyte. I. Experimental*, in: *Journal of The Electrochemical Society 146 (6)*, pp. 2068–2077, 1999

28. Richard, M.N.; Dahn, J.R.: *Accelerating Rate Calorimetry Study on the Thermal Stability of Lithium Intercalated Graphite in Electrolyte. II. Modeling the Results and Predicting Differential Scanning Calorimeter Curves*, in: *Journal of The Electrochemical Society 146 (6)*, pp. 2078–2084, 1999

29. MacNeil, D.D.; Larcher, D.; Dahn, J.R.: *Comparison of the Reactivity of Various Carbon Electrode Materials with Electrolyte at Elevated Temperature*, in: *Journal of The Electrochemical Society 146 (10)*, pp. 3596–3602, 1999

30. Domi, Y.; Doi, T.; Nakagawa, H.; Yamanaka, T.; Abe, T.; Ogumi, Z.: *In Situ Raman Study on Reversible Structural Changes of Graphite Negative-Electrodes at High Potentials in $LiPF_6$-Based Electrolyte Solution*, in: *Journal of The Electrochemical Society 163 (10)*, A2435–A2440, 2016

31. Zhang, S.S.; Ding, M.S.; Xu, K.; Allen, J.; Jow, T.R.: *Understanding Solid Electrolyte Interface Film Formation on Graphite Electrodes*, in: *Electrochemical and Solid-State Letters 4 (12)*, A206–A208, 2001

32. El Ouatani, L.; Dedryvère, R.; Ledeuil, J.-B.; Siret, C.; Biensan, P.; Desbrières, J.; Gonbeau, D.: *Surface film formation on a carbonaceous electrode: Influence of the binder chemistry*, in: *Journal of Power Sources 189 (1)*, pp. 72–80, 2009

33. Tornheim, A.; Peebles, C.; Gilbert, J.A.; Sahore, R.; Garcia, J.C.; Bareño, J.; Iddir, H.; Liao, C.; Abraham, D.P.: *Evaluating electrolyte additives for lithium-ion cells: A new Figure of Merit approach*, in: *Journal of Power Sources 365*, pp. 201–209, 2017

34. Hu, L.; Tornheim, A.; Zhang, S.S.; Zhang, Z.: *Additives for Functional Electrolytes of Li-Ion Batteries*, in: Zhang, Z.; Zhang, S.S. (eds.): *Rechargeable batteries*, Springer, Cham, 2015

35. Deng, J.; Wagner, G.J.; Muller, R.P.: *Phase Field Modeling of Solid Electrolyte Interface Formation in Lithium Ion Batteries*, in: *Journal of The Electrochemical Society 160 (3)*, A487–A496, 2013

36. Liu, L.; Park, J.; Lin, X.; Sastry, A.M.; Lu, W.: *A thermal-electrochemical model that gives spatial-dependent growth of solid electrolyte interphase in a Li-ion battery*, in: *Journal of Power Sources 268*, pp. 482–490, 2014

37. Nie, M.; Chalasani, D.; Abraham, D.P.; Chen, Y.; Bose, A.; Lucht, B.L.: *Lithium Ion Battery Graphite Solid Electrolyte Interphase Revealed by Microscopy and Spectroscopy*, in: *The Journal of Physical Chemistry C 117 (3)*, pp. 1257–1267, 2013

38. Nie, M.; Abraham, D.P.; Seo, D.M.; Chen, Y.; Bose, A.; Lucht, B.L.: *Role of Solution Structure in Solid Electrolyte Interphase Formation on Graphite with LiPF₆ in Propylene Carbonate*, in: *The Journal of Physical Chemistry C 117 (48)*, pp. 25381–25389, 2013

39. Nie, M.; Lucht, B.L.: *Role of Lithium Salt on Solid Electrolyte Interface (SEI) Formation and Structure in Lithium Ion Batteries*, in: *Journal of The Electrochemical Society 161 (6)*, A1001–A1006, 2014

40. Peled, E.; Golodnitsky, D.; Menachem, C.; Bar-Tow, D.: *An Advanced Tool for the Selection of Electrolyte Components for Rechargeable Lithium Batteries*, in: *Journal of The Electrochemical Society 145 (10)*, pp. 3482–3486, 1998

41. Edström, K.; Herstedt, M.; Abraham, D.P.: *A new look at the solid electrolyte interphase on graphite anodes in Li-ion batteries*, in: *Journal of Power Sources 153 (2)*, pp. 380–384, 2006

42. Aurbach, D.: *Electrode–solution interactions in Li-ion batteries: A short summary and new insights*, in: *Journal of Power Sources 119-121*, pp. 497–503, 2003

43. Aurbach, D.; Markovsky, B.; Weissman, I.; Levi, E.; Ein-Eli, Y.: *On the correlation between surface chemistry and performance of graphite negative electrodes for Li ion batteries*, in: *Electrochimica Acta 45 (1-2)*, pp. 67–86, 1999

44. Aurbach, D.; Ein-Eli, Y.; Chusid, O.; Carmeli, Y.; Babai, M.; Yamin, H.: *The Correlation Between the Surface Chemistry and the Performance of Li-Carbon Intercalation Anodes for Rechargeable 'Rocking-Chair' Type Batteries*, in: *Journal of The Electrochemical Society 141 (3)*, pp. 603–611, 1994

References

45. Aurbach, D.; Markovsky, B.; Shechter, A.; Ein-Eli, Y.; Cohen, H.: *A Comparative Study of Synthetic Graphite and Li Electrodes in Electrolyte Solutions Based on Ethylene Carbonate-Dimethyl Carbonate Mixtures*, in: *Journal of The Electrochemical Society 143 (12)*, pp. 3809–3820, 1996

46. Aurbach, D.; Daroux, M.L.; Faguy, P.W.; Yeager, E.: *Identification of Surface Films Formed on Lithium in Propylene Carbonate Solutions*, in: *Journal of The Electrochemical Society 134 (7)*, pp. 1611–1620, 1987

47. Zhuang, G.V.; Ross, P.N.: *Analysis of the Chemical Composition of the Passive Film on Li-Ion Battery Anodes Using Attenuated Total Reflection Infrared Spectroscopy*, in: *Electrochemical and Solid-State Letters 6 (7)*, A136–A139, 2003

48. Qian, Y.; Niehoff, P.; Börner, M.; Grützke, M.; Mönnighoff, X.; Behrends, P.; Nowak, S.; Winter, M.; Schappacher, F.M.: *Influence of electrolyte additives on the cathode electrolyte interphase (CEI) formation on $LiNi_{1/3}Mn_{1/3}Co_{1/3}O_2$ in half cells with Li metal counter electrode*, in: *Journal of Power Sources 329*, pp. 31–40, 2016

49. Friesen, A.; Mönnighoff, X.; Börner, M.; Haetge, J.; Schappacher, F.M.; Winter, M.: *Influence of temperature on the aging behavior of 18650-type lithium ion cells - A comprehensive approach combining electrochemical characterization and post-mortem analysis*, in: *Journal of Power Sources 342*, pp. 88–97, 2017

50. Kasnatscheew, J. et al.: *The truth about the 1st cycle Coulombic efficiency of $LiNi_{1/3}Co_{1/3}Mn_{1/3}O_2$ (NCM) cathodes*, in: *Physical chemistry chemical physics 18 (5)*, pp. 3956–3965, 2016

51. Edström, K.; Gustafsson, T.; Thomas, J.O.: *The cathode–electrolyte interface in the Li-ion battery*, in: *Electrochimica Acta 50 (2-3)*, pp. 397–403, 2004

52. Younesi, R.; Christiansen, A.S.; Scipioni, R.; Ngo, D.-T.; Simonsen, S.B.; Edström, K.; Hjelm, J.; Norby, P.: *Analysis of the Interphase on Carbon Black Formed in High Voltage Batteries*, in: *Journal of The Electrochemical Society 162 (7)*, A1289–A1296, 2015

53. Gauthier, M. et al.: *Electrode-electrolyte interface in Li-ion batteries: current understanding and new insights*, in: *The Journal of Physical Chemistry Letters 6 (22)*, pp. 4653–4672, 2015

54. Castaing, R.; Moreau, P.; Reynier, Y.; Schleich, D.; Jouanneau Si Larbi, S.; Guyomard, D.; Dupré, N.: *NMR quantitative analysis of solid electrolyte interphase on aged Li-ion battery electrodes*, in: *Electrochimica Acta 155*, pp. 391–395, 2015

55. Dedryvère, R.; Foix, D.; Franger, S.; Patoux, S.; Daniel, L.; Gonbeau, D.: *Electrode/Electrolyte Interface Reactivity in High-Voltage Spinel $LiMn_{1.6}Ni_{0.4}O_4/Li_4Ti_5O_{12}$ Lithium-Ion Battery*, in: *The Journal of Physical Chemistry C 114 (24)*, pp. 10999–11008, 2010

56. Waldmann, T. et al.: *Review - Post-Mortem Analysis of Aged Lithium-Ion Batteries: Disassembly Methodology and Physico-Chemical Analysis Techniques*, in: *Journal of The Electrochemical Society 163 (10)*, A2149–A2164, 2016

57. Cabana, J.: *Chapter 7 - Tools and Methodologies for Characterization of Electrode-Electrolyte Interfaces*, in: Jow, T.R.; Xu, K.; Borodin, O.; Ue, M. (eds.): *Electrolytes for lithium and lithium-ion batteries*, Springer, New York, 2014

58. Zhang, S.S.; Xu, K.; Jow, T.R.: *EIS study on the formation of solid electrolyte interface in Li-ion battery*, in: *Electrochimica Acta 51 (8-9)*, pp. 1636–1640, 2006

59. Cheng, X.-B.; Zhang, R.; Zhao, C.-Z.; Wei, F.; Zhang, J.-G.; Zhang, Q.: *A Review of Solid Electrolyte Interphases on Lithium Metal Anode*, in: *Advanced Science 3 (3)*, p. 1500213, 2016

60. Agubra, V.A.; Fergus, J.W.: *The formation and stability of the solid electrolyte interface on the graphite anode*, in: *Journal of Power Sources 268*, pp. 153–162, 2014

61. Boesenberg, U.; Fitschen, U.E.A.: *2D and 3D Imaging of Li-Ion Battery Materials Using Synchrotron Radiation Sources*, in: Zhang, Z.; Zhang, S.S. (eds.): *Rechargeable batteries*, Springer, Cham, 2015

62. Harks, P.; Mulder, F.M.; Notten, P.H.L.: *In situ methods for Li-ion battery research: A review of recent developments*, in: *Journal of Power Sources 288*, pp. 92–105, 2015

63. Zoski, C.G.: *Review—Advances in Scanning Electrochemical Microscopy (SECM)*, in: *Journal of The Electrochemical Society 163 (4)*, H3088–H3100, 2015

64. Sharma, N.; Wagemaker, M.: *Lithium-Ion Batteries*, in: Kearley, G.J.; Peterson, V.K. (eds.): *Neutron Applications in Materials for Energy*, Springer, Cham, 2015

65. Kren, H.: *About the Continuous Growth of the Solid Electrolyte Interphase in Lithium Ion Batteries*, Graz University of Technology, Graz, Austria, 2011

66. Marrocchelli, D.; Merlet, C.; Salanne, M.: *Molecular Dynamics Simulations of Electrochemical Energy Storage Devices*, in: Franco, A.A.; Doublet, M.L.; Bessler, W.G. (eds.): *Physical Multiscale Modeling and Numerical Simulation of Electrochemical Devices for Energy Conversion and Storage*, Springer, London, 2016

67. Lee, T.J. et al.: *Tris(pentafluorophenyl)silane as a Solid Electrolyte Interphase (SEI)-Forming Agent for Graphite Electrodes*, in: *Journal of The Electrochemical Society 164 (9)*, A1887–A1892, 2017

68. Ge, H.; Aoki, T.; Ikeda, N.; Suga, S.; Isobe, T.; Li, Z.; Tabuchi, Y.; Zhang, J.: *Investigating Lithium Plating in Lithium-Ion Batteries at Low Temperatures Using Electrochemical Model with NMR Assisted Parameterization*, in: *Journal of The Electrochemical Society 164 (6)*, A1050–A1060, 2017

69. Armand, M.; Tarascon, J.-M.: *Building better batteries*, in: *Nature 451 (7179)*, pp. 652–657, 2008

70. Scrosati, B.; Garche, J.: *Lithium batteries: Status, prospects and future*, in: *Journal of Power Sources 195 (9)*, pp. 2419–2430, 2010

71. Passerini, S.; Scrosati, B.: *Lithium and Lithium-Ion Batteries: Challenges and Prospects*, in: *Electrochemical Society Interface 25 (3)*, pp. 85–87, 2016

72. Arora, P.; White, R.E.; Doyle, C.M.: *Capacity Fade Mechanisms and Side Reactions in Lithium-Ion Batteries*, in: *Journal of The Electrochemical Society 145 (10)*, pp. 3647–3667, 1998

73. Christensen, J.; Newman, J.S.: *Cyclable Lithium and Capacity Loss in Li-Ion Cells*, in: *Journal of The Electrochemical Society 152 (4)*, A818–A829, 2005

74. Pieczonka, N.P.W.; Liu, Z.; Lu, P.; Olson, K.L.; Moote, J.; Powell, B.R.; Kim, J.-H.: *Understanding Transition-Metal Dissolution Behavior in $LiNi_{0.5}Mn_{1.5}O_4$ High-Voltage Spinel for Lithium Ion Batteries*, in: *The Journal of Physical Chemistry C 117 (31)*, pp. 15947–15957, 2013

75. Zhang, S.S.: *A review on electrolyte additives for lithium-ion batteries*, in: *Journal of Power Sources 162 (2)*, pp. 1379–1394, 2006

76. Jaini, R.R.; Setzler, B.P.; Star, A.G.; Fuller, T.F.: *Investigating the Solid Electrolyte Interphase Formed by Additive Reduction Using Physics-Based Modeling*, in: *Journal of The Electrochemical Society 163 (10)*, A2185–A2196, 2016

77. Aurbach, D.; Gamolsky, K.; Markovsky, B.; Gofer, Y.; Schmidt, M.; Heider, U.: *On the use of vinylene carbonate (VC) as an additive to electrolyte solutions for Li-ion batteries*, in: *Electrochimica Acta 47 (9)*, pp. 1423–1439, 2002

78. Forestier, C.; Grugeon, S.; Davoisne, C.; Lecocq, A.; Marlair, G.; Armand, M.; Sannier, L.; Laruelle, S.: *Graphite electrode thermal behavior and solid electrolyte interphase investigations - Role of state-of-the-art binders, carbonate additives and lithium bis(fluorosulfonyl)imide salt*, in: *Journal of Power Sources 330*, pp. 186–194, 2016

79. Xu, K.; von Cresce, A.; Lee, U.: *Differentiating contributions to "ion transfer" barrier from interphasial resistance and Li^+ desolvation at electrolyte/graphite interface*, in: *Langmuir 26 (13)*, pp. 11538–11543, 2010

80. He, Y.-B.; Liu, M.; Huang, Z.-D.; Zhang, B.; Yu, Y.; Li, B.; Kang, F.; Kim, J.-K.: *Effect of solid electrolyte interface (SEI) film on cyclic performance of $Li_4Ti_5O_{12}$ anodes for Li ion batteries*, in: *Journal of Power Sources 239*, pp. 269–276, 2013

81. Reale, P.; Fernicola, A.; Scrosati, B.: *Compatibility of the $Py_{24}TFSI$–$LiTFSI$ ionic liquid solution with $Li_4Ti_5O_{12}$ and $LiFePO_4$ lithium ion battery electrodes*, in: *Journal of Power Sources 194 (1)*, pp. 182–189, 2009

82. Laresgoiti, I.; Käbitz, S.; Ecker, M.; Sauer, D.U.: *Modeling mechanical degradation in lithium ion batteries during cycling - Solid electrolyte interphase fracture*, in: *Journal of Power Sources 300*, pp. 112–122, 2015

83. Petibon, R.; Chevrier, V.L.; Aiken, C.P.; Hall, D.S.; Hyatt, S.R.; Shunmugasundaram, R.; Dahn, J.R.: *Studies of the Capacity Fade Mechanisms of $LiCoO_2$/Si-Alloy - Graphite Cells*, in: *Journal of The Electrochemical Society 163 (7)*, A1146–A1156, 2016

84. Rieger, B.; Erhard, S.V.; Rumpf, K.; Jossen, A.: *A New Method to Model the Thickness Change of a Commercial Pouch Cell during Discharge*, in: *Journal of The Electrochemical Society 163 (8)*, A1566–A1575, 2016

85. Ohzuku, T.; Iwakoshi, Y.; Sawai, K.: *Formation of Lithium-Graphite Intercalation Compounds in Nonaqueous Electrolytes and Their Application as a Negative Electrode for a Lithium Ion (Shuttlecock) Cell*, in: *Journal of The Electrochemical Society 140 (9)*, pp. 2490–2498, 1993

86. Choi, W.; Manthiram, A.: *Comparison of Metal Ion Dissolutions from Lithium Ion Battery Cathodes*, in: *Journal of The Electrochemical Society 153 (9)*, A1760–A1764, 2006

87. Vortmann-Westhoven, B.; Winter, M.; Nowak, S.: *Where is the lithium? Quantitative determination of the lithium distribution in lithium ion battery cells: Investigations on the influence of the temperature, the C-rate and the cell type*, in: *Journal of Power Sources 346*, pp. 63–70, 2017

88. Bhandari, A.; Bhattacharya, J.: *Review—Manganese Dissolution from Spinel Cathode: Few Unanswered Questions*, in: *Journal of The Electrochemical Society 164 (2)*, A106–A127, 2017

89. Buchberger, I.; Seidlmayer, S.; Pokharel, A.; Piana, M.; Hattendorff, J.; Kudejova, P.; Gilles, R.; Gasteiger, H.A.: *Aging Analysis of Graphite/$LiNi_{1/3}Mn_{1/3}Co_{1/3}O_2$ Cells Using XRD, PGAA, and AC Impedance*, in: *Journal of The Electrochemical Society 162 (14)*, A2737–A2746, 2015

90. Shin, H.; Park, J.; Sastry, A.M.; Lu, W.: *Degradation of the solid electrolyte interphase induced by the deposition of manganese ions*, in: *Journal of Power Sources 284*, pp. 416–427, 2015

91. Darling, R.B.; Newman, J.S.: *Modeling a Porous Intercalation Electrode with Two Characteristic Particle Sizes*, in: *Journal of The Electrochemical Society 144 (12)*, pp. 4201–4208, 1997

92. Chen, C.-F.; Barai, P.; Smith, K.A.; Mukherjee, P.P.: *Scaling Relations for Intercalation Induced Damage in Electrodes*, in: *Electrochimica Acta 204*, pp. 31–49, 2016

93. Ebner, M.; Chung, D.-W.; García, R.E.; Wood, V.: *Tortuosity Anisotropy in Lithium-Ion Battery Electrodes*, in: *Advanced Energy Materials 4 (5)*, p. 1301278, 2014

94. Cericola, D.; Spahr, M.E.: *Impedance Spectroscopic Studies of the Porous Structure of Electrodes containing Graphite Materials with Different Particle Size and Shape*, in: *Electrochimica Acta 191*, pp. 558–566, 2016

95. Tang, M.H.-M.; Albertus, P.; Newman, J.S.: *Two-Dimensional Modeling of Lithium Deposition during Cell Charging*, in: *Journal of The Electrochemical Society 156 (5)*, A390–A399, 2009

96. Dai, Y.; Cai, L.; White, R.E.: *Simulation and Analysis of Inhomogeneous Degradation in Large Format $LiMn_2O_4$/Carbon Cells*, in: *Journal of The Electrochemical Society 161 (8)*, E3348–E3356, 2014

97. Kleiner, K.; Jakes, P.; Scharner, S.; Liebau, V.; Ehrenberg, H.: *Changes of the balancing between anode and cathode due to fatigue in commercial lithium-ion cells*, in: *Journal of Power Sources 317*, pp. 25–34, 2016

98. Singh, M.; Kaiser, J.; Hahn, H.: *Thick Electrodes for High Energy Lithium Ion Batteries*, in: *Journal of The Electrochemical Society 162 (7)*, A1196–A1201, 2015

99. Gallagher, K.G. et al.: *Optimizing Areal Capacities through Understanding the Limitations of Lithium-Ion Electrodes*, in: *Journal of The Electrochemical Society 163 (2)*, A138–A149, 2016

100. Du, Z.; Rollag, K.M.; Li, J.; An, S.J.; Wood, M.; Sheng, Y.; Mukherjee, P.P.; Daniel, C.; Wood, D.L.: *Enabling aqueous processing for crack-free thick electrodes*, in: *Journal of Power Sources 354*, pp. 200–206, 2017

101. Yang, G.-F.; Joo, S.-K.: *Calendering effect on the electrochemical performances of the thick Li-ion battery electrodes using a three dimensional Ni alloy foam current collector*, in: *Electrochimica Acta 170*, pp. 263–268, 2015

102. Müller, M.; Pfaffmann, L.; Jaiser, S.; Baunach, M.; Trouillet, V.; Scheiba, F.; Scharfer, P.; Schabel, W.; Bauer, W.: *Investigation of binder distribution in graphite anodes for lithium-ion batteries*, in: *Journal of Power Sources 340*, pp. 1–5, 2017

103. Dedryvère, R.; Martinez, H.; Leroy, S.; Lemordant, D.; Bonhomme, F.; Biensan, P.; Gonbeau, D.: *Surface film formation on electrodes in a $LiCoO_2$/graphite cell: A step by step XPS study*, in: *Journal of Power Sources 174 (2)*, pp. 462–468, 2007

104. Shi, Q.; Liu, W.; Qu, Q.; Gao, T.; Wang, Y.; Liu, G.; Battaglia, V.S.; Zheng, H.: *Robust solid/electrolyte interphase on graphite anode to suppress lithium inventory loss in lithium-ion batteries*, in: *Carbon 111*, pp. 291–298, 2017

105. Ding, M.S.; Koch, S.L.; Passerini, S.: *The Effect of 1-Pentylamine as Solid Electrolyte Interphase Precursor on Lithium Metal Anodes*, in: *Electrochimica Acta 240*, pp. 408–414, 2017

106. Zhang, S.S.: *A review on the separators of liquid electrolyte Li-ion batteries*, in: *Journal of Power Sources 164 (1)*, pp. 351–364, 2007

107. Lee, H.; Yanilmaz, M.; Toprakci, O.; Fu, K.; Zhang, X.: *A review of recent developments in membrane separators for rechargeable lithium-ion batteries*, in: *Energy Environmental Science 7 (12)*, pp. 3857–3886, 2014

108. Arora, P.; Zhang, Z.: *Battery Separators*, in: *Chemical Reviews 104 (10)*, pp. 4419–4462, 2004

109. Miranda, D.; Costa, C.M.; Almeida, A.M.; Lanceros-Méndez, S.: *Modeling separator membranes physical characteristics for optimized lithium ion battery performance*, in: *Solid State Ionics 278*, pp. 78–84, 2015

110. Zhong, Q.; von Sacken, U.: *Low viscosity electrolyte comprising P205 for use in non-aqueous rechargable lithium batteries, US005650245A (5,650,245)*, 1997

111. Taskier, H.T.: *Hydrophilic polymer coated microporous membranes capable of use as a battery separator (US4359510A)*, 1982

112. Knoche, T.; Zinth, V.; Schulz, M.; Schnell, J.; Gilles, R.; Reinhart, G.: *In situ visualization of the electrolyte solvent filling process by neutron radiography*, in: *Journal of Power Sources 331*, pp. 267–276, 2016

113. Wood, D.L.; Li, J.; Daniel, C.: *Prospects for reducing the processing cost of lithium ion batteries*, in: *Journal of Power Sources 275*, pp. 234–242, 2015

114. Tagawa, K.; Brodd, R.J.: *Production Processes for Fabrication of Lithium-Ion Batteries*, in: Yoshio, M.; Brodd, R.J.; Kozawa, A. (eds.): *Lithium-ion batteries*, Springer, New York, NY, 2009

115. Knoche, T.; Surek, F.; Reinhart, G.: *A Process Model for the Electrolyte Filling of Lithium-ion Batteries*, in: *Procedia CIRP 41*, pp. 405–410, 2016

116. Yoon, S.-Y.; Iocco, R.: *Split Charge Forming Process for Battery (US20100192362 A1)*, 2010

117. Zhao, M.; Kariuki, S.; Dewald, H.D.; Lemke, F.R.; Staniewicz, R.J.; Plichta, E.J.; Marsh, R.A.: *Electrochemical Stability of Copper in Lithium-Ion Battery Electrolytes*, in: *Journal of The Electrochemical Society 147 (8)*, pp. 2874–2879, 2000

118. Crompton, K.R.; Landi, B.J.: *Opportunities for near zero volt storage of lithium ion batteries*, in: *Energy Environmental Science 9 (7)*, pp. 2219–2239, 2016

119. Lux, S.; Bruch, M.; Vetter, M.: *Formation of Lithium-ion Batteries*, München, 10.06.2015

120. Gering, K.L.; Einerson, J.J.: *Statistical Design of Experiment for Li-ion Cell Formation Parameters using "Gen3" Electrode Materials: Final Summary*, Arlington, VA, 19.05.2009

121. Bhattacharya, S.; Alpas, A.T.: *Micromechanisms of solid electrolyte interphase formation on electrochemically cycled graphite electrodes in lithium-ion cells*, in: *Carbon 50 (15)*, pp. 5359–5371, 2012

122. Lee, H.-H.; Wang, Y.-Y.; Wan, C.-C.; Yang, M.-H.; Wu, H.-C.; Shieh, D.-T.: *A fast formation process for lithium batteries*, in: *Journal of Power Sources 134 (1)*, pp. 118–123, 2004

123. An, S.J.; Li, J.; Du, Z.; Daniel, C.; Wood, D.L.: *Fast formation cycling for lithium ion batteries*, in: *Journal of Power Sources 342*, pp. 846–852, 2017

124. He, Y.-B.; Tang, Z.-Y.; Song, Q.-S.; Xie, H.; Liu, Y.-G.; Xu, Q.: *Effects of Temperature on the Formation of Graphite/LiCoO$_2$ Batteries*, in: *Journal of The Electrochemical Society 155 (7)*, A481–A487, 2008

125. German, F.; Hintennach, A.; LaCroix, A.; Thiemig, D.; Oswald, S.; Scheiba, F.; Hoffmann, M.J.; Ehrenberg, H.: *Influence of temperature and upper cut-off voltage on the formation of lithium-ion cells*, in: *Journal of Power Sources 264*, pp. 100–107, 2014

126. Aiken, C.P.; Self, J.; Petibon, R.; Xia, X.; Paulsen, J.M.; Dahn, J.R.: *A Survey of In Situ Gas Evolution during High Voltage Formation in Li-Ion Pouch Cells*, in: *Journal of The Electrochemical Society 162 (4)*, A760–A767, 2015

127. Albertus, P.; Christensen, J.; Newman, J.S.: *Experiments on and Modeling of Positive Electrodes with Multiple Active Materials for Lithium-Ion Batteries*, in: *Journal of The Electrochemical Society 156 (7)*, A606–A618, 2009

128. Delp, S.A.; Borodin, O.; Olguin, M.; Eisner, C.G.; Allen, J.L.; Jow, T.R.: *Importance of Reduction and Oxidation Stability of High Voltage Electrolytes and Additives*, in: *Electrochimica Acta 209*, pp. 498–510, 2016

129. Steinhauer, M.; Risse, S.; Wagner, N.; Friedrich, K.A.: *Investigation of the Solid Electrolyte Interphase Formation at Graphite Anodes in Lithium-Ion Batteries with Electrochemical Impedance Spectroscopy*, in: *Electrochimica Acta 228*, pp. 652–658, 2017

130. Markovsky, B.; Rodkin, A.; Cohen, Y.S.; Palchik, O.; Levi, E.; Aurbach, D.; Kim, H.-J.; Schmidt, M.: *The study of capacity fading processes of Li-ion batteries: major factors that play a role*, in: *Journal of Power Sources 119-121*, pp. 504–510, 2003

131. Spotnitz, R.M.: *Simulation of capacity fade in lithium-ion batteries*, in: *Journal of Power Sources 113 (1)*, pp. 72–80, 2003

132. Agubra, V.A.; Fergus, J.W.: *Lithium Ion Battery Anode Aging Mechanisms*, in: *Materials 6*, pp. 1310–1325, 2013

133. Aurbach, D.: *Review of selected electrode–solution interactions which determine the performance of Li and Li ion batteries*, in: *Journal of Power Sources 89 (2)*, pp. 206–218, 2000

134. Aurbach, D.; Markovsky, B.; Salitra, G.; Markevich, E.; Talyossef, Y.; Koltypin, M.; Nazar, L.F.; Ellis, B.; Kovacheva, D.: *Review on electrode–electrolyte solution interactions, related to cathode materials for Li-ion batteries*, in: *Journal of Power Sources 165 (2)*, pp. 491–499, 2007

135. Birkl, C.R.; Roberts, M.R.; McTurk, E.; Bruce, P.G.; Howey, D.A.: *Degradation diagnostics for lithium ion cells*, in: *Journal of Power Sources 341*, pp. 373–386, 2017

136. Broussely, M.; Biensan, P.; Bonhomme, F.; Blanchard, P.; Herreyre, S.; Nechev, K.; Staniewicz, R.J.: *Main aging mechanisms in Li ion batteries*, in: *Journal of Power Sources 146 (1-2)*, pp. 90–96, 2005

137. Vetter, J. et al.: *Ageing mechanisms in lithium-ion batteries*, in: *Journal of Power Sources 147 (1-2)*, pp. 269–281, 2005

138. Zhang, Q.; White, R.E.: *Capacity fade analysis of a lithium ion cell*, in: *Journal of Power Sources 179 (2)*, pp. 793–798, 2008

139. Han, X.; Ouyang, M.; Lu, L.; Li, J.; Zheng, Y.; Li, Z.: *A comparative study of commercial lithium ion battery cycle life in electrical vehicle - Aging mechanism identification*, in: *Journal of Power Sources 251*, pp. 38–54, 2014

140. Dubarry, M.; Truchot, C.; Liaw, B.Y.: *Synthesize battery degradation modes via a diagnostic and prognostic model*, in: *Journal of Power Sources 219*, pp. 204–216, 2012

141. Gilbert, J.A.; Shkrob, I.A.; Abraham, D.P.: *Transition Metal Dissolution, Ion Migration, Electrocatalytic Reduction and Capacity Loss in Lithium-Ion Full Cells*, in: *Journal of The Electrochemical Society 164 (2)*, A389–A399, 2017

142. Ramadesigan, V.; Northrop, Paul W. C.; De, S.; Santhanagopalan, S.; Braatz, R.D.; Subramanian, V.R.: *Modeling and Simulation of Lithium-Ion Batteries from a Systems Engineering Perspective*, in: *Journal of The Electrochemical Society 159 (3)*, R31–R45, 2012

143. Jokar, A.; Rajabloo, B.; Désilets, M.; Lacroix, M.: *Review of simplified Pseudo-two-Dimensional models of lithium-ion batteries*, in: *Journal of Power Sources 327*, pp. 44–55, 2016

144. Ganesh, P.; Kent, P.R.C.; Jiang, D.-e.: *Solid–Electrolyte Interphase Formation and Electrolyte Reduction at Li-Ion Battery Graphite Anodes: Insights from First-Principles Molecular Dynamics*, in: *The Journal of Physical Chemistry C 116 (46)*, pp. 24476–24481, 2012

145. Benitez, L.; Seminario, J.M.: *Ion Diffusivity through the Solid Electrolyte Interphase in Lithium-Ion Batteries*, in: *Journal of The Electrochemical Society 164 (11)*, E3159–E3170, 2017

146. Ogata, S.; Ohba, N.; Kouno, T.: *Multi-Thousand-Atom DFT Simulation of Li-Ion Transfer through the Boundary between the Solid–Electrolyte Interface and Liquid Electrolyte in a Li-Ion Battery*, in: *The Journal of Physical Chemistry C 117 (35)*, pp. 17960–17968, 2013

147. Zvereva, E.; Caliste, D.; Pochet, P.: *Interface identification of the solid electrolyte interphase on graphite*, in: *Carbon 111*, pp. 789–795, 2017

148. Saubanère, M.; Filhol, J.-S.; Doublet, M.L.: *Atomistic Modeling of Electrode Materials for Li-Ion Batteries: From Bulk to Interfaces*, in: Franco, A.A.; Doublet, M.L.; Bessler, W.G. (eds.): *Physical Multiscale Modeling and Numerical Simulation of Electrochemical Devices for Energy Conversion and Storage*, Springer, London, 2016

149. Hörmann, N.G.; Jäckle, M.; Gossenberger, F.; Roman, T.; Forster-Tonigold, K.; Naderian, M.; Sakong, S.; Groß, A.: *Some challenges in the first-principles modeling of structures and processes in electrochemical energy storage and transfer*, in: *Journal of Power Sources 275*, pp. 531–538, 2015

150. Ushirogata, K.; Sodeyama, K.; Futera, Z.; Tateyama, Y.; Okuno, Y.: *Near-Shore Aggregation Mechanism of Electrolyte Decomposition Products to Explain Solid Electrolyte Interphase Formation*, in: *Journal of The Electrochemical Society 162 (14)*, A2670–A2678, 2015

151. Newman, J.S.; Thomas-Alyea, K.E.: *Electrochemical systems*, 3rd edition, Wiley-Interscience, Hoboken, NJ, 2004

152. Fuller, T.F.; Doyle, C.M.; Newman, J.S.: *Relaxation Phenomena in Lithium-Ion-Insertion Cells*, in: *Journal of The Electrochemical Society 141 (4)*, pp. 982–990, 1994

153. Doyle, C.M.; Fuller, T.F.; Newman, J.S.: *Modeling of Galvanostatic Charge and Discharge of the Lithium/Polymer/Insertion Cell*, in: *Journal of The Electrochemical Society 140 (6)*, pp. 1526–1533, 1993

154. Zhang, D.; Popov, B.N.; White, R.E.: *Modeling Lithium Intercalation of a Single Spinel Particle under Potentiodynamic Control*, in: *Journal of The Electrochemical Society 147 (3)*, pp. 831–838, 2000

155. Newman, J.S.; Tobias, C.W.: *Theoretical Analysis of Current Distribution in Porous Electrodes*, in: *Journal of The Electrochemical Society 109 (12)*, pp. 1183–1191, 1962

156. Santhanagopalan, S.; Guo, Q.; Ramadass, P.; White, R.E.: *Review of models for predicting the cycling performance of lithium ion batteries*, in: *Journal of Power Sources 156 (2)*, pp. 620–628, 2006

157. Kang, L.; Zhao, X.; Ma, J.: *A new neural network model for the state-of-charge estimation in the battery degradation process*, in: *Applied Energy 121*, pp. 20–27, 2014

158. Waag, W.; Käbitz, S.; Sauer, D.U.: *Experimental investigation of the lithium-ion battery impedance characteristic at various conditions and aging states and its influence on the application*, in: *Applied Energy 102*, pp. 885–897, 2013

159. Tröltzsch, U.; Kanoun, O.; Tränkler, H.-R.: *Characterizing aging effects of lithium ion batteries by impedance spectroscopy*, in: *Electrochimica Acta 51 (8–9)*, pp. 1664–1672, 2006

160. Schranzhofer, H.; Bugajski, J.; Santner, H.J.; Korepp, C.; Möller, K.-C.; Besenhard, J.O.; Winter, M.; Sitte, W.: *Electrochemical impedance spectroscopy study of the SEI formation on graphite and metal electrodes*, in: *Journal of Power Sources 153 (2)*, pp. 391–395, 2006

161. Andre, D.; Meiler, M.; Steiner, K.; Walz, H.; Soczka-Guth, T.; Sauer, D.U.: *Characterization of high-power lithium-ion batteries by electrochemical impedance spectroscopy - II: Modelling*, in: *Journal of Power Sources 196 (12)*, pp. 5349–5356, 2011

162. Andre, D.; Meiler, M.; Steiner, K.; Wimmer, C.; Soczka-Guth, T.; Sauer, D.U.: *Characterization of high-power lithium-ion batteries by electrochemical impedance spectroscopy - I. Experimental investigation*, in: *Journal of Power Sources 196 (12)*, pp. 5334–5341, 2011

163. Burns, J.C.; Petibon, R.; Nelson, K.J.; Sinha, N.N.; Kassam, A.; Way, B.M.; Dahn, J.R.: *Studies of the Effect of Varying Vinylene Carbonate (VC) Content in Lithium Ion Cells on Cycling Performance and Cell Impedance*, in: *Journal of The Electrochemical Society 160 (10)*, A1668–A1674, 2013

164. Dai, H.; Xu, T.; Zhu, L.; Wei, X.; Sun, Z.: *Adaptive model parameter identification for large capacity Li-ion batteries on separated time scales*, in: *Applied Energy 184*, pp. 119–131, 2016

165. Fang, K.; Mu, D.; Chen, S.; Wu, B.; Wu, F.: *A prediction model based on artificial neural network for surface temperature simulation of nickel–metal hydride battery during charging*, in: *Journal of Power Sources 208*, pp. 378–382, 2012

166. Zaghib, K.; Nadeau, G.; Kinoshita, K.: *Effect of Graphite Particle Size on Irreversible Capacity Loss*, in: *Journal of The Electrochemical Society 147 (6)*, pp. 2110–2115, 2000

167. Li, D.; Danilov, D.; Zhang, Z.; Chen, H.; Yang, Y.; Notten, P.H.L.: *Modeling the SEI-Formation on Graphite Electrodes in LiFePO$_4$ Batteries*, in: *Journal of The Electrochemical Society 162 (6)*, A858–A869, 2015

168. Martínez-Rodríguez, M.J.; Shimpalee, S.; van Zee, J.W.: *Measurement of MacMullin Numbers for PEMFC Gas-Diffusion Media*, in: *Journal of The Electrochemical Society 156 (1)*, B80–B85, 2009

169. Martínez-Rodríguez, M.J.; Cui, T.; Shimpalee, S.; Seraphin, S.; Duong, B.; van Zee, J.W.: *Effect of microporous layer on MacMullin number of carbon paper gas diffusion layer*, in: *Journal of Power Sources 207*, pp. 91–100, 2012

170. Landesfeind, J.; Ehrl, A.; Graf, M.; Wall, W.A.; Gasteiger, H.A.: *Direct Electrochemical Determination of Thermodynamic Factors in Aprotic Binary Electrolytes*, in: *Journal of The Electrochemical Society 163 (7)*, A1254–A1264, 2016

171. Guidelli, R.; Compton, R.G.; Feliu, J.M.; Gileadi, E.; Lipkowski, J.; Schmickler, W.; Trasatti, S.: *Defining the transfer coefficient in electrochemistry: An assessment (IUPAC Technical Report)*, in: *Pure and Applied Chemistry 86 (2)*, pp. 245–258, 2014

172. Jokar, A.; Rajabloo, B.; Désilets, M.; Lacroix, M.: *An Inverse Method for Estimating the Electrochemical Parameters of Lithium-Ion Batteries - I. Methodology*, in: *Journal of The Electrochemical Society 163 (14)*, A2876–A2886, 2016

173. Yan, J.; Xia, B.-J.; Su, Y.-C.; Zhou, X.-Z.; Zhang, J.; Zhang, X.-G.: *Phenomenologically modeling the formation and evolution of the solid electrolyte interface on the graphite electrode for lithium-ion batteries*, in: *Electrochimica Acta 53 (24)*, pp. 7069–7078, 2008

174. Pinson, M.B.; Bazant, M.Z.: *Theory of SEI Formation in Rechargeable Batteries: Capacity Fade, Accelerated Aging and Lifetime Prediction*, in: *Journal of The Electrochemical Society 160 (2)*, A243–A250, 2013

175. Ecker, M.; Nieto, N.; Käbitz, S.; Schmalstieg, J.; Blanke, H.; Warnecke, A.; Sauer, D.U.: *Calendar and cycle life study of Li(NiMnCo)O₂-based 18650 lithium-ion batteries*, in: *Journal of Power Sources 248*, pp. 839–851, 2014

176. Ekström, H.; Lindbergh, G.: *A Model for Predicting Capacity Fade due to SEI Formation in a Commercial Graphite/LiFePO₄ Cell*, in: *Journal of The Electrochemical Society 162 (6)*, A1003–A1007, 2015

177. Ploehn, H.J.; Ramadass, P.; White, R.E.: *Solvent Diffusion Model for Aging of Lithium-Ion Battery Cells*, in: *Journal of The Electrochemical Society 151 (3)*, A456–A462, 2004

178. Ashwin, T.R.; Chung, Y.M.; Wang, J.: *Capacity fade modelling of lithium-ion battery under cyclic loading conditions*, in: *Journal of Power Sources 328*, pp. 586–598, 2016

179. Schuster, S.F.; Bach, T.C.; Fleder, E.; Müller, J.; Brand, M.J.; Sextl, G.; Jossen, A.: *Nonlinear aging characteristics of lithium-ion cells under different operational conditions*, in: *Journal of Energy Storage 1*, pp. 44–53, 2015

180. Bach, T.C.; Schuster, S.F.; Fleder, E.; Müller, J.; Brand, M.J.; Lorrmann, H.; Jossen, A.; Sextl, G.: *Nonlinear aging of cylindrical lithium-ion cells linked to heterogeneous compression*, in: *Journal of Energy Storage 5*, pp. 212–223, 2016

181. Lin, X.; Park, J.; Liu, L.; Lee, Y.K.; Sastry, A.M.; Lu, W.: *A Comprehensive Capacity Fade Model and Analysis for Li-Ion Batteries*, in: *Journal of The Electrochemical Society 160 (10)*, A1701–A1710, 2013

182. Cai, L.; Dai, Y.; Nicholson, M.; White, R.E.; Jagannathan, K.; Bhatia, G.: *Life modeling of a lithium ion cell with a spinel-based cathode*, in: *Journal of Power Sources 221*, pp. 191–200, 2013

183. Trippe, A.E.; Arunachala, R.; Massier, T.; Jossen, A.; Hamacher, T.: *Charging optimization of battery electric vehicles including cycle battery aging - 12 - 15 Oct. 2014, Istanbul*, in: *IEEE PES Innovative Smart Grid Technologies Conference Europe*, pp. 1–6, 2014

184. Zhang, G.; Shaffer, C.E.; Wang, C.-Y.; Rahn, C.D.: *In-Situ Measurement of Current Distribution in a Li-Ion Cell*, in: *Journal of The Electrochemical Society 160 (4)*, A610–A615, 2013

185. Osswald, P.J.; Erhard, S.V.; Wilhelm, J.; Hoster, H.E.; Jossen, A.: *Simulation and Measurement of Local Potentials of Modified Commercial Cylindrical Cells - I. Cell Preparation and Measurements*, in: *Journal of The Electrochemical Society 162 (10)*, A2099–A2105, 2015

186. Osswald, P.J.; Erhard, S.V.; Rheinfeld, A.; Rieger, B.; Hoster, H.E.; Jossen, A.: *Temperature dependency of state of charge inhomogeneities and their equalization in cylindrical lithium-ion cells*, in: *Journal of Power Sources 329*, pp. 546–552, 2016

187. Harris, S.J.; Lu, P.: *Effects of Inhomogeneities—Nanoscale to Mesoscale—on the Durability of Li-Ion Batteries*, in: *The Journal of Physical Chemistry C 117 (13)*, pp. 6481–6492, 2013

188. Harris, S.J.; Timmons, A.; Baker, D.R.; Monroe, C.W.: *Direct in situ measurements of Li transport in Li-ion battery negative electrodes*, in: *Chemical Physics Letters 485 (4-6)*, pp. 265–274, 2010

189. Kitada, K.; Murayama, H.; Fukuda, K.; Arai, H.; Uchimoto, Y.; Ogumi, Z.; Matsubara, E.: *Factors determining the packing-limitation of active materials in the composite electrode of lithium-ion batteries*, in: *Journal of Power Sources 301*, pp. 11–17, 2016

190. Abe, H.; Kubota, M.; Nemoto, M.; Masuda, Y.; Tanaka, Y.; Munakata, H.; Kanamura, K.: *High-capacity thick cathode with a porous aluminum current collector for lithium secondary batteries*, in: *Journal of Power Sources 334*, pp. 78–85, 2016

191. Tanida, H.; Yamashige, H.; Orikasa, Y.; Gogyo, Y.; Arai, H.; Uchimoto, Y.; Ogumi, Z.: *Elucidating the Driving Force of Relaxation of Reaction Distribution in LiCoO$_2$ and LiFePO$_4$ Electrodes Using X-ray Absorption Spectroscopy*, in: *The Journal of Physical Chemistry C 120 (9)*, pp. 4739–4743, 2016

192. Erhard, S.V.; Osswald, P.J.; Wilhelm, J.; Rheinfeld, A.; Kosch, S.; Jossen, A.: *Simulation and Measurement of Local Potentials of Modified Commercial Cylindrical Cells - II: Multi-Dimensional Modeling and Validation*, in: *Journal of The Electrochemical Society 162 (14)*, A2707–A2719, 2015

193. Erhard, S.V. et al.: *Simulation and Measurement of the Current Density Distribution in Lithium-Ion Batteries by a Multi-Tab Cell Approach*, in: *Journal of The Electrochemical Society 164 (1)*, A6324–A6333, 2017

194. Zinth, V.; von Lüders, C.; Hofmann, M.; Hattendorff, J.; Buchberger, I.; Erhard, S.V.; Rebelo-Kornmeier, J.; Jossen, A.; Gilles, R.: *Lithium plating in lithium-ion batteries at sub-ambient temperatures investigated by in situ neutron diffraction*, in: *Journal of Power Sources 271*, pp. 152–159, 2014

195. von Lüders, C.; Zinth, V.; Erhard, S.V.; Osswald, P.J.; Hofmann, M.; Gilles, R.; Jossen, A.: *Lithium plating in lithium-ion batteries investigated by voltage relaxation and in situ neutron diffraction*, in: *Journal of Power Sources 342*, pp. 17–23, 2017

196. Rieger, B.; Schuster, S.F.; Erhard, S.V.; Osswald, P.J.; Rheinfeld, A.; Willmann, C.; Jossen, A.: *Multi-directional laser scanning as innovative method to detect local cell damage during fast charging of lithium-ion cells*, in: *Journal of Energy Storage 8*, pp. 1–5, 2016

197. Kindermann, F.M.; Osswald, P.J.; Klink, S.; Ehlert, G.; Schuster, J.; Noel, A.; Erhard, S.V.; Schuhmann, W.; Jossen, A.: *Measurements of lithium-ion concentration equilibration processes inside graphite electrodes*, in: *Journal of Power Sources 342*, pp. 638–643, 2017

198. La Mantia, F.: *Characterization of Electrodes for Lithium-Ion Batteries through Electrochemical Impedance Spectroscopy and Mass Spectrometry - Nr. 17848*, ETH Zürich, Zürich, 2008

199. Ng, S.-H.; La Mantia, F.; Novák, P.: *A multiple working electrode for electrochemical cells: A tool for current density distribution studies*, in: *Angewandte Chemie International Edition 48 (3)*, pp. 528–532, 2009

200. Klink, S.; Schuhmann, W.; La Mantia, F.: *Vertical Distribution of Overpotentials and Irreversible Charge Losses in Lithium Ion Battery Electrodes*, in: *ChemSusChem 7 (8)*, pp. 2159–2166, 2014

201. Klink, S.; Weide, P.; Muhler, M.; Schuhmann, W.; La Mantia, F.: *New Insights into SEI Formation in Lithium Ion Batteries: Inhomogeneous Distribution of Irreversible Charge Losses Across Graphite Electrodes*, in: *ECS Transactions 62 (1)*, pp. 265–271, 2014

202. Barsoukov, E.; Macdonald, J.R.: *Impedance spectroscopy - Theory, experiment, and applications*, 2nd edition, Wiley-Interscience, Hoboken, NJ, 2005

203. Orazem, M.E.; Tribollet, B.: *Electrochemical Impedance Spectroscopy*, Wiley, Hoboken, NJ, 2008

204. Huggins, R.: *Advanced batteries - Materials science aspects*, 1st edition, Springer, Berlin, 2009

205. Popkirov, G.S.: *Fast time-resolved electrochemical impedance spectroscopy for investigations under nonstationary conditions*, in: *Electrochimica Acta 41 (7-8)*, pp. 1023–1027, 1996

206. Pop, V.; Bergveld, H.J.; Notten, P.H.L.; Regtien, P.P.L.: *State-of-the-art of battery state-of-charge determination*, in: *Measurement Science and Technology 16 (12)*, R93–R110, 2005

207. Ran, L.; Junfeng, W.; Haiying, W.; Gechen, L.: *Prediction of state of charge of Lithium-ion rechargeable battery with electrochemical impedance spectroscopy theory*, in: 5th IEEE Conference on Industrial Electronics and Applications (ICIEA), 2010

208. Waag, W.; Fleischer, C.; Sauer, D.U.: *Critical review of the methods for monitoring of lithium-ion batteries in electric and hybrid vehicles*, in: *Journal of Power Sources 258*, pp. 321–339, 2014

209. Ecker, M.; Gerschler, J.B.; Vogel, J.; Käbitz, S.; Hust, F.; Dechent, P.; Sauer, D.U.: *Development of a lifetime prediction model for lithium-ion batteries based on extended accelerated aging test data*, in: *Journal of Power Sources 215*, pp. 248–257, 2012

210. Li, Y.; Bettge, M.; Polzin, B.J.; Zhu, Y.; Balasubramanian, M.; Abraham, D.P.: *Understanding Long-Term Cycling Performance of $Li_{1.2}Ni_{0.15}Mn_{0.55}Co_{0.1}O_2$-Graphite Lithium-Ion Cells*, in: *Journal of The Electrochemical Society 160 (5)*, A3006–A3019, 2013

211. Ning, G.; Haran, B.S.; Popov, B.N.: *Capacity fade study of lithium-ion batteries cycled at high discharge rates*, in: *Journal of Power Sources 117 (1-2)*, pp. 160–169, 2003

212. Shim, J.; Kostecki, R.; Richardson, T.; Song, X.; Striebel, K.A.: *Electrochemical analysis for cycle performance and capacity fading of a lithium-ion battery cycled at elevated temperature*, in: *Journal of Power Sources 112 (1)*, pp. 222–230, 2002

213. Zhang, Y.; Wang, C.-Y.: *Cycle-Life Characterization of Automotive Lithium-Ion Batteries with $LiNiO_2$ Cathode*, in: *Journal of The Electrochemical Society 156 (7)*, A527–A535, 2009

214. Zhang, J.; Lee, J.: *A review on prognostics and health monitoring of Li-ion battery*, in: *Journal of Power Sources 196 (15)*, pp. 6007–6014, 2011

215. Cho, H.-M.; Choi, W.-S.; Go, J.-Y.; Bae, S.-E.; Shin, H.-C.: *A study on time-dependent low temperature power performance of a lithium-ion battery*, in: *Journal of Power Sources 198*, pp. 273–280, 2012

216. Roth, J.G.: *Impedanzspektroskopie als Verfahren zur Alterungsanalyse von Hochleistungs-Lithium-Ionen-Zellen*, Verlag Dr. Hut, München, 2013

217. Schmidt, J.P.; Arnold, S.; Loges, A.; Werner, D.; Wetzel, T.; Ivers-Tiffée, E.: *Measurement of the internal cell temperature via impedance: Evaluation and application of a new method*, in: *Journal of Power Sources 243*, pp. 110–117, 2013

218. Wang, C.; Appleby, A.J.; Little, F.E.: *Electrochemical impedance study of initial lithium ion intercalation into graphite powders*, in: *Electrochimica Acta 46 (12)*, pp. 1793–1813, 2001

219. Barai, A.; Chouchelamane, G.H.; Guo, Y.; McGordon, A.; Jennings, P.A.: *A study on the impact of lithium-ion cell relaxation on electrochemical impedance spectroscopy*, in: *Journal of Power Sources 280*, pp. 74–80, 2015

220. Kindermann, F.M.; Noel, A.; Keil, P.; Jossen, A.: *Influence of Relaxation Time on EIS Measurements of Li-ion Batteries*, Chemnitz, 26.09.2013 – 27.09.2013

221. Zhang, S.S.; Xu, K.; Jow, T.R.: *Electrochemical impedance study on the low temperature of Li-ion batteries*, in: *Electrochimica Acta 49 (7)*, pp. 1057–1061, 2004

222. *PNGV Test Plan for Advanced Technology Development GEN 2 Lithium-ion Cells - EHV-TP-121*, 2002

223. Gaberscek, M.; Dominko, R.; Jamnik, J.: *The meaning of impedance measurements of LiFePO$_4$ cathodes: A linearity study*, in: *Journal of Power Sources 174 (2)*, pp. 944–948, 2007

224. Fleischer, C.; Waag, W.; Heyn, H.-M.; Sauer, D.U.: *On-line adaptive battery impedance parameter and state estimation considering physical principles in reduced order equivalent circuit battery models: Part 2. Parameter and state estimation*, in: *Journal of Power Sources 262*, pp. 457–482, 2014

225. Bernardi, D.M.; Chandrasekaran, R.; Go, J.-Y.: *Solid-state transport of lithium in lithium-ion-battery positive electrodes*, in: *Journal of The Electrochemical Society 160 (9)*, A1430–A1441, 2013

226. Bernardi, D.M.; Go, J.-Y.: *Analysis of pulse and relaxation behavior in lithium-ion batteries*, in: *Journal of Power Sources 196 (1)*, pp. 412–427, 2011

227. Pei, L.; Wang, T.; Lu, R.; Zhu, C.: *Development of a voltage relaxation model for rapid open-circuit voltage prediction in lithium-ion batteries*, in: *Journal of Power Sources 253*, pp. 412–418, 2014

228. Waag, W.; Sauer, D.U.: *Adaptive estimation of the electromotive force of the lithium-ion battery after current interruption for an accurate state-of-charge and capacity determination*, in: *Applied Energy 111*, pp. 416–427, 2013

229. Kindermann, F.M.; Noel, A.; Erhard, S.V.; Jossen, A.: *Long-term equalization effects in Li-ion batteries due to local state of charge inhomogeneities and their impact on impedance measurements*, in: *Electrochimica Acta 185*, pp. 107–116, 2015

List of Publications

I **Kindermann, F.M.**; Noel, A.; Erhard, S.V.; Jossen, A.: *Long-term equalization effects in Li-ion batteries due to local state of charge inhomogeneities and their impact on impedance measurements*, in: *Electrochimica Acta 185*, pp. 107–116, 2015

II Osswald, P.J.; Erhard, S.V.; Keil, P.; **Kindermann, F.M.**; Hoster, H.E.; Jossen, A.: *Current density distribution in cylindrical Li-Ion cells during impedance measurements*, in: *Journal of Power Sources 314*, pp. 93–101, 2016

III Erhard, S.V.; Osswald, P.J.; Keil, P.; Höffer, E.; Haug, M.; Noel, A.; Wilhelm, J.; Rieger, B.; Schmidt, K.; Kosch, S.; **Kindermann, F.M.**; Spingler, F.B.; Kloust, H.; Thoennessen, T.; Rheinfeld, A.; Jossen, A.: *Simulation and Measurement of the Current Density Distribution in Lithium-Ion Batteries by a Multi-Tab Cell Approach*, in: *Journal of The Electrochemical Society 164 (1)*, pp. A6324–A6333, 2017

IV **Kindermann, F.M.**; Osswald, P.J.; Klink, S.; Ehlert, G.; Schuster, J.; Noel, A.; Erhard, S.V.; Schuhmann, W.; Jossen, A.: *Measurements of lithium-ion concentration equilibration processes inside graphite electrodes*, in: *Journal of Power Sources 342*, pp. 638–643, 2017

V **Kindermann, F.M.**; Osswald, P.J.; Ehlert, G.; Schuster, J.; Rheinfeld, A.; Jossen, A.: *Reducing Inhomogeneous Current Density Distribution in Graphite Electrodes by Design Variation*, in: *Journal of The Electrochemical Society 164 (11)*, pp. E3105–E3113, 2017

VI **Kindermann, F.M.**; Keil, J.; Frank, A.; Jossen, A.: *A SEI Modeling Approach Distinguishing between Capacity and Power Fade*, in: *Journal of The Electrochemical Society 164 (12)*, pp. E287–E294, 2017

Acknowledgment